Lattice Simulations of two-color QCD at finite density

Gittersimulationen der QCD
mit zwei Farben bei endlicher Dichte

Master-Thesis

vorgelegt beim

Fachbereich 07
Mathematik und Informatik, Physik, Geographie

JUSTUS-LIEBIG-
UNIVERSITÄT
GIESSEN

von

Jonas Wilhelm

25.08.2016

Erstgutachter: Prof. Dr. Lorenz von Smekal
Zweitgutachter: Prof. Dr. Christian Fischer
Institut für Theoretische Physik
Justus-Liebig-Universität Gießen

Abstract

We study two-color QCD at finite density by employing lattice simulations. For this, we can apply importance sampling Monte Carlo techniques, as the sign problem is not present in SU(2) lattice gauge theories at finite Baryon chemical potential. To observe the spontaneous symmetry breaking of quark number conservation, we have to introduce an explicit diquark source term into the lattice action. The possibility to reduce the number of dynamical quark flavors in lattice simulations by employing real pseudofermions is probed. Finally, we use rooted staggered quarks and reduce to $N_f = 2$ continuum quark flavors. For suppressing the artificial bulk phase, we utilize an improved gauge action and simulate at a larger gauge coupling than earlier lattice studies [1]. The chiral condensate, the diquark condensate and the quark number density are measured in dependence of the chemical potential. We find a large influence of UV-divergent terms on the chiral condensate, thus we need to perform an additive renormalization. Furthermore, the spectrum of the Goldstone modes at finite density is investigated. We compare our numerical results from lattice simulations to the predictions of leading order chiral perturbation theory.

Zusammenfassung

Wir untersuchen Zwei-Farb QCD bei endlicher Dichte mittels Gittersimulationen. Dazu können wir Monte-Carlo-Methoden anwenden, da das Vorzeichenproblem in SU(2) Gittertheorien bei endlichem baryonischen chemischen Potential nicht existiert. Um die spontane Symmetriebrechung der Quarkzahlerhaltung zu beobachten, müssen wir eine explizite Diquarkquelle in die Gitterwirkung einführen. Die Möglichkeit die Anzahl der dynamischen Quarks in Gittersimulationen zu reduzieren, indem reelle Pseudofermionen benutzt werden, wird getestet. Letztendlich benutzen wir Rooted-Staggered-Quarks und reduzieren zu $N_f = 2$ kontinuum Quarks. Zur Unterdrückung der künstlichen Bulkphase benutzen wir eine verbesserte Eichwirkung und simulieren bei einer größeren Eichkopplung als frühere Gittersimulationen [1]. Das chirale Kondensat, das Diquarkkondensat und die Quarkzahldichte werden in Abhängigkeit zum chemischen Potential gemessen. Wir beobachten eine große Beeinflussung des chiralen Kondensates durch UV-divergierende Beiträge, daher muss eine additive Renormierung durchgeführt werden. Weiterhin wird das Spektrum der Goldstone-Moden bei endlicher Dichte untersucht. Wir vergleichen unsere numerischen Ergebnisse aus Gittersimulation mit den Vorhersagen der chiralen Störungstheorie in niedrigster Ordnung.

Contents

1. Introduction

This master thesis investigates the phase diagram of Quantum Chromodynamics (QCD), which is the field theory of the strong force, describing the interactions of quarks and gluons. In general, the gauge group of QCD is SU(N_c), which is non-abelian and hence self-interactions of the gluons arise, effecting the prominent property of QCD that the beta function for the gauge coupling is negative [2]. This leads on the one hand to *asymptotic freedom* at large energy scales, where the gauge coupling becomes small. In this regime the color-charged quarks are free and not bound into hadrons. On the other hand at low energy scales the gauge coupling becomes large, resulting in a strong coupling of quarks and gluons. This regime is associated with the so-called *confinement*, where all quarks are bound into hadrons, so that only color-neutral objects exist. The regime of confinement is associated with a hadron and nuclear matter phase whereas the regime of asymptotic freedom is associated with a quark-gluon plasma (QGP) phase at high temperature and a color superconducting phase at low temperature. The color superconducting phase is indicated by the pairing of quarks, leading to a non-vanishing diquark condensate. Figure (1.1) shows an overview of the QCD phase diagram, which illustrates the dependence of the phase of quark matter on the temperature and the density.

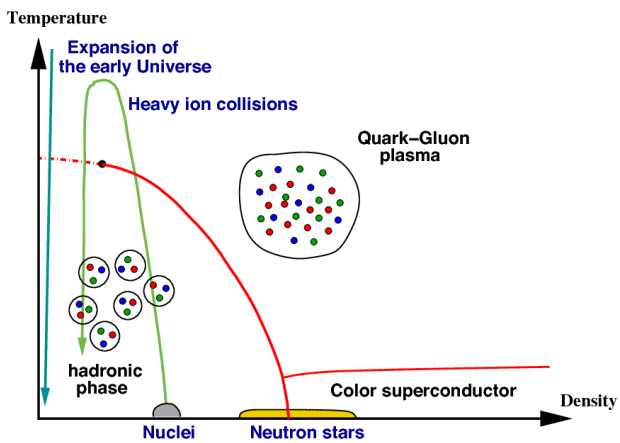

Figure 1.1.: An overview of the QCD phase diagram. The blue arrow sketches the expansion of the early Universe. The green arrow shows the path through the phase diagram during a heavy ion collision. [3]

In the regime of asymptotic freedom calculations using perturbative expansions can be done as the gauge coupling is small. However, for the study of hadrons and

confinement non-perturbative methods are needed, as for large gauge couplings perturbative expansions are not meaningful. A method for the non-perturbative calculation of observables from QCD based on the path-integral formalism is *lattice QCD*, which is our method of choice. In lattice QCD integrals are approximated with Monte Carlo methods, and the action is discretized onto a discrete space-time lattice. We will give an introduction to the basic concepts of lattice QCD in section {2}. Then, we will show the formalism of staggered fermions in section {3}, which are especially cheap for numerical calculations, as the action for staggered fermions is diagonal in Dirac space, and present the Hybrid Monte Carlo (HMC) algorithm for numerical calculations in section {4}. It will be shown in section {2.5.2}, that the path-integral of the fermions is given by the so-called *fermion determinant*. To investigate the phase diagram of QCD, we need to introduce a non-vanishing temperature as well as a quark chemical potential (see section {5}), where the latter leads to a matter-antimatter asymmetry. On the lattice a quark chemical potential is easily included with the help of an external temporal abelian gauge field. Unfortunately, this leads to the so-called *sign problem* for $N_c = 3$, which causes the importance sampling used in Monte Carlo methods to be ill-defined as explained in section {5.3}. To overcome this problem, we restrict our numerical calculations to $N_c = 2$, in contrary to the physical three color QCD. Including only two colors into the theory avoids the sign problem due to the pseudo-reality of the SU(2) gauge group [4]. For the theoretical derivations and overviews, we will use the general gauge group SU(N_c) and only reduce to SU(2) when necessary. Lattice QCD allows us to study different phase transitions of QCD, like the *deconfinement phase transition* and the *chiral transition*, indicated by a non-vanishing Polyakov loop and chiral condensate, respectively [5]. In this master thesis, we want to observe the color superconductor phase through measuring the diquark condensate on the lattice. Notice that in two-color QCD the diquarks do not carry a net color, so that this phase is a superfluid phase in our simulations. The transition to a phase with a non-vanishing diquark condensate will cause a spontaneous breakdown of quark number conservation. To be able to observe this on the lattice, we need to include a diquark source term in the fermion action and later extrapolate the results back to vanishing diquark source to achieve the physical situation. The inclusion of a diquark source term into the theory is shown in section {6}. We consider the symmetries and the pattern of symmetry breaking of the resulting lattice action in section {7}. The measurement of the masses of the Goldstone modes in dependence of the chemical potential is explained in section {8}. With the knowledge of the pattern of symmetry breaking on the lattice, we can find the continuum theory obeying the same pattern and apply leading order chiral perturbation theory to it, see section {9}. This gives us predictions for the chiral and diquark condensate, the quark number density and the Goldstone spectrum, which we can fit to our numerical data. Previous calculations showed [6][7][8], that two-color QCD exhibits the properties of diquark condensation as well as having color confinement, hence an investigation of this theory seems justified and one hopes that results and predictions will be close to the physical three color QCD.

2. The Framework of Lattice QCD

In this section, we will show how to describe QCD on a discrete four dimensional space-time lattice

$$\begin{aligned}\Lambda = \{n = (n_1, n_2, n_3, n_4) \mid \\ n_i = 0, 1, 2, .., N_s - 1, i = 1, 2, 3;\ n_4 = 0, 1, 2, ..., N_t - 1\}\end{aligned} \tag{2.0.1}$$

where integers are used to label the lattice points n [5][9]. The physical space-time points x can be calculated by multiplying the integer points n with the lattice spacing a: $x = an$. First, the fermionic part will be inspected, giving a naive discretization of the fermion action and introducing the gluon fields as gauge fields on the lattice. Then, an action for the gluons is constructed from the requirement of gauge invariance. A first overview of how to measure observables by calculating the QCD path integral on the lattice will be given. The order parameter of the deconfinement phase transition will be introduced and the artificial bulk phase will be discussed.

2.1. Naive Discretization of the Fermion Action

The free Euclidean continuum fermion action for a single quark flavor is given by

$$S_F^0[\psi, \bar{\psi}] = \int d^4x\ \bar{\psi}(x)\ (\gamma_\mu \partial_\mu + m)\ \psi(x)\ . \tag{2.1.1}$$

To get the lattice equivalent of this action, one has to replace the integral over the whole space-time by a sum over the discrete lattice points $n \in \Lambda$. The fermion fields get evaluated at the lattice points only, giving a $4N_c$ dimensional vector for $\psi(n)$ and $\bar{\psi}(n)$ at every $n \in \Lambda$. At last, one needs to discretize the derivative of the fermion field. This can be done, for example, by the midpoint difference

$$\partial_\mu \psi(n) \to \Delta_\mu \psi(n) = \frac{\psi(n + \hat{\mu}) - \psi(n - \hat{\mu})}{2a}\ , \tag{2.1.2}$$

where $\hat{\mu}$ is a unit vector in μ-direction. Putting all together one obtains the naive discretization of the free fermion action

$$S_F^0[\psi, \bar{\psi}] = a^4 \sum_{n \in \Lambda} \bar{\psi}(n)\ \left(\sum_{\mu=1}^{4} \gamma_\mu \frac{\psi(n + \hat{\mu}) - \psi(n - \hat{\mu})}{2a} + m\ \psi(n) \right)\ . \tag{2.1.3}$$

As in the continuum, we require the action to be invariant under gauge-transformation, where for the gauge-transformation a SU(N_c) element $\Omega(n)$ at every lattice point $n \in \Lambda$ is used. The fermion fields transform like

$$\psi(n) \to \psi'(n) = \Omega(n)\ \psi(n) \tag{2.1.4}$$
$$\bar{\psi}(n) \to \bar{\psi}'(n) = \bar{\psi}(n)\ \Omega(n)^\dagger\ . \tag{2.1.5}$$

It is easy to see that the mass term is invariant, but the derivative term is not

$$\bar{\psi}(n)\psi(n+\hat{\mu}) \to \bar{\psi}'(n)\psi'(n+\hat{\mu}) = \bar{\psi}(n)\ \Omega(n)^\dagger\Omega(n+\hat{\mu})\ \psi(n+\hat{\mu})\ . \tag{2.1.6}$$

To ensure the gauge-invariance of the derivative, one introduces directional fields $U_\mu(n)$ represented by a SU(N_c) matrix at every lattice point in each direction. Defining the gauge transformation of this fields to be

$$U_\mu(n) \to U'_\mu(n) = \Omega(n)\ U_\mu(n)\ \Omega(n+\hat{\mu})^\dagger\ , \tag{2.1.7}$$

the terms $\bar{\psi}(n)U_\mu(n)\psi(n+\hat{\mu})$ and $\bar{\psi}(n)U_\mu(n-\hat{\mu})^\dagger\psi(n-\hat{\mu})$ become invariant. The fields $U_\mu(n)$ are called *link-variables*, as they connect two lattice points through their directional character and represent the gluon fields on the lattice. On the lattice the gluon fields are SU(N_c) group elements, where in the continuum the gauge field is represented by elements of the Lie algebra su(N_c). The relation between the lattice link-variables and the continuum gluon fields will be shown in section (2.3). One also defines link-variables oriented in negative direction through hermitian conjugation of the positive oriented link-variable

$$U_{-\mu}(n) \equiv U_\mu(n-\hat{\mu})^\dagger\ . \tag{2.1.8}$$

Now, the gauge invariant naive fermion action including the interactions with the gluon fields is given by

$$S_F[\psi,\bar{\psi},U] = a^4 \sum_{n\in\Lambda} \bar{\psi}(n) \left(\sum_{\mu=1}^{4} \gamma_\mu \frac{U_\mu(n)\psi(n+\hat{\mu}) - U_{-\mu}(n)\psi(n-\hat{\mu})}{2a} + m\ \psi(n) \right)\ . \tag{2.1.9}$$

In appendix (A.2) it is shown that one recovers the form of the continuum action by taking the naive continuum limit $a \to 0$, for which results from section {2.3} are needed. Unfortunately, this naive action has the problem of actually describing sixteen fermions instead of one. This can be seen by calculating the propagator in momentum space. The propagator of a fermion is given by the inverse of the Dirac operator. For the naive action the Dirac operator reads

$$D(n|m) = \sum_{\mu=1}^{4} \gamma_\mu \frac{\delta_{m,n+\hat{\mu}} - \delta_{m,n-\hat{\mu}}}{2a} + m\ \delta_{n,m}\ . \tag{2.1.10}$$

Calculating the Fourier-transform, one ends up with

$$\begin{aligned}\tilde{D}(p|q) &= \frac{1}{|\Lambda|}\sum_{n,m\in\Lambda} e^{-ip\cdot na}\ D(n|m)\ e^{iq\cdot ma} \\ &= \frac{1}{|\Lambda|}\sum_{n,m\in\Lambda} e^{-i(p-q)\cdot na}\ \left(\sum_{\mu=1}^{4}\gamma_\mu \frac{e^{iq_\mu a}-e^{-iq_\mu a}}{2a} + m\ \mathbb{I}\right) \\ &= \delta(p-q)\ \tilde{D}(p)\end{aligned} \tag{2.1.11}$$

$$\implies \quad \tilde{D}(p) = m\ \mathbb{I} + \frac{i}{a}\sum_{\mu=1}^{4}\gamma_\mu\ \sin(p_\mu a)\ , \tag{2.1.12}$$

where $|\Lambda|$ is the total number of lattice points. Finally, the propagator in momentum space is given by

$$\frac{1}{a}S(p) = \left(i\sum_{\mu=1}^{4}\gamma_\mu\ \sin(p_\mu a) + ma\ \mathbb{I}\right)^{-1} = \frac{-i\sum_{\mu=1}^{4}\gamma_\mu\ \sin(p_\mu a) + ma\ \mathbb{I}}{\sum_{\mu=1}^{4}\sin^2(p_\mu a) + (ma)^2}\ . \tag{2.1.13}$$

It is easy to see that the massless propagator has a pole at each corner of the Brillouin zone given by $ap = \{(0,0,0,0),(\pi,0,0,0),(0,\pi,0,0),...,(\pi,\pi,\pi,\pi)\}$. Thus, the naive action describes sixteen fermions instead of one. The additional fermions are so-called *doublers*. A way to avoid the doublers was introduced by Wilson, which is explained in the next section.

2.2. Wilson Fermions

To avoid the doublers, Wilson introduced a second-derivative like operator which alters the dispersion relation by lifting the masses of the doublers but still leaving one low energy solution. A second derivative can be discretized as

$$\partial_\mu^2\psi(n) \to \Delta_\mu^2\psi(n) = \frac{\psi(n+\hat{\mu}) - 2\psi(n) + \psi(n-\hat{\mu})}{a^2} \tag{2.2.1}$$

and hence the additional term proposed by Wilson reads [10]

$$S^W[\psi,\bar{\psi},U] = -\frac{ra^5}{2}\sum_{n\in\Lambda,\mu}\bar{\psi}(n)\ \frac{U_\mu(n)\psi(n+\hat{\mu}) - 2\psi(n) + U_\mu(n-\hat{\mu})\psi(n-\hat{\mu})}{a^2}\ . \tag{2.2.2}$$

The additional parameter r tunes the effect of this operator. Being proportional to the lattice spacing a, this term vanishes in the naive continuum limit $a \to 0$. Adding

it to the naive action (2.1.9) and calculating the free propagator, one ends up with [11]

$$\frac{1}{a}S(p) = \frac{-i\sum_{\mu=1}^{4}\gamma_\mu\ \sin(p_\mu a) + ma\ \mathbb{I} - r\sum_{\mu=1}^{4}(\cos(p_\mu a)-1)}{\sum_{\mu=1}^{4}\sin^2(p_\mu a) + \left[ma - r\sum_{\mu=1}^{4}(\cos(p_\mu a)-1)\right]^2}\ . \tag{2.2.3}$$

This propagator still has a large contribution for $ap_\mu = (0,0,0,0)$, but the masses of the doublers get lifted according to

$$m_{\text{doubler}} = m + \frac{2r}{a}\cdot k\ , \tag{2.2.4}$$

where k is the number of components of p_μ equal to $\frac{\pi}{a}$. Therefore, in the limit $a \to 0$ the doubler become very heavy and only the physical pole for $ap_\mu = (0,0,0,0)$ remains. Often the Wilson action is written by introducing the *hopping parameter* $\kappa = \frac{1}{2(ma+4r)}$ and rescaling the fields according to $\psi \to \frac{1}{\sqrt{2a\kappa}}\ \psi$, one ends up with

$$\begin{aligned} S[\psi,\bar{\psi},U] = a^4 \sum_{n\in\Lambda} [\bar{\psi}(n)\ \psi(n) \\ - \kappa\ \bar{\psi}(n)\sum_{\mu=1}^{4}((r-\gamma_\mu)U_\mu(n)\psi(n+\hat{\mu}) + (r+\gamma_\mu)U_{-\mu}(n)\psi(n-\hat{\mu}))]\ . \end{aligned} \tag{2.2.5}$$

Usually the parameter r is set equal to one. The Wilson action (2.2.5) is gauge-invariant and doubler free, but being a mass term the second-derivative like term explicitly breaks chiral symmetry, even in the case of massless fermions. See section {3.3} for an introduction to chiral symmetry. The problem of breaking chiral symmetry while removing the doublers is a fundamental problem of lattice QCD known as the *Nielsen-Ninomiya theorem*, which states that one can not have a chiral and doubler free action at the same time (see [5] and references therein). We stress that the second-derivative like term can formally be introduced from the continuum through a so-called *isospectral transformation*, which is a spectrum-conserving redefinition of the fermion fields. Higher order operators introduced through isospectral transformations can be used to reduce the discretization errors of the lattice action [11][12].

2.3. The Connection between the Link Variables and the Continuum Gauge Fields

Before we construct a gauge action for the gluons, we point out the connection between the group-valued link variables and the algebra-valued continuum gauge fields. The link variables connect two lattice sites and ensure gauge-invariance of products of two fermion fields at different lattice sites. In analogy, one can define gauge

transporters in the continuum theory with a transformation property according to [13]

$$G(x,y) \to G'(x,y) = \Omega(x)\ G(x,y)\ \Omega(y)^\dagger\ . \tag{2.3.1}$$

They are called gauge transporters as they ensure that $\psi(y)$ and $G(y,x)\psi(x)$ transform the same way under gauge transformations. Again, they are $\mathrm{SU}(N_c)$ group-valued and have the property $G(y,y) = \mathbb{I}$. Being unitary matrices, the gauge transporters can be expanded by hermitian matrices around $G = \mathbb{I}$, leading to

$$G(x + dx_\mu, x) = \mathbb{I} + i\ A^i_\mu(x) T^i dx_\mu + O(\epsilon^2)\ , \tag{2.3.2}$$

where the continuum gluon fields are given by $A_\mu(x) = A^i_\mu(x)T^i$ with T^i the hermitian generators of the group $\mathrm{SU}(N_c)$. By using products of infinitesimal gauge transporters, one can build up the gauge transporter between arbitrary space time points x and y according to [1]

$$G(y,x) = \prod_i G_i = P \exp\left(i \int_x^y A_\mu(x) dx_\mu \right)\ , \tag{2.3.3}$$

with the infinitesimal gauge transporters given by

$$G_i = 1 + i \int_{x_i}^{x_i+\epsilon_i} A_\mu(x) dx_\mu\ . \tag{2.3.4}$$

The path-ordering ensures the right order of the gauge fields during the gauge transport. Thus, one identifies the link variables on the lattice as discrete versions of the gauge transporters according to [10]

$$U_\mu(n) = \exp\left(ia\ A_\mu\left(n + \frac{\hat{\mu}}{2}\right)\right)\ . \tag{2.3.5}$$

The integral in the exponential of the gauge transporter got approximated by the midpoint rule. Through the path-ordering the links in negative direction are readily defined as

$$U_{-\mu}(n) = \exp\left(-ia\ A_\mu\left(n - \frac{\hat{\mu}}{2}\right)\right) = U_\mu(n - \hat{\mu})^\dagger\ . \tag{2.3.6}$$

Having this connection, one can calculate the continuum limit of the naive fermion action, which is done in appendix {A.2}.

[1] $e^x = \lim_{n\to\infty}(1 + \frac{x}{n})^n$

2.4. Wilson Gauge Action

Having found the relation between the link variables and the continuum gauge fields, one can build up a gauge action on the lattice, which, like the fermion action, has to approach the continuum gauge action in the naive continuum limit $a \to 0$. Again, The gauge action is required to be gauge invariant. Using the gauge transformations of the fermion fields (2.1.4),(2.1.5) and of the link variables (2.1.7), one finds that there are two possibilities to build up gauge invariant objects on the lattice [5]:

1. Two quark fields connected by a path-ordered product of link variables:

$$\bar{\psi}(n_0) \left[\prod_{(n,\mu)\in\mathscr{P}} U_\mu(n) \right] \psi(n_1) \tag{2.4.1}$$

2. The trace of a closed loop of link variables:

$$\mathrm{tr} \left[\prod_{(n,\mu)\in\mathscr{L}} U_\mu(n) \right] \tag{2.4.2}$$

Closed loops of link variables are so-called *Wilson loops*. The simplest Wilson loop is the 1×1 plaquette

$$\begin{aligned} P_{\mu\nu}(n) &= U_\mu(n)\ U_\nu(n+\hat{\mu})\ U_\mu(n+\hat{\nu})^\dagger\ U_\nu(n)^\dagger \\ &= e^{iaA_\mu(n+\frac{\hat{\mu}}{2})}\ e^{iaA_\nu(n+\hat{\mu}+\frac{\hat{\nu}}{2})}\ e^{-iaA_\mu(n+\hat{\nu}+\frac{\hat{\mu}}{2})}\ e^{-iaA_\nu(n+\frac{\hat{\nu}}{2})}\ , \end{aligned} \tag{2.4.3}$$

illustrated in figure (2.1). By using the Baker-Campbell-Hausdorff formula

$$e^A\ e^B = e^{A+B+\frac{1}{2}[A,B]} \tag{2.4.4}$$

and Taylor expansions for the gluon fields, it can be expressed as

$$P_{\mu\nu}(n) = e^{ia^2 F_{\mu\nu}(n) + O\left(a^3\right)}\ . \tag{2.4.5}$$

From this it is easy to see that a lattice gauge gauge action, first proposed by Wilson, can be constructed like

$$S_G[U] = \frac{2N_c}{g^2} \sum_{n\in\Lambda} \sum_{\mu>\nu} \left(1 - \frac{1}{N_c} \mathrm{Re}\ \mathrm{tr}\left(P_{\mu\nu}\right) \right)\ . \tag{2.4.6}$$

It can be expanded like

$$S_G[U] = \frac{a^4}{2g^2} \sum_{n\in\Lambda} \left[\sum_{\mu,\nu} \mathrm{tr}\left[F_{\mu\nu}(n)^2\right]\ +\ O\left(a^2\right) \right] \tag{2.4.7}$$

and therefore has the right continuum limit (remember that $a^4 \sum_{n\in\Lambda} \to \int d^4x$). Usually, the prefactor of the action is combined to the inverse coupling $\beta = \frac{2N_c}{g^2}$. It is important to mention, that the Wilson gauge action (2.4.6) is not unique and larger Wilson loops can be used to reduce discretization errors. For example, the discretization error of $O(a^2)$ of the Wilson gauge action can be reduced to $O(a^4)$ by using additional rectangular loops like

$$R_{\mu\nu}(n) = U_\nu(n)\; U_\mu(n+\hat{\nu})\; U_\mu(n+\hat{\mu}+\hat{\nu})\; U_\nu(n+2\hat{\mu})^\dagger\; U_\mu(n+\hat{\mu})^\dagger\; U_\mu(n)^\dagger\;, \tag{2.4.8}$$

shown in figure (2.2). Defining the relations

$$\tilde{P}_{\mu\nu} = 1 - \frac{1}{N_c}\mathrm{Re}\ \mathrm{tr}(P_{\mu\nu}) \tag{2.4.9}$$

$$\tilde{R}_{\mu\nu} = 1 - \frac{1}{N_c}\mathrm{Re}\ \mathrm{tr}(R_{\mu\nu}) \tag{2.4.10}$$

an improved gauge action with discretization errors starting at $O(a^4)$ can be written as [14]

$$S_G^{imp}[U] = \beta \sum_{n\in\Lambda}\sum_{\mu>\nu}\left(\frac{5\tilde{P}_{\mu\nu}}{3} - \frac{\tilde{R}_{\mu\nu}+\tilde{R}_{\nu\mu}}{12}\right)\;. \tag{2.4.11}$$

M. Lüscher and P. Weisz showed an elegant way to calculate the continuum limits of even more different loops of link-variables and how their coefficients have to be chosen for an improved action, leading to Symanzik's tree-improved action [15].

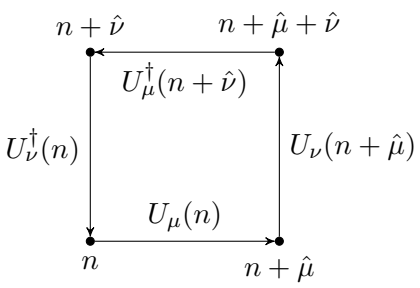

Figure 2.1.: The Plaquette $P_{\mu\nu}$.

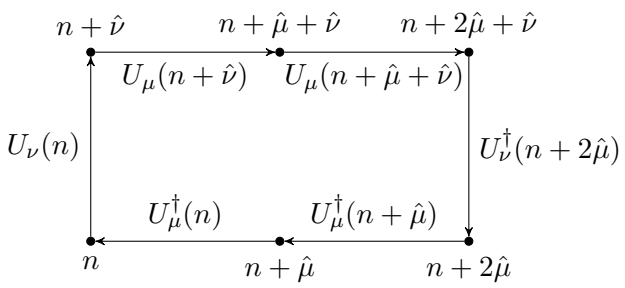

Figure 2.2.: The Rectangle $R_{\mu\nu}$.

2.5. The QCD Path Integral on the Lattice

In lattice QCD the values of physical observables are obtained by calculating the expectation value of the associated operators using the lattice path integral. The fundamental degrees of freedom are the quark fields $\psi(n)$ and $\bar{\psi}(n)$ and the gluon

fields represented by link variables $U_\mu(n)$. Hence for the lattice path integral, one has to integrate over all configurations of quark fields and link variables, and the partition function reads [5]

$$Z = \int \mathcal{D}[U]\mathcal{D}[\psi,\bar{\psi}]\ e^{-S_F[\psi,\bar{\psi},U]-S_G[U]}\ , \tag{2.5.1}$$

so that the expectation values of an operator O is calculated according to

$$\langle O\rangle = \frac{1}{Z}\int \mathcal{D}[U]\mathcal{D}[\psi,\bar{\psi}]\ O[\psi,\bar{\psi},U]\ e^{-S_F[\psi,\bar{\psi},U]-S_G[U]}\ . \tag{2.5.2}$$

The integration measures of the link variables and the fermion fields are introduced in the next sections. Numerical methods for the calculation of expectation values are shown in section {4}.

2.5.1. Haar Measure

The integral measure of the link variables in lattice QCD is defined as the product of all measures for the individual link variables

$$\int \mathcal{D}[U] = \prod_{n\in\Lambda}\prod_{\mu=1}^{4}\int dU_\mu(n)\ , \tag{2.5.3}$$

where the integral of a link variable is over the whole group manifold of $\mathrm{SU}(N_c)$. The path integral should be invariant under a change of variables, therefore we require invariance under the gauge transformation of the link variables (2.1.7)

$$Z = \int \mathcal{D}[U]\ e^{-S_G[U]} = \int \mathcal{D}[U']\ e^{-S_G[U']}\ . \tag{2.5.4}$$

The gauge action is gauge invariant by construction and thus the measure of the link variables has to satisfy

$$dU_\mu(n) = dU'_\mu(n) = d(\Omega(n)\ U_\mu(n)\ \Omega(n+\hat{\mu})^\dagger)\ . \tag{2.5.5}$$

This leads to the so-called *Haar measure* [5]. It defines the integration of group elements over a continuous compact group G. There are two defining properties of the Haar measure:

1. $\forall V \in G : dU = d(UV) = d(VU)$
2. $\int \mathbb{I}\ dU = \mathbb{I}$

Where the first property is just the required gauge invariance and the second property is a normalization. G being a compact Lie group, the group elements U can be parametrized by a set of real numbers ω^k. Furthermore, it can be shown that $\frac{\partial U(\omega)}{\partial \omega^k}U(w)^{-1}$ lies in the Lie algebra of the group [5]. Thus, one defines a metric on the group through the coordinates in the Lie algebra space as [5]

$$
\begin{aligned}
ds^2 &= g(\omega)_{nm} d\omega^n d\omega^m \\
&= \mathrm{tr}\left[\frac{\partial U(\omega)}{\partial \omega^n} U(w)^{-1} \left(\frac{\partial U(\omega)}{\partial \omega^m} U(w)^{-1}\right)^\dagger\right] d\omega^n d\omega^m \\
&= \mathrm{tr}\left[\frac{\partial U(\omega)}{\partial \omega^n} \frac{\partial U(\omega)}{\partial \omega^m}^\dagger\right] d\omega^n d\omega^m \ .
\end{aligned}
\tag{2.5.6}
$$

Using the metric $g(\omega)$, the measure of a group element dU can be written as a product of the measures of the real parameters ω^k

$$
dU = c\sqrt{\det(g(\omega))} \prod_k d\omega^k \ , \tag{2.5.7}
$$

where the constant c gets chosen to ensure the normalization condition.

2.5.2. Grassmann Integration

Like the integral measure of the link variables, the integral measure of the quark fields is also defined as a product of measures of all individual quark field components on the lattice

$$
\mathcal{D}[\psi, \bar{\psi}] = \prod_{n\in\Lambda} \prod_{\alpha,a} d\psi(n)_{\alpha a} \ d\bar{\psi}(n)_{\alpha a} \ . \tag{2.5.8}
$$

Being fermions, the quark fields have to obey Pauli's principle. This can be achieved by treating all fermionic degrees of freedom as anti-commuting numbers, so-called *Grassmann numbers* (see [2] for their properties). From the naive fermion action (2.1.9) or the Wilson action (2.2.5), it can be seen that the fermion action is linear in the quark fields. Thus, the fermion action can be written as a matrix product

$$
S_F[\psi, \bar{\psi}, U] = \bar{\psi} \ D[U] \ \psi = \sum_{A,B} \bar{\psi}_A \ D[U]_{AB} \ \psi_B \ , \tag{2.5.9}
$$

with A and B being multi-indices including space-time, Dirac- and color-space. Using this, the fermionic part of the partition function (2.5.1) can be written as

$$
Z_F[U] = \int d\psi_N d\bar{\psi}_N \cdots d\psi_1 d\bar{\psi}_1 \ \exp\left(\sum_{A,B} \bar{\psi}_A \ D[U]_{AB} \ \psi_B\right) \ . \tag{2.5.10}
$$

Now, one can do a change of variables, introducing a determinant of the Dirac operator in the integral [5]

$$
\psi'_A = \sum_B D[U]_{AB} \ \psi_B \quad \rightarrow \quad d^N\psi = \det\left(D[U]\right) \ d^N\psi' \ . \tag{2.5.11}
$$

Therefore, the fermionic part of the partition function can be simplified to

$$
\begin{aligned}
Z_F[U] &= \det\left(D[U]\right) \int d\psi'_N d\bar{\psi}_N \cdots d\psi'_1 d\bar{\psi}_1 \ \exp\left(\sum_A \bar{\psi}_A \psi'_A\right) \\
&= \det\left(D[U]\right) \prod_A \int d\psi'_A d\bar{\psi}_A \ \exp\left(\bar{\psi}_A \psi'_A\right) = \det\left(D[U]\right) \ .
\end{aligned}
\tag{2.5.12}
$$

In the first step the fact that a pair of Grassmann numbers commutes with every other pair of Grassmann numbers and in the second step the nilpotency of Grassman numbers has been used. The lattice QCD path integral (2.5.1) reduces to one over the gauge degrees of freedom only

$$
Z = \int \mathcal{D}[U] \ \det\left(D[U]\right) \ e^{-S_G[U]} \ . \tag{2.5.13}
$$

For the calculation of n-point functions, one introduces the generating functional for fermions. It is given by the fermionic part of the partition function with additional sources θ and $\bar{\theta}$ for the fermion fields

$$
W[\theta, \bar{\theta}] = \int \prod_C d\psi_C d\bar{\psi}_C \ \exp\left(\sum_{A,B} \bar{\psi}_A \ D[U]_{AB} \ \psi_B + \sum_A \bar{\theta}_A \psi_A + \sum_A \bar{\psi}_A \theta_A\right) \ . \tag{2.5.14}
$$

After completing the square in the exponent and a transformation of variables one finds [5]

$$
W[\theta, \bar{\theta}] = \det\left(D[U]\right) \ \exp\left(-\sum_{A,B} \bar{\theta}_A \ \left(D[U]^{-1}\right)_{AB} \ \theta_B\right) \ . \tag{2.5.15}
$$

The calculation of a n-point function can now easily be done. From equation (2.5.14) one sees that it can be written as the derivatives of the generating functional and using the form of (2.5.15) these derivatives can easily be calculated, leading to

$$
\begin{aligned}
\left\langle \psi_{A_1} \bar{\psi}_{B_1} \cdots \psi_{A_N} \bar{\psi}_{B_N} \right\rangle_F &= \frac{1}{Z_F} \frac{\partial}{\partial \theta_{A_1}} \frac{\partial}{\partial \bar{\theta}_{B_1}} \cdots \frac{\partial}{\partial \theta_{A_N}} \frac{\partial}{\partial \bar{\theta}_{B_N}} \ W[\theta, \bar{\theta}]\Big|_{\theta=\bar{\theta}=0} \\
&= (-1)^N \sum_{P(1,2,\ldots,N)} \mathrm{sign}(P) \ \left(D^{-1}\right)_{A_1 B_{P_1}} \cdots \left(D^{-1}\right)_{A_N B_{P_N}} \ ,
\end{aligned}
\tag{2.5.16}
$$

where the subscript F means that the calculation includes only the fermionic part of the path integral, it still depends on the gluon fields through the Dirac operator. This result is the so-called *Wick theorem*.

To include the gluonic part of the path integral, one needs to calculate

$$\left\langle \psi_{A_1}\bar{\psi}_{B_1}\cdots\psi_{A_N}\bar{\psi}_{B_N}\right\rangle = \frac{1}{Z}\int \mathcal{D}[U]\ Z_F[U]\ \left\langle \psi_{A_1}\bar{\psi}_{B_1}\cdots\psi_{A_N}\bar{\psi}_{B_N}\right\rangle_F\ e^{-S_G[U]}\ . \tag{2.5.17}$$

2.6. The Polyakov Loop

One of the elementary properties of QCD is the occurrence of a deconfinement phase transition, which is a true phase transition only in the quenched limit. In this section, we will introduce the order parameter for this transition, the so-called *Polyakov loop*. The considerations in this chapter are done for pure gauge theory, where the quark masses become infinitely heavy and no dynamical quark excitations are possible. The reasons for this restriction become clear during the section. We start our consideration in the continuum and then make the connection to the lattice. An infinitely heavy quark at a position $\vec{x}$ in continuous spacetime can only propagate in time and corresponds to the current

$$j_\mu(\vec{y}) = \delta\left(\vec{y}-\vec{x}\right)\ \vec{e}_t\ , \tag{2.6.1}$$

with $\vec{e}_t$ being the four-dimensional unit vector in time direction. In QCD the current of a static charge couples to the gauge field and can be observed through the operator [5]

$$O = \mathrm{tr}\left[Pe^{i\int d^4y j_\mu(y)A_\mu(y)}\right]\ . \tag{2.6.2}$$

Plugging in the current (2.6.1), we obtain

$$O = \mathrm{tr}\left[Pe^{i\int dt A_4(x)}\right]\ . \tag{2.6.3}$$

Now, we transfer this observable on the lattice by remembering the connection between the link variables and the gauge fields pointed out in section {2.3}. The result is the Polyakov loop, which therefore describes the propagation of a static quark on the lattice, given by

$$P(\vec{n}) = \mathrm{tr}\left[\prod_{i=0}^{N_t-1} U_4(\vec{n},i)\right]\ . \tag{2.6.4}$$

The Polyakov loop winds around the lattice in time direction once. Hence, we can find a connection of the correlation between a Polyakov loop in positive time direction and a Polyakov loop in negative time direction to the free energy of a static quark and anti-quark separated by $r = |\vec{n}-\vec{m}|$, given by (see [5] for a more detailed discussion)

$$\left\langle P(\vec{n})P(\vec{m})^\dagger\right\rangle \propto e^{-aN_tF_{\bar{q}q}(ar)}\ . \tag{2.6.5}$$

For large distances the Polyakov loop correlator (2.6.5) factorises and approaches $|\langle P\rangle|^2$ and thus the Polyakov loop expectation value is connected to the free energy of a single static charge by [16]

$$|\langle P\rangle| = \frac{1}{N_s^3}\left\langle \sum_{\vec{n}\in\Lambda} P(\vec{n})\right\rangle \sim e^{-\frac{F_q}{T}} \ , \tag{2.6.6}$$

where we used the connection of the temperature with the temporal size of the lattice $T = \frac{1}{aN_t}$, which will be pointed out in section {5.1}. In a regime where the theory is confining the free energy of a single static quark is infinity as it is not possible to separate a single charged particle. For the regime where the theory is deconfining a finite amount of energy is needed to separate a single charged particle and thus for a theory with a phase transition at some critical temperature T_c the Polyakov loop can be used as order parameter

$$\begin{array}{llll} \textbf{confinement} & F_q = \infty & \Longrightarrow & |\langle P\rangle| = 0 \ \text{ for } T < T_c \ , \\ \textbf{deconfinement} & F_q = \text{finite} & \Longrightarrow & |\langle P\rangle| > 0 \ \text{ for } T > T_c \ . \end{array}$$

This is not true anymore, when we are including dynamical quark excitations as in the separation of two charged particles dynamical quark-antiquark pairs can be created, which leads to a finite free energy of a static quark even in the confined regime. This is often denoted by the so-called *string breaking*. Notice that for periodic boundary conditions for the link variables, the Polyakov loop is invariant under the gauge transformations defined by equation (2.1.7)

$$\begin{aligned} P(\vec{n}) \to P'(\vec{n}) &= \mathrm{tr}\left[\prod_{i=0}^{N_t-1} \Omega(\vec{n},i)\ U_4(\vec{n},i)\ \Omega^\dagger(\vec{n},i+1)\right] \\ &= \mathrm{tr}\left[\Omega(\vec{n},0)\ \left(\prod_{i=0}^{N_t-1} U_4(\vec{n},i)\right)\Omega^\dagger(\vec{n},N_t)\right] \\ &= \mathrm{tr}\left[\prod_{i=0}^{N_t-1} U_4(\vec{n},i)\right] \ . \end{aligned} \tag{2.6.7}$$

2.7. The Bulk Phase

Let us now discuss another phase transition, the so-called *bulk phase transition*. It describes the transition from an artificial phase, due to topological lattice artifacts, to a physical phase [6]. The transition disappears in the continuum limit $\beta \to \infty$, but can influence the physical transitions happening at finite β, which one wants to observe. In $SU(2)$ pure gauge theory such a bulk phase transition is visible. The (pseudo) order parameter of this transition is the $\mathbb{Z}(2)$ monopole density, measuring the condensation of $\mathbb{Z}(2)$ magnetic monopoles [6]. It is measured according to

$$M = 1 - \frac{1}{N_C} \sum_C \prod_{P_{\mu\nu} \in \partial C} \text{sign}\left(\text{tr } P_{\mu\nu}\right) \ , \tag{2.7.1}$$

where the sum runs over all N_C 3-cubes of the lattice. The value of the $\mathbb{Z}(2)$ monopole density crucially depends on the local distribution of the plaquettes $P_{\mu\nu}$. With larger inverse coupling β the fraction of positive sign plaquettes increases [6], leading to a vanishing $\mathbb{Z}(2)$ monopole density. Being a lattice artifact, the bulk phase can be suppressed by using improved gauge actions, like equation (2.4.11). It is evident from figure (2.3), that the bulk phase transition is shifted to smaller inverse couplings, when using the improved gauge action. Including dynamical fermions lowers the $\mathbb{Z}(2)$ monopole density only a little bit, which we will later confirm with our simulations at non-vanishing chemical potential. Furthermore, it has been seen that the $\mathbb{Z}(2)$ monopole density is nearly independent of the lattice volume [6]. Simulations inside the bulk phase lead, for example, to an unphysical contribution to the chiral susceptibility [6]. Thus in general, we need to simulate at values of the inverse coupling β which are outside the bulk phase. On the other side, a large β leads to a small lattice spacing a and hence to avoid finite volume effects the lattice volume $N_s^3 \times N_t$ has to be large enough. Simulations at large lattice volumes are expensive, so that often a compromise between bulk phase effects and finite volume effects is made. Another problem is that the chiral transition is close to the bulk phase transition and employing the improved gauge action shifts the chiral transition with nearly the same $\Delta\beta$ to smaller inverse couplings β [6]. Thus, using large enough β to be outside the bulk phase often means that one already overpassed the chiral transition, which one might want to observe.

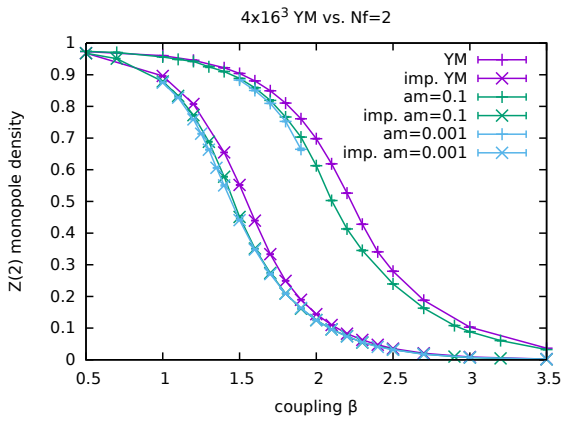

Figure 2.3.: The $\mathbb{Z}(2)$ monopole density for unimproved and improved gauge action and in dependence of the quark mass [6].

3. Staggered Fermions

This section will introduce the lattice fermion formalism used in this work. In section {4}, we will show how to include it in the Hybrid Monte Carlo algorithm for numerical calculations of observables with the full path integral. We already introduced standard Wilson fermions in section {2.2}. They are widely used for spectroscopy as they allow a straightforward formulation of correlation functions. Unfortunately, standard Wilson fermions have the problem of explicitly breaking chiral symmetry on the lattice, even in the case of massless fermions, through the second-derivative-like term (2.2.2). Hence, they are not really suitable for the calculation of the phase diagram, for which one has to be able to observe the spontaneous breaking of chiral symmetry. All calculations including dynamical fermions in this work were done with *staggered fermions*. They are computationally cheap and have a remnant chiral symmetry and thus are a good choice for thermodynamic simulations.

3.1. The Staggered Transformation

The action for staggered fermions is obtained through the staggered transformation defined as [5]

$$\psi(n) = \gamma_1^{n_1}\gamma_2^{n_2}\gamma_3^{n_3}\gamma_4^{n_4}\ \psi(n)' \ , \tag{3.1.1}$$

$$\bar{\psi}(n) = \bar{\psi}(n)'\ \gamma_1^{n_1}\gamma_2^{n_2}\gamma_3^{n_3}\gamma_4^{n_4} \ , \tag{3.1.2}$$

with the new field variables $\psi(n)'$ and $\bar{\psi}(n)'$. Obviously, this transformation mixes space-time and Dirac indices. When plugging in the staggered transformation for the fermion fields into the naive fermion action, all Dirac matrices will cancel, resulting only in factors of (-1) due to the anti-commutation (see (A.1.2)). Thus, the action becomes diagonal in Dirac-space and we can drop three of the four equal components. We treat the remanent component as the new fermion field $\chi(n)$ and $\bar{\chi}(n)$, whose action is written as

$$S_F[\chi,\bar{\chi}] = a^4 \sum_{n\in\Lambda} \bar{\chi}(n) \left(\sum_{\mu=1}^{4} \eta_\mu(n) \frac{U_\mu(n)\chi(n+\hat{\mu}) - U_{-\mu}(n)\chi(n-\hat{\mu})}{2a} + m\chi(n) \right) \ , \tag{3.1.3}$$

with the so-called *staggered phases*

$$\eta_1(n) = 1 \ , \ \eta_2(n) = (-1)^{n_1} \ , \ \eta_3(n) = (-1)^{n_1+n_2} \ , \ \eta_4(n) = (-1)^{n_1+n_2+n_3} \ . \tag{3.1.4}$$

To address the question of how many continuum flavors the staggered action actually describes, we refer to the next section.

3.2. The Spin-Taste Transformation

In the last section, we have seen that the staggered transformation diagonalized the naive fermion action in Dirac space and therefore we dropped three of the four equal components, introducing the staggered fermion field. To find the number of flavors described by one staggered fermion field, it is important to note that the space-time and Dirac indices of the original fermion field got mixed during the staggered transformation. Thus the suggestion comes up, that through a linear combination of staggered fermion fields at different lattice sites the Dirac structure could be restored. Indeed, by grouping together the 16 sites of a hypercube we will recover a 4-spinor structure for four different species of fermions [5][9][11]. These species are the so-called *tastes* of a staggered fermion. Hence, we will conclude that the staggered action describes a theory with $N_f = 4$ quark flavors. Here, we assume that in every direction of the lattice we have an even number of lattice sites. The sum over all lattice sites will be replaced by a sum over the hypercubes and a sum over the corners of the hypercubes, where the fermion fields are located,

$$\sum_{n\in\Lambda} \to \sum_{y\in\Lambda'} \sum_{s} \ , \tag{3.2.1}$$

with

$$\Lambda' = \left\{ y = (y_1, y_2, y_3, y_4) \ \mid y_\mu = 0, 1, 2, ..., \frac{N_\mu}{2} - 1 \right\} \ , \quad s_\mu = 0, 1 \ . \tag{3.2.2}$$

Defining matrices Γ_s, which depend on the corner of the hypercube, as

$$\Gamma_s = \gamma_1^{s_1} \gamma_2^{s_2} \gamma_3^{s_3} \gamma_4^{s_4} \ , \tag{3.2.3}$$

we can introduce new fields $q(y)$ and $\bar{q}(y)$ through the so-called *spin-taste transformation* [5]

$$\begin{aligned} q(y)_{\alpha a} &= \frac{1}{8} \sum_s \Gamma_{s,\alpha a} \ \chi(2y+s) \ , \\ \bar{q}(y)_{a\alpha} &= \frac{1}{8} \sum_s \bar{\chi}(2y+s) \ \Gamma^\dagger_{s,a\alpha} \ . \end{aligned} \tag{3.2.4}$$

The matrix indices of the Γ_s matrices are explicitly shown. We identify the greek index $\alpha = 1, 2, 3, 4$ as the Dirac index and the latin index $a = 1, 2, 3, 4$ as the taste index. Notice that the color structure of the q and $\bar{q}$ fields is the same as of the χ and $\bar{\chi}$ fields. In appendix {A.10}, we use the spin-taste transformation to transform

the staggered action (3.1.3) in the free case $U_\mu = \mathbb{I}$ from the spin basis with fields χ and $\bar{\chi}$ into the taste basis with fields q and $\bar{q}$ and obtain

$$S_F[q,\bar{q}] = b^4 \sum_y \bar{q}(y) \left\{ m\,(\mathbb{I}\otimes\mathbb{I}) + \sum_\mu \left[(\gamma_\mu \otimes \mathbb{I})\,\nabla_\mu - \frac{b}{2}\,(\gamma_5 \otimes t_5 t_\mu)\;\Delta_\mu \right] \right\} q(y)\ , \tag{3.2.5}$$

where $b = 2a$ and $t_\mu = \gamma_\mu^T$. The first two terms of this action are diagonal in taste space and have exactly the same form as the naive Wilson action (2.1.3). They describe a theory of four independent tastes of quarks and thus, as already mentioned, we conclude that one staggered fermion describes a theory with $N_f = 4$. The third term in the staggered action in taste basis explicitly breaks taste symmetry, but vanishes in the continuum limit and therefore does not affect the continuum propagator. Thus, it has the same behaviour as the second-derivative like term of Wilson fermions (2.2.2), which explicitly breaks chiral symmetry and vanishes in the continuum limit, too. Looking at the kinetic term of the staggered action in taste basis without the taste breaking term, we find that it is invariant under independent vector and axial rotations for each taste given by

$$q' = e^{i\alpha}\ q\ , \qquad \bar{q}' = \bar{q}\ e^{-i\alpha}\ , \tag{3.2.6}$$

$$q' = e^{i\beta\gamma_5}\ q\ , \qquad \bar{q}' = \bar{q}\ e^{i\beta\gamma_5}\ . \tag{3.2.7}$$

The taste breaking term is not invariant under the rotations (3.2.7) and breaks them down to [5]

$$q' = e^{i\beta\tau_5}\ q\ , \qquad \bar{q}' = \bar{q}\ e^{i\beta\tau_5}\ , \tag{3.2.8}$$

with the taste-mixing generator $\tau_5 = \gamma_5 \otimes t_5$, leaving a remaining $U(1)\times U(1)$ symmetry group. Including the mass term of the action breaks the symmetry further down to a remaining $U(1)_V$ symmetry group given by the rotations (3.2.6), corresponding to a conserved quark number. If gauge fields are included in both formulations of the staggered action, taste and spin basis, it can be shown that for general gauge fields both formulations are not equivalent [17]. The formulations are only equivalent if the link variables are related via

$$U_\mu(n) = \begin{cases} U_\mu(y) & \text{for } n = 2y + s\ ,\ s_\mu = 1 \\ \mathbb{I} & \text{elsewhere} \end{cases}\ , \tag{3.2.9}$$

meaning that the gauge fields in the spin basis formulation only couple fields which belong to different hypercubes.

3.3. The Chiral Symmetry

Another central properties of QCD is chiral symmetry and its spontaneous breaking, meaning that even though the Lagrangian is chirally symmetric the ground state of the theory is not. The quark masses even break the chiral symmetry explicitly. As the quark masses for the light quarks (u,d) are very small, one treats chiral symmetry as an approximate symmetry of two-flavor QCD. The breaking of a symmetry leads to the appearance of Goldstone bosons, in this case the pions. Furthermore, the pions gain their small masses from the explicit breaking of the chiral symmetry. Being such an important property of QCD, we want to have a proper implementation of chiral symmetry on the lattice. This has been a hard task in the past, leading to the *Nielsen-Ninomya theorem*, as already noted in section {2.2}. In this section, we will introduce the basic concepts about chiral symmetry and its order parameter, the chiral condensate, in the continuum as well as on the lattice.

3.3.1. The Chiral Rotations

Consider a Lagrangian for a theory of N_f quark flavors

$$\mathcal{L} = \bar{\psi}\ (\not{D} + M)\ \psi\ , \tag{3.3.1}$$

where $\not{D} = \gamma_\mu(\partial_\mu + iA_\mu)$ is the massless Dirac operator and $M = \mathrm{diag}(m_1, m_2, ..., m_{N_f})$ is the mass matrix. We employed vector notation, meaning that the different flavors are components of the vector ψ. With the help of the left- and right-handed projection operators

$$P_L = \frac{1}{2}(1+\gamma_5)\ ,\quad P_R = \frac{1}{2}(1-\gamma_5)\ , \tag{3.3.2}$$

the Dirac field in the Lagrangian can be decomposed in its left- and right-handed components, leading to [18]

$$\mathcal{L} = \bar{\psi}_R \not{D} \psi_R + \bar{\psi}_L \not{D} \psi_L + M\left(\bar{\psi}_R \psi_L + \bar{\psi}_L \psi_R\right)\ . \tag{3.3.3}$$

In the massless case $M = 0$ the left- and right-handed components contribute independently to the Lagrangian. Therefore, the Lagrangian is symmetric under independent unitary transformations

$$\psi_{L,R} \to U_{L,R}\ \psi_{L,R}\ , \tag{3.3.4}$$

leading to the symmetry group $U(N_f)_L \times U(N_f)_R$ which can be decomposed to

$$SU(N_f)_L \times SU(N_f)_R \times U(1)_V \times U(1)_A\ . \tag{3.3.5}$$

For the investigation of the different transformations contributing to the symmetry group $U(N_f)_L \times U(N_f)_R$, we employ vector notation again

$$\psi = \begin{pmatrix} \psi_L \\ \psi_R \end{pmatrix} \to \psi' = \begin{pmatrix} \psi'_L \\ \psi'_R \end{pmatrix} = \begin{pmatrix} U_L & 0 \\ 0 & U_R \end{pmatrix} \begin{pmatrix} \psi_L \\ \psi_R \end{pmatrix} = U\ \psi\ . \tag{3.3.6}$$

The corresponding transformation to the $U(1)_V$ symmetry group is given by

$$\psi' = e^{i\alpha\mathbb{I}}\ \psi\ ,\quad \bar{\psi}' = \bar{\psi}\ e^{-i\alpha\mathbb{I}}\ . \tag{3.3.7}$$

This symmetry is the origin of quark number conservation. Finally, *the chiral rotations*, belonging to the part of $U(N_f)_L \times U(N_f)_R$ with $U_L = U_R^\dagger$, are given by

$$\psi' = e^{i\alpha\gamma_5\mathbb{I}}\ \psi\ ,\quad \bar{\psi}' = \bar{\psi}\ e^{i\alpha\gamma_5\mathbb{I}}\ , \tag{3.3.8}$$

$$\psi' = e^{i\alpha\gamma_5 T_i}\ \psi\ ,\quad \bar{\psi}' = \bar{\psi}\ e^{i\alpha\gamma_5 T_i}\ . \tag{3.3.9}$$

where T_i are the generators of $\mathrm{SU}(N_f)$. The transformations (3.3.8) belong to the symmetry group $U(1)_A$. This symmetry gets explicitly broken by the non-invariance of the fermion measure due to the *axial anomaly* [2][18][19]. The transformations (3.3.9) are part of the symmetry group $SU(N_f)_L \times SU(N_f)_R$, often denoted as $SU(N_f)_A$. When introducing degenerated masses for the fermions $M = (m, m, ..., m)$, the $SU(N_f)_A$ part is explicitly broken, leaving the subgroup $SU(N_f)_V$ with $U_L = U_R$ of $SU(N_f)_L \times SU(N_f)_R$ as a remaining symmetry, with transformations

$$\psi' = e^{i\alpha T_i}\ \psi\ ,\quad \bar{\psi}' = \bar{\psi}\ e^{-i\alpha T_i}\ . \tag{3.3.10}$$

The transformations (3.3.10) correspond to the isospin transformations of a system of N_f mass degenerated quarks. Lastly, introducing non-degenerated masses for the quarks breaks the $SU(N_f)_V$ symmetry, leaving only a $U(1)_V$ symmetry for each quark flavor according to the baryon number conservation, as already mentioned. Thus we can sum up to [5]:

$$\begin{array}{lcl} U(N_f)_L \times U(N_f)_R & = & SU(N_f)_L \times SU(N_f)_R \times U(1)_V \times U(1)_A \\ \text{invariant measure} & \to & SU(N_f)_L \times SU(N_f)_R \times U(1)_V \\ \text{degenerated masses} & \to & SU(N_f)_V \times U(1)_V \\ \text{non-deg. masses} & \to & U(1)_V \times \cdots \times U(1)_V \quad (N_f \text{ factors}) \end{array}$$

Notice that essential for chiral symmetry is the anti-commutation of the massless Dirac operator with γ_5

$$\{D, \gamma_5\} = D\gamma_5 + \gamma_5 D = 0\ , \tag{3.3.11}$$

as this is required for the decomposition of the Lagrangian into the form of equation (3.3.3). The naive discretization of the lattice fermions (2.1.9) fulfills this requirement and thus is chiral symmetric in the massless limit. Being the starting point of

the staggered action (3.1.3), staggered fermions inherit a remnant chiral symmetry according to the transformations

$$\chi(n) \to e^{i\alpha\eta_5(n)}\ \chi(n)\ ,\quad \bar{\chi}(n) \to \bar{\chi}(n)\ e^{i\alpha\eta_5(n)}\ , \tag{3.3.12}$$

with $\eta_5(n) = (-1)^{n_1+n_2+n_3+n_4}$ the analogue of γ_5 for the staggered formalism.

3.3.2. The Chiral Condensate

The order parameter for the chiral symmetry breaking is the so-called *chiral condensate*

$$\left\langle \bar{\psi}^f \psi^f \right\rangle\ , \tag{3.3.13}$$

which is defined for each flavor f separately. Transforming like a mass term, the chiral condensate is not invariant under the chiral rotations. Thus, a non-vanishing chiral condensate implies the spontaneous breaking of chiral symmetry. Note that in the case of massive quarks the chiral condensate is never zero. Still, due to the small quark masses a phase transition is visible, showing the effect of spontaneous breaking, even though the chiral condensate is no true order parameter any more. With the help of the generating functional (2.5.15), we can express the chiral condensate as the quark propagator

$$\left\langle \bar{\psi}_{\beta b}(y)\psi_{\alpha a}(x)\right\rangle_F = \frac{1}{Z_F}\frac{\partial}{\partial\theta_{\beta b}(y)}\frac{\partial}{\partial\bar{\theta}_{\alpha a}(x)}\ W[\theta,\bar{\theta}]\Big|_{\theta=\bar{\theta}=0} = -\left(D^{-1}\right)_{\alpha\beta,ab}(x,y)\ , \tag{3.3.14}$$

where D is now the full Dirac operator including the mass term. Considering the mean over the gauge configurations and summing over all fermionic degrees of freedom, we arrive at

$$\left\langle \bar{\psi}\psi \right\rangle = -\frac{1}{V}\mathrm{tr}\left\langle D^{-1}\right\rangle\ , \tag{3.3.15}$$

with an additional normalization by the volume V. The mean value is calculated as an average over gauge configurations according to equation (4.0.2) and the trace is approximated with the help of Gaussian distributed noisy estimators $P[\psi_k] \propto \exp(-\bar{\psi}_k\psi_k)$ [20]. Thus, the chiral condensate on the lattice is calculated according to

$$\left\langle \bar{\psi}\psi \right\rangle = -\frac{1}{|\Lambda|}\frac{1}{N_G}\sum_{i=1}^{N_G}\ \frac{1}{N_F}\sum_{k=1}^{N_F}\bar{\psi}_k\left(D^{-1}\right)[U_i]\ \ \psi_k\ , \tag{3.3.16}$$

where N_G is the number of used gauge configurations, N_F is the number of used noisy estimators per gauge configuration and $|\Lambda|$ is the number of lattice points.

4. The Numerical Calculation of Observables from the QCD Path Integral

This section will introduce our method of choice for the numerical calculation of observables from QCD the path integral. We will first show the algorithm for pure gauge theory, meaning that the path integral only has gluonic degrees of freedom, and then include dynamical fermions. Pure gauge theory corresponds to a theory of infinitely heavy quarks. From equation (2.5.2) we see that the expectation value of an observable O in pure gauge theory is given by

$$\langle O \rangle = \frac{1}{Z} \int \mathcal{D}[U] \; O[U] \; e^{-S_G[U]} \; . \tag{4.0.1}$$

We use a *Monte Carlo method* [21] to approximate the path integral over all possible configurations of gauge fields by a sum over a finite subset of configurations

$$\langle O \rangle \approx \frac{1}{N} \sum_{i=1}^{N} O[U_i] \; , \tag{4.0.2}$$

where the gluon configurations U_i are sampled according to the probability distribution density [5]

$$dP(U) = \frac{e^{-S_G[U]} \; \mathcal{D}[U]}{\int \mathcal{D}[U] \; e^{-S_G[U]}} \; . \tag{4.0.3}$$

This sampling is called *importance sampling*, because it takes a weight factor into account. The weight factor corresponds to the canonical equilibrium distribution $p_{eq.}(U) \propto e^{-S_G[U]}$ of the link variables. For the sampling a *Markov chain* of configurations is generated, where the next configuration is calculated from the configuration before, starting from an arbitrary configuration

$$U_0 \to U_1 \to U_2 \to \cdots \; . \tag{4.0.4}$$

The next section presents the algorithm used for the gauge field generation.

4.1. The Hybrid Monte Carlo Algorithm

The Hybrid Monte Carlo algorithm is a global updating algorithm, it changes every link variable on the lattice in one step. Hence, it provides a fast movement through

the configuration space but is computationally costly. The idea is to base the updates on Molecular Dynamics [5][11]. For this, a conjugate momentum $\pi_\mu(n)$ to every link variable $U_\mu(n)$ on the lattice is introduced. Being SU(N_c) group elements, the link variables can be written as an exponential function of a linear product of real parameters, corresponding to the gluon fields, and the generators of the group T_j

$$U_\mu(n) = \exp\left(i \sum_{j=1}^{N_c^2-1} A_\mu^j(n)\ T_j \right) \ . \tag{4.1.1}$$

The canonical momenta are treated as elements of the su(N_c) Lie-Algebra

$$\pi_\mu(n) = \sum_{j=1}^{N_c^2-1} p_\mu^j(n)\ T_j \ . \tag{4.1.2}$$

For the molecular dynamics the Hamiltonian

$$H[\pi, U] = \sum_{n\in\Lambda} \sum_{\mu} \mathrm{tr}\left[\pi_\mu(n)^2\right] + S_G[U] \tag{4.1.3}$$

is used and the evolution is done along a trajectory through the parameter space of the Lie group SU(N_c), leading to the equations of motions given by

$$\frac{d}{d\tau} A_\mu^j(n) = \frac{\partial H}{\partial p_\mu^j(n)} \ , \tag{4.1.4}$$

$$\frac{d}{d\tau} p_\mu^j(n) = -\frac{\partial S_G}{\partial A_\mu^j(n)} \ . \tag{4.1.5}$$

The right-hand sites of these equations of motions can be calculated more explicitly to

$$\frac{\partial H}{\partial p_\mu^j(n)} = \frac{1}{2} \sum_{m\in\Lambda} \sum_{\nu,i} \frac{\partial p_\nu^i(m)^2}{\partial p_\mu^j(n)} = p_\mu^j(n) \ , \tag{4.1.6}$$

$$\begin{aligned} \frac{\partial S_G}{\partial A_\mu^j(n)} &= \frac{\partial \exp\left(i \sum_i A_\mu^i(n)\ T_i\right)_{ab}}{\partial A_\mu^j(n)} \frac{\partial S_G}{\partial \exp\left(i \sum_i A_\mu^i(n)\ T_i\right)_{ab}} \\ &= i\ (T_j)_{ae} U_\mu(n)_{eb} \frac{\partial S_G}{\partial U_\mu(n)_{ab}} \ . \end{aligned} \tag{4.1.7}$$

In the calculation of the derivative of the gauge action the color indices have been written explicitly, as they do not contract trivially. The imaginary i appearing in the last line can be absorbed into the conjugate momentum parameter and hence $ip_\mu^j(n)$ will be treated as the parameter for the anti-hermitian conjugate momentum $i\pi_\mu(n)$. Having the equations of motion for the parameters, the according equations

of motion for the link variables and conjugate momenta can be calculated, one arrives at

$$\begin{aligned}\frac{d}{d\tau}U_\mu(n) &= U_\mu(n)\left(i\sum_j\left(\frac{d}{d\tau}A^j_\mu(n)\right)T_j\right)\\ &= U_\mu(n)\left(i\sum_j p^j_\mu(n)T_j\right)\\ &= U_\mu(n)\left(i\pi_\mu(n)\right)\ ,\end{aligned} \tag{4.1.8}$$

$$\begin{aligned}\frac{d}{d\tau}\left(i\pi_\mu(n)\right)_{fg} &= \sum_j \frac{d}{d\tau}\left(ip^j_\mu(n)\right)(T_j)_{fg}\\ &= \sum_j (T_j)_{ae}U_\mu(n)_{eb}\frac{\partial S_G}{\partial U_\mu(n)_{ab}}\ (T_j)_{fg}\\ &= U_\mu(n)_{fb}\frac{\partial S_G}{\partial U_\mu(n)_{gb}}\Big|_{TA}\ \equiv\ F_{G,\mu}(n)_{fg}\Big|_{TA}\ .\end{aligned} \tag{4.1.9}$$

The evolution of the conjugate momentum is driven by the so-called *force term* $F_{G,\mu}(n)$. It has to be traceless and anti-hermitian, as the $i\pi_\mu(n)$, and therefore a projection of the kind

$$A\Big|_{TA} = \frac{1}{2}\left(A - A^\dagger\right) - \frac{1}{2N_c}\mathrm{tr}\left(A - A^\dagger\right) \tag{4.1.10}$$

is used, which is shown more explicitly in appendix {A.3}. The explicit calculation of the force term depends on the used gauge action. In appendix {A.4} the force term for the Wilson gauge action (2.4.6) and in appendix {A.5} the force term for the improved gauge action (2.4.11) is shown. When introducing dynamical fermions, there will be an additional force term according to the fermion action, see section {4.2}. For the actual update the equations of motion (4.1.8) and (4.1.9) have to be integrated, giving a new configuration for the link variables and the conjugate momenta at a later time $(U,\pi) \to (U',\pi')$. After the evolution, one does an accept/reject-step with the acceptance probability [5]

$$P_{acc}(U',\pi'|U,\pi) = \min\left(1, \frac{\exp\left(-H\left[U',\pi'\right]\right)}{\exp\left(-H\left[U,\pi\right]\right)}\right)\ . \tag{4.1.11}$$

The clue is that an exact solution of the equations of motion leaves the Hamiltonian invariant, as it is a constant of motion. Thus, with an exact integration method, one would achieve an acceptance ratio of one and the new configurations would always be accepted. Unfortunately, there is in general no analytic solution to the equations of motion, therefore the integration is done numerically. The numerical

integration introduces errors, which lead to a change in the Hamiltonian $\Delta H \neq 0$ and the accept/reject-step can be seen as a corrective step. We require that the Hybrid Monte Carlo algorithm obeys the so-called *detailed balance condition*, which ensures that there are no sinks and sources of probability, leading to a fixed point at the desired equilibrium distribution $p_{eq.}(U) \propto e^{-S_G[U]}$ (see [5]). It can be shown that to achieve this we only need to Gaussian distribute the real parameters of the conjugate momenta $p^j_\mu(n)$ and require our integration method to fulfill the following two properties [5]:

- Area preservation of the integration measure $\mathcal{D}[U]\mathcal{D}[\pi]$
  $\Rightarrow$ corresponding to Liouville's theorem
- Reversibility of the molecular dynamics trajectory $(U, \pi) \leftrightarrow (U', \pi')$
  $\Rightarrow$ corresponding to the detailed balance condition

A class of integrators obeying these properties are the so-called *symplectic integrators*, like the *leapfrog integrator* explained in appendix {A.7}. All symplectic integrators preserve a Hamiltonian, which is slightly disturbed from the original one, where the difference in the Hamiltonians depends only on the step size $\Delta\tau$ of the integration and not on the length of the trajectory. Hence, through tuning the step size $\Delta\tau$ one can achieve a high acceptance ratio. For the leap frog integrator holds $\Delta H \sim O(\Delta\tau^2)$. With a suiting integrator, a Hybrid Monte Carlo step can be done according to the following steps:

1. Generate the real parameters for the conjugate momenta according to the Gaussian distribution $p(x) \propto \exp(-\frac{x^2}{2})$
2. Evolve along a molecular dynamics trajectory $(U, \pi) \to (U', \pi')$
3. Do an accept/reject-step with acceptance probability $p_{acc.} = \min(1, \exp(-\Delta H))$

4.2. Including Staggered Fermions in the HMC

This section will show how to numerically calculate observables from the full QCD path integral

$$Z = \int \mathcal{D}[U] \ \det(D[U]) \ e^{-S_G[U]} \ , \tag{4.2.1}$$

with staggered fermions, using the Hybrid Monte Carlo algorithm from the previous section. Notice that there is no possibility to employ a local updating algorithm, when including dynamical fermions, because of the high non-locality of the fermion determinant. The Dirac operator for staggered fermions can be read off from the staggered action (3.1.3) to be

$$D[U](n|m) = \sum_{\mu=1}^{4} \eta_\mu(n) \frac{U_\mu(n)\delta_{m,n+\hat{\mu}} - U_{-\mu}(n)\delta_{m,n-\hat{\mu}}}{2a} + m \ \delta_{mn} \ . \tag{4.2.2}$$

The basic idea for the inclusion of dynamical fermions into the HMC is to include the fermion determinant into the probability weight for the gauge configurations during the Markov chain, so that the gauge fields are generated according to the new equilibrium probability distribution of

$$p_{eq.}(U) \propto e^{-S_G[U]} \det(D[U]) \ . \tag{4.2.3}$$

In order to be interpreted as a probability weight factor, the fermion determinant has to be real and non-negative. The reality of the fermion determinant can easily be shown for Dirac operators who obey the property of γ_5-hermiticity $\gamma_5 D \gamma_5 = D^\dagger$, which holds for the staggered Dirac operator [5] and hence for the fermion determinant we have

$$\det(D)^* = \det(D^\dagger) = \det(\gamma_5 D \gamma_5) = \det(D) \ . \tag{4.2.4}$$

To ensure that the probability weight is positive, we just square the Dirac operator $D \to DD^\dagger$, so that for the fermion determinant factor we achieve

$$0 \leqslant \det(D) \det(D^\dagger) = \det(DD^\dagger) \ , \tag{4.2.5}$$

meaning physically that the number of quark flavors described by the theory has been doubled. We have shown in the section {3.2} that the staggered action describes $N_f = 4$ different quark flavors, hence calculations with the squared Dirac operator accord to a theory with $N_f = 8$ quark flavors. A Method to reduce the number of quark flavors N_f will be shown in the following section. In section {4.1} we already mentioned that additional terms in the action of the theory introduce additional force terms in the equation of motion for the conjugate momenta and leave the principle of the algorithm untouched. Thus, we want to reintroduce the fermion determinant as a part of the action. This can be done without the pain of reintroducing Grassman valued numbers for the fermions again by introducing so-called *pseudofermions* instead [5][11]. The pseudofermions are bosons having the same number of degrees of freedom as the original fermions. Exploiting the relation

$$\det[M] = \frac{1}{\det[M^{-1}]} \tag{4.2.6}$$

and introducing N complex variables $\phi = \phi_R + i\phi_I$ we can rewrite the fermion determinant of the squared Dirac operator as [5]

$$\det(DD^\dagger) = \frac{1}{\pi^N} \int \prod_{i=1}^{N} d\phi_{R,i} d\phi_{I,i} \ \exp\left(-\sum_{i,j} \phi_i^\dagger \left(DD^\dagger\right)^{-1}_{ij} \phi_j \right) \ . \tag{4.2.7}$$

Therefore, the full QCD path integral is also given by

$$Z = \frac{1}{\pi^N} \int \mathcal{D}[U]\mathcal{D}[\phi^\dagger]\mathcal{D}[\phi] \; e^{-S_G[U]-S_F[\phi,\phi^\dagger,U]} \tag{4.2.8}$$

$$\text{with} \quad S_F[\phi,\phi^\dagger,U] = \phi^\dagger \left((DD^\dagger)[U]\right)^{-1} \phi \; . \tag{4.2.9}$$

Hence, the molecular dynamics Hamiltonian (4.1.3) changes to

$$H[\pi,U] = \sum_{n\in\Lambda}\sum_{\mu} \mathrm{tr}\left[\pi_\mu(n)^2\right] + S_G[U] + S_F[\phi,\phi^\dagger,U] \; , \tag{4.2.10}$$

leading to the additional force term from the fermions

$$F_{F,\mu}(n)_{fg}\Big|_{TA} = U_\mu(n)_{fb}\frac{\partial S_F}{\partial U_\mu(n)_{gb}}\Big|_{TA} \; , \tag{4.2.11}$$

which is calculated in appendix {A.6}. The equilibrium probability weight factor for a configuration of pseudofermions ϕ and link variables U is now given by the total action

$$p_{eq.} \propto \exp\left(S_G[U] + S_F[\phi,\phi^\dagger,U]\right) \tag{4.2.12}$$

and we have to update the pseudofermions and the link variables for a HMC step. The update of the pseudofermions is easily done, because during the molecular dynamics evolution the pseudofermion fields can be treated as constant background fields. Thus, one starts the HMC algorithm by generating a new pseudofermion field configuration ϕ, distributed according to the weight factor $\propto \exp\left(-\phi^\dagger \left(\left(DD^\dagger\right)[U]\right)^{-1}\phi\right)$, which is done by the following two steps [5]:

1. Generate complex vectors η according to the Gaussian distribution

$$p(\eta) \propto \exp\left(-\eta^\dagger\eta\right) \tag{4.2.13}$$

2. Determine the pseudofermion fields as $\phi = D\eta$ and $\phi^\dagger = \eta^\dagger D^\dagger$

After the pseudofermion fields are constructed, we update the link variables with a molecular dynamics trajectory as described in section {4.1}, with the addition of the fermion action contributing to the Hamiltonian and the fermion force contributing to the equation of motion for the conjugate momenta.

4.3. The Rational HMC - Reducing the Number of Quark Flavors

In general, the number of quark flavors described by the theory depends on the exponent of the fermion determinant and also on the Dirac operator. Hence, naively

we can include roots of the fermion determinant of the squared Dirac operator into the HMC to adjust the number of simulated quark flavors. The rational HMC follows from the HMC algorithm by approximating the fermion determinant as

$$\det\left(DD^\dagger\right)^\alpha \approx \frac{1}{\pi^N}\int \mathcal{D}\phi^\dagger\mathcal{D}\phi\; e^{\phi^\dagger r_\alpha(DD^\dagger)\phi}\;, \quad |\alpha|<1\;, \tag{4.3.1}$$

with $r_\alpha(DD^\dagger) \approx (DD^\dagger)^{-\alpha}$ being the rational minimax approximation defined by [22]

$$\| r - f \|_\infty = \min_r \max_{x\in I} w(x)\,|r(x)-f(x)|\;, \tag{4.3.2}$$

where I is the interval containing the spectrum of $DD^\dagger$ and $w(x)$ is a positive weight function commonly chosen to be $w(x) \equiv \frac{1}{|f(x)|}$. Note that for hermitian matrices, like $A = DD^\dagger$, matrix valued functions are defined by [22]

$$f(A) \equiv Uf(M)U^\dagger \quad \text{with} \quad f(M)_{ii} = f(M_{ii})\;, \tag{4.3.3}$$

as hermitian matrices can be transformed into a real diagonal matrix M through a unitary transformation $A = UMU^\dagger$. Hence, the rational approximation can be obtained without explicitly diagonalizing the matrix A. Writing the rational approximation r_α in partial fraction form

$$r_\alpha(DD^\dagger) = a_0^\alpha + \sum_{j=1}^n \frac{a_j^\alpha}{DD^\dagger + b_j^\alpha}\;, \tag{4.3.4}$$

where the coefficients a_j^α and b_j^α can be obtained through the so-called *Remez algorithm* [22], the resulting force term from the pseudofermions is readily calculated to be

$$\begin{aligned} F_\mu &= U_\mu\phi^\dagger\frac{\partial r_\alpha(DD^\dagger)}{\partial U_\mu}\phi \\ &= \sum_{j=1}^n a_j^\alpha U_\mu\phi^\dagger\frac{\partial(DD^\dagger+b_j^\alpha)^{-1}}{\partial U_\mu}\phi \\ &= \sum_{j=1}^n a_j^\alpha U_\mu\phi^\dagger(DD^\dagger+b_j^\alpha)^{-1}\left(\frac{\partial D}{\partial U_\mu}D^\dagger + D\frac{\partial D^\dagger}{\partial U_\mu}\right)(DD^\dagger+b_j^\alpha)^{-1}\phi\;. \end{aligned} \tag{4.3.5}$$

In analogy to the HMC algorithm we identify $\chi_j = (DD^\dagger + b_j^\alpha)^{-1}\phi$ and thus for every integer value of j we need to solve the system

$$\left(DD^\dagger + b_j^\alpha\right)\chi_j = \phi\;, \tag{4.3.6}$$

making it clear that the rational HMC is computationally more expensive. To solve for all the χ_j a so-called *multishift-inverter* is used [23]. As in the HMC algorithm,

we wish to sample the pseudofermions from Gaussian distributed complex vectors η. Thus we split up the pseudofermion action into a symmetric product, from which it results that the pseudofermions follow the probability distribution given by

$$p(\phi) \propto e^{-\phi^\dagger r_{\frac{\alpha}{2}}(DD^\dagger) r_{\frac{\alpha}{2}}(DD^\dagger)\phi} \ . \tag{4.3.7}$$

Hence, we solve

$$\phi = r_{\frac{\alpha}{2}}^{-1}(DD^\dagger)\ \eta = r_{-\frac{\alpha}{2}}(DD^\dagger)\ \eta \tag{4.3.8}$$

by using the partial fraction form of the rational approximation $r_{-\frac{\alpha}{2}}$ to obtain the pseudofermions. Lastly, we need the Hamiltonian contribution of the pseudofermion action for the accept/reject-step of the HMC algorithm. It is calculated according to

$$S_F[\phi, \phi^\dagger] = \vartheta^\dagger \vartheta \ , \quad \text{with} \quad \vartheta = r_{\frac{\alpha}{2}}(DD^\dagger)\phi \ . \tag{4.3.9}$$

Thus for the sampling of the pseudofermions, the force calculation and the Hamiltonian contribution we use the multishift-inverter with different rational approximations, always employing the partial fraction form (4.3.4). This is summed up in table (4.1).

Pseudofermion sampling	Force calculation	Hamiltonian contribution
$r_{-\frac{\alpha}{2}}(DD^\dagger)$	$r_\alpha(DD^\dagger)$	$r_{\frac{\alpha}{2}}(DD^\dagger)$

Table 4.1.: The needed rational approximations for the rational HMC.

The factor by which the number of quark flavors is reduced depends on the value of the exponent α of the fermion determinant in equation (4.3.1). Some possibilities are given by

$$\begin{aligned} \alpha = \tfrac{1}{2} \quad &\Rightarrow \quad N_f = 8 \to N_f = 4 \\ &\quad\ \ or \quad N_f = 4 \to N_f = 2 \ , \\ \alpha = \tfrac{1}{4} \quad &\Rightarrow \quad N_f = 8 \to N_f = 2 \ . \end{aligned} \tag{4.3.10}$$

5. Lattice QCD at non-vanishing Temperature and Chemical Potential

In this section, the two physical parameters who span the phase diagram of QCD will be introduced on the lattice. These are the temperature and the quark chemical potential. Firstly, the connection of the temperature to the lattice spacing and the time extension of the lattice will be shown. Then, the inclusion of the quark chemical potential into the Dirac operator of staggered fermions is presented. Finally, we will observe the so-called *sign problem*, due to the non-vanishing quark chemical potential, and point out how we can avoid it by simulating two-color QCD instead of the physical three-color QCD.

5.1. Temperature on the Lattice

The partition function at non-vanishing temperature T for a Euclidean quantum field theory can generally be written as

$$Z(T) = \int \mathcal{D}[\Psi] \ \exp\left(-S_E[\Psi]\right) \ , \tag{5.1.1}$$

$$\text{with} \quad S_E[\Psi] = \int_0^{\frac{1}{T}} dt \int_{\mathbb{R}^3} d\vec{x} \ L_E\left(\Psi(t,\vec{x}), \partial_\mu \Psi(t,\vec{x})\right) \ . \tag{5.1.2}$$

To ensure the Pauli exclusion principle, the field Ψ is restricted to be either anti-periodic (fermions) or periodic (bosons) in time. Thus, a theory at finite temperature on the lattice is discretized as described in section {2} and the temperature is connected to the time extension of the lattice according to

$$\frac{1}{T} = aN_t \ . \tag{5.1.3}$$

5.2. Introducing a Chemical Potential μ

Now, the quark chemical potential μ, which allows the observation of non-vanishing quark number density on the lattice, will be included into the lattice theory. With a non-vanishing chemical potential in our theory, we do not calculate the partition function of a canonical ensemble any more, but of a grand canonical ensemble. In free continuum theory of Dirac fermions the conserved baryon current, according to the global U(1) symmetry, is given by *Noether's theorem* as

$$j_\mu(x) = \bar{\psi}(x)\gamma_\mu\psi(x) \tag{5.2.1}$$

and the particle number is given by the spatial integral over the temporal component

$$\hat{N} = \int d\vec{x}\ \bar{\psi}\gamma_4\psi\ . \tag{5.2.2}$$

Therefore, in free continuum theory one introduces the chemical potential with an additional term in the Lagrangian density

$$\mathcal{L} = \bar{\psi}D\psi = \bar{\psi}(\gamma_\mu\partial_\mu + \mu\gamma_4 + m)\psi\ . \tag{5.2.3}$$

Now, one could think of introducing the chemical potential in an analogue way on the lattice by adding an additional term to the naive free fermion action (2.1.3) [24]

$$S[\bar{\psi},\psi](\mu) = a^4 \sum_{n\in\lambda} \bar{\psi}(n)\ \mu\gamma_4\ \psi(n)\ , \tag{5.2.4}$$

but this leads to problems if one calculates the free energy density and takes the naive continuum limit $a \to 0$ [5]

$$\lim_{a\to 0} (\epsilon(\mu) - \epsilon(0)) \propto (\frac{\mu}{a})^2\ . \tag{5.2.5}$$

Hence, the free energy density diverges in the continuum limit for this naive approach. Looking at the interacting theory, we can find another way to introduce the chemical potential. The Lagrangian density now includes the covariant derivative $D_\mu = \partial_\mu + iA_\mu$, notice that

$$\begin{aligned}
\mathcal{L} &= \bar{\psi}(\gamma_\mu D_\mu + \mu\gamma_4 + m)\psi \\
&= \bar{\psi}(\gamma_i(\partial_i + iA_i) + \gamma_4(\partial_4 + iA_4 + \mu) + m)\psi \\
&= \bar{\psi}(\gamma_i(\partial_i + iA_i) + \gamma_4(\partial_4 + iA_4 + i\tilde{A}_4) + m)\psi \\
&= \bar{\psi}(\gamma_\mu\tilde{D}_\mu + m)\psi\ ,
\end{aligned} \tag{5.2.6}$$

where we have identified a new external temporal gauge field $\tilde{A}_4 = -i\mu$ and absorbed it into the new covariant derivative $\tilde{D}_\mu$. In section {2.3} we showed how to connect a gauge field to link variables on the lattice and hence we introduce a chemical potential by including additional link variables corresponding to the external gauge field $\tilde{A}_4$ in temporal direction

$$U_{4,\text{ext}} = e^{ia\tilde{A}_4} = e^{a\mu}\ . \tag{5.2.7}$$

Finally, we arrive at the staggered Dirac operator for non-vanishing chemical potential μ, which is given by

$$D[U,\mu](n|m) = \sum_{\mu=1}^{4} \eta_\mu(n) \frac{U_\mu(n)\ e^{a\mu\delta_{\mu,4}}\ \delta_{m,n+\hat{\mu}} - U_{-\mu}(n)\ e^{-a\mu\delta_{\mu,4}}\ \delta_{m,n-\hat{\mu}}}{2a} + m\ \delta_{mn}\ . \tag{5.2.8}$$

This form of the Dirac operator shows that a non-vanishing chemical potential introduces a matter-antimatter asymmetry as the propagation of a quark in positive time direction is favored by a factor of $e^{a\mu}$ and the propagation of a quark in negative time, this corresponds to an anti-quark, is disfavored by a factor of $e^{-a\mu}$. The quark number density results from the difference between the number of quarks and anti-quarks and thus will be unequal to zero for a non-vanishing quark chemical potential. Now, the fermion force term (A.6.8) for the HMC algorithm is given by

$$\begin{aligned} F_{F,\mu}(n,\mu)\Big|_{TA} =& \frac{\eta_\mu(n)}{2a} \Big[U_\mu(n) \Big((D^\dagger\chi)(n+\hat{\mu})\chi^\dagger(n) e^{a\mu\delta_{\mu,4}} - \chi(n+\hat{\mu})(D^\dagger\chi)^\dagger(n) e^{-a\mu\delta_{\mu,4}} \Big) \\ &+ \Big((D^\dagger\chi)(n)\chi^\dagger(n+\hat{\mu}) e^{-a\mu\delta_{\mu,4}} - \chi(n)(D^\dagger\chi)^\dagger(n+\hat{\mu}) e^{a\mu\delta_{\mu,4}} \Big) U_\mu^\dagger(n) \Big] \Big|_{TA} . \end{aligned} \tag{5.2.9}$$

Notice that a chemical potential can be introduced when using Wilson fermions in the same manner [25]. Unfortunately, lattice QCD for non-vanishing quark chemical potential suffers under the so-called *sign problem*, which shall be explained in the next section.

5.3. The Sign Problem

Introducing a quark chemical potential on the lattice is conceptionally easy, as seen in the last section, but the sign problem arises. In section {4.2} we have seen that the γ_5-hermiticity of the Dirac operator is needed to have a real fermion determinant and hence to be able to use it as a probability weight. Checking γ_5-hermiticity for the continuum Dirac operator including a chemical potential, we achieve

$$\gamma_5(\not{D} + m + \gamma_4\mu)\gamma_5 = -\not{D} + m - \gamma_4\mu = (\not{D} + m - \gamma_4\mu)^\dagger \tag{5.3.1}$$

$$\implies \quad \gamma_5 D(\mu)\gamma_5 = D(-\mu)^\dagger \quad \iff \quad \det(D) \in \mathbb{C}\ . \tag{5.3.2}$$

It is not possible to include a complex fermion determinant into the probability weight for the generation of the gauge field configurations with the HMC algorithm. Hence, different methods have to be employed. Due to the sign problem, we use SU(2) as the gauge group, corresponding to $N_c = 2$ colors. The reason for this is the pseudo-reality of the fundamental representation of SU(2) [4]

$$T_a \in \mathrm{SU}(2) \quad \implies \quad (\tau_2)\ T_a\ (\tau_2)^{-1} = -(T_a)^*\ , \tag{5.3.3}$$

where τ_2 is a Pauli matrix. Using this property, it is shown in appendix {A.8} that the fermion determinant in two-color QCD is real even for non-vanishing chemical potential and the fermion determinant can be included into the HMC algorithm through pseudofermions as described in {4.2}.

6. Diquarks in two-color Lattice QCD

In this section, we will include an explicit diquark source term into the staggered fermion action with $SU(2)$ link variables to be able to observe a superfluid phase, indicated by a non-vanishing diquark condensate, which causes a spontaneous symmetry breaking of quark number conservation. We will demonstrate for the resulting modified action how the diquark condensate, the chiral condensate and the quark number density can be measured on the lattice. Furthermore, we will show how we can reduce the number of quark flavors by using the rational HMC while having a diquark source term in the action.

6.1. The Staggered Action with a Diquark Source Term

Here, we will include a diquark source term into the fermionic part of the action. The action including diquarks is given by [7][8]

$$S_F[\chi, \bar{\chi}] = \bar{\chi}\ D[\mu]\ \chi + \frac{\lambda}{2}\left(\chi^T \tau_2 \chi + \bar{\chi}\tau_2\bar{\chi}^T\right)\ , \tag{6.1.1}$$

where $D[\mu]$ is the staggered Dirac operator with non-vanishing chemical potential μ given by (5.2.8) and τ_2 is a Pauli matrix, acting on the color indices of the fermion fields. To achieve physical results, we will extrapolate measurements to $\lambda = 0$. This action can be rewritten to

$$S_F = \frac{1}{2}\begin{pmatrix} \bar{\chi} & \chi^T \end{pmatrix}\begin{pmatrix} \lambda\tau_2 & D[\mu] \\ -D[\mu]^T & \lambda\tau_2 \end{pmatrix}\begin{pmatrix} \bar{\chi}^T \\ \chi \end{pmatrix}\ . \tag{6.1.2}$$

Introducing a new field $\phi^T = \begin{pmatrix}\bar{\chi} & \chi^T\end{pmatrix}$, the fermion action is simplified to $S_F = \frac{1}{2}\phi^T A\phi$ with A being the matrix in equation (6.1.2). It is important to notice that A is anti-symmetric and is sandwiched between ϕ and ϕ^T, no complex conjugation of the field ϕ is needed and thus the Grassmann integration over the fermionic degrees of freedom can be done with real Grassmann numbers, instead of complex ones, leading to the *pfaffian* of the matrix A

$$\begin{aligned} Z_F &= \int \mathcal{D}\chi\mathcal{D}\bar{\chi}\ e^{-S_F[\chi,\bar{\chi}]} = \int \mathcal{D}\phi\ e^{-\frac{1}{2}\phi^T A\phi} \\ &= \mathrm{pfaff}(A) = \sqrt{\det(A)}\ . \end{aligned} \tag{6.1.3}$$

Using the general formula of the determinant for matrices with blocks of 2×2 sub-matrices

$$\det \begin{pmatrix} X & Y \\ W & Z \end{pmatrix} = \det(X)\, \det(Z - WX^{-1}Y) \ , \tag{6.1.4}$$

we can calculate the determinant of the matrix A to be

$$\begin{aligned} \det(A) &= \det(\lambda\tau_2)\, \det\left(\lambda\tau_2 + D[\mu]^T \frac{1}{\lambda}\tau_2 D[\mu]\right) \\ &= \det\left(\lambda^2 + \tau_2 D[\mu]^T \tau_2 D[\mu]\right) \\ &= \det\left(\lambda^2 + D[\mu]^\dagger D[\mu]\right) \ , \end{aligned} \tag{6.1.5}$$

where we have used the pseudo-reality of SU(2)

$$\tau_2 U_\mu \tau_2 = U_\mu^* \quad \Longrightarrow \quad \tau_2 D[\mu]^T \tau_2 = D[\mu]^\dagger \ . \tag{6.1.6}$$

Hence, the fermionic partition function reads

$$Z_F = \sqrt{\det\left(D[\mu]^\dagger D[\mu] + \lambda^2\right)} \tag{6.1.7}$$

and the square root reduces the number of quark flavors described by the considered theory back to $N_f = 4$. As the pfaffian of a matrix is strictly real and positive, it can be included as a probability weight for the gauge configurations into the HMC algorithm. For this, we again use pseudofermions as described in section {4.2}. Unfortunately, a straightforward replacement of $\phi^\dagger(DD^\dagger)^{-1}\phi$ by $\phi^\dagger(DD^\dagger + \lambda^2)^{-1}\phi$ causes problems in the sampling of the random pseudofermions. The matrix $(DD^\dagger + \lambda^2)^{-1}$ can not be split up in a product like $(XX^\dagger)^{-1}$ and thus we could not sample Gaussian distributed complex vectors η and calculate our pseudofermions from them by a simple matrix product $\phi = X\eta$. Therefore, we consider the matrix $\tilde{A}$ given by

$$\begin{aligned} &\tilde{A} = \begin{pmatrix} \lambda & D[\mu] \\ -D[\mu]^\dagger & \lambda \end{pmatrix} = \begin{pmatrix} 1 & 0 \\ 0 & \tau_2 \end{pmatrix} A \begin{pmatrix} \tau_2 & 0 \\ 0 & 1 \end{pmatrix} \ , \\ &\text{with} \ \ \det(\tilde{A}) = \det(A) = \det\left(D[\mu]^\dagger D[\mu] + \lambda^2\right) \ . \end{aligned} \tag{6.1.8}$$

The matrices A and $\tilde{A}$ have the same determinant and therefore we can use $\tilde{A}$ in the HMC algorithm. To apply the HMC algorithm, we multiply $\tilde{A}$ by its conjugate transpose

$$\tilde{A}^\dagger \tilde{A} = \tilde{A}\tilde{A}^\dagger = \begin{pmatrix} D[\mu]D[\mu]^\dagger + \lambda^2 & 0 \\ 0 & D[\mu]^\dagger D[\mu] + \lambda^2 \end{pmatrix} \ . \tag{6.1.9}$$

Note that for the determinants we find the following properties

$$\det(\tilde{A}\tilde{A}^\dagger) = \det(A)^2 = \det\left(D[\mu]^\dagger D[\mu] + \lambda^2\right)^2 \ , \tag{6.1.10}$$

$$\det\left(D[\mu]^\dagger D[\mu] + \lambda^2\right) = \det\left(D[\mu]D[\mu]^\dagger + \lambda^2\right) \ . \tag{6.1.11}$$

A direct use of the HMC algorithm with the matrix $\tilde{A}\tilde{A}^\dagger$ will lead to $\det(A)^2$ and not $\sqrt{\det(A)}$. This problem is overcome by realising that $\tilde{A}\tilde{A}^\dagger$ is block diagonal and therefore does not mix upper and lower components of the pseudofermions, which for now have twice the number of components as in the case of using $DD^\dagger$. Hence, after the sampling of the pseudofermions we drop the lower components and only use the upper components in the remaining steps of the HMC algorithm. Still, this only leads to $\det(A)$ and thus we need to reduce the number of degrees of freedom of the pseudofermions further to arrive at $\sqrt{\det(A)}$. [7] suggests that this can be done by rescaling the action of the pseudofermions by $\frac{1}{2}$. We will check if reducing the number of degrees of freedom of the pseudofermions by using real instead of complex ones has the same effect and if both methods lead to $\sqrt{\det(A)}$, according to a theory of $N_f = 4$ quark flavors. The sampling of the pseudofermions with a reduced number of degrees of freedom according to the probability distribution $\propto \exp(-\tilde{\phi}^\dagger(\tilde{A}\tilde{A}^\dagger)^{-1}\tilde{\phi})$ is done in two steps:

1. Generate real vectors η according to the Gaussian distribution $p(\eta) \propto \exp(-\eta^T\eta)$
2. Determine the pseudofermion fields as $\tilde{\phi} = \tilde{A}\eta$ and $\tilde{\phi}^\dagger = \eta^T\tilde{A}^\dagger$

Note that this will not guarantee real pseudofermions as the matrix $(\tilde{A}\tilde{A}^\dagger)^{-1}$ is in general complex, but using real vectors η, instead of complex ones, will already have the same effect and reduces the number of degrees of freedom of the pseudofermions by two. After step two, we drop the lower components of the pseudofermions to get

$$\tilde{\phi} = \begin{pmatrix} \phi \\ 0 \end{pmatrix} \tag{6.1.12}$$

and the fermion force for the molecular dynamics can now be calculated in the usual manner

$$\begin{aligned} F_{F,\mu}(n)_{ef} &= U_\mu(n)_{ec}\ \tilde{\phi}_a^\dagger \frac{\partial(\tilde{A}\tilde{A}^\dagger)^{-1}_{ab}}{\partial U_\mu(n)_{fc}}\ \tilde{\phi}_b \\ &= -U_\mu(n)_{ec}\ \phi_a^\dagger (DD^\dagger + \lambda^2)^{-1}_{ah} \left(\frac{\partial(DD^\dagger + \lambda^2)_{ab}}{\partial U_\mu(n)_{fc}} \right) (DD^\dagger + \lambda^2)^{-1}_{nb} \phi_b \\ &= -U_\mu(n)_{ec}\ \chi_h^\dagger \left(\frac{\partial D_{hm}}{\partial U_\mu(n)_{fc}} D^\dagger_{mn} + D_{hm} \frac{\partial D^\dagger_{mn}}{\partial U_\mu(n)_{fc}} \right) \chi_n\ , \end{aligned} \tag{6.1.13}$$

where we have identified $\chi = (DD^\dagger + \lambda^2)^{-1}\phi$ and thus now we need inversions of $DD^\dagger + \lambda^2$ for the HMC algorithm.

6.2. The Chiral and Diquark Condensate

Now, we will show how the calculation for the chiral condensate, already explained in section {3.3.2}, has to be adjusted, when including an explicit diquark source term into the staggered action. Furthermore, we will introduce the measurement of the diquark condensate. To recap, the fermionic part of the partition function from section {6.1} is given by

$$Z = \int \mathcal{D}\phi \; e^{-\frac{1}{2}\phi^T A \phi} = \sqrt{\det(\tilde{A})} \; , \tag{6.2.1}$$

$$\text{with} \;\; \tilde{A} = \begin{pmatrix} \lambda & D[\mu] \\ -D[\mu]^\dagger & \lambda \end{pmatrix} \; . \tag{6.2.2}$$

In section {3.3.2} we calculated the chiral condensate with the help of the generating functional (2.5.15). Here, we have to deal with the matrix $\tilde{A}$ and thus it is more convenient to directly calculate the two condensates from the fermionic part of the partition function. Noticing that the chiral condensate behaves like a mass term, we can state that

$$\langle \bar{\psi}\psi \rangle = \lim_{\lambda \to 0} \frac{1}{V} \frac{\partial \ln Z}{\partial m} \; . \tag{6.2.3}$$

The diquark condensate can be calculated in complete analogy like [26][27]

$$\langle \psi\psi \rangle = \lim_{\lambda \to 0} \frac{1}{V} \frac{\partial \ln Z}{\partial \lambda} \; . \tag{6.2.4}$$

Using the well know relation for matrices

$$\ln \det X = \operatorname{tr} \ln X \; , \tag{6.2.5}$$

we obtain

$$\langle \bar{\psi}\psi \rangle = \lim_{\lambda \to 0} \frac{c}{V} \operatorname{tr} \left(\tilde{A}^{-1} \begin{pmatrix} 0 & 1 \\ -1 & 0 \end{pmatrix} \right) \; , \tag{6.2.6}$$

$$\langle \psi\psi \rangle = \lim_{\lambda \to 0} \frac{c}{V} \operatorname{tr} \left(\tilde{A}^{-1} \begin{pmatrix} 1 & 0 \\ 0 & 1 \end{pmatrix} \right) \; . \tag{6.2.7}$$

The normalization constant c will be discussed at the end of this section. Still, we will use noisy estimators to calculate the traces, which now have twice the number of components and here it will not be possible to throw away the lower components, as we will see shortly. We estimate

$$\operatorname{tr} \left(\tilde{A}^{-1} M \right) \approx \frac{1}{N_F} \sum_{k=1}^{N_F} \bar{\psi}_k \; \tilde{A}^\dagger (\tilde{A}\tilde{A}^\dagger)^{-1} M \; \psi_k \; , \tag{6.2.8}$$

where M has to be chosen according to equation (6.2.6) or (6.2.7). Writing the upper and lower components of the noisy estimator fields explicitly

$$\psi = \begin{pmatrix} \psi_u \\ \psi_l \end{pmatrix} , \tag{6.2.9}$$

we can calculate each term of the sum in (6.2.8) for the chiral and the diquark condensate as

$$\begin{aligned} \bar{\psi}\ \tilde{A}^\dagger(\tilde{A}\tilde{A}^\dagger)^{-1} \begin{pmatrix} 0 & 1 \\ -1 & 0 \end{pmatrix} \psi \ &= \bar{\psi}_u \lambda \left(DD^\dagger + \lambda^2\right)^{-1} \psi_l + \bar{\psi}_u D \left(D^\dagger D + \lambda^2\right)^{-1} \psi_u \\ &+ \bar{\psi}_l D^\dagger \left(DD^\dagger + \lambda^2\right)^{-1} \psi_l - \bar{\psi}_l \lambda \left(D^\dagger D + \lambda^2\right)^{-1} \psi_u \ , \end{aligned} \tag{6.2.10}$$

$$\begin{aligned} \bar{\psi}\ \tilde{A}^\dagger(\tilde{A}\tilde{A}^\dagger)^{-1} \begin{pmatrix} 1 & 0 \\ 0 & 1 \end{pmatrix} \psi \ &= \bar{\psi}_u \lambda \left(DD^\dagger + \lambda^2\right)^{-1} \psi_u - \bar{\psi}_u D \left(D^\dagger D + \lambda^2\right)^{-1} \psi_l \\ &+ \bar{\psi}_l D^\dagger \left(DD^\dagger + \lambda^2\right)^{-1} \psi_u + \bar{\psi}_l \lambda \left(D^\dagger D + \lambda^2\right)^{-1} \psi_l \ . \end{aligned} \tag{6.2.11}$$

We stress the explicit mixing between the upper and lower components and the dependence of the condensates on the parameter λ. Hence, for each term of the noisy estimator sum we need an inversion of $\left(DD^\dagger + \lambda^2\right)$ and $\left(D^\dagger D + \lambda^2\right)$. For this, we employ the relation

$$D^\dagger[\mu, m] D[\mu, m] = D[-\mu, -m] D^\dagger[-\mu, -m] \ . \tag{6.2.12}$$

The normalization constant c To determine the normalization constant of the condensates, we refer to the usual fourth-root approach in the staggered formalism to account for the four-fold degeneracy of one staggered fermion. The partition function for N_f continuum flavors, using the staggered formalism, is thus generally given by [11]

$$Z = \det\left(D\right)^{\frac{N_f}{4}} \ , \tag{6.2.13}$$

from which we obtain the following chiral condensate

$$\left\langle \bar{\psi}\psi \right\rangle' = \frac{1}{V} \frac{N_f}{4} \mathrm{tr}\left(D^{-1}\right) \ . \tag{6.2.14}$$

In the limit $\lambda \to 0$, the chiral condensate obtained from equation (6.2.6) should be equal to $\left\langle \bar{\psi}\psi \right\rangle'$. This will fix our normalization constant c. Taking the limit $\lambda \to 0$ gives

$$\langle\bar{\psi}\psi\rangle = \frac{c}{V}\left(\mathrm{tr}\left(D^{-1}\right) + \mathrm{tr}\left((D^{\dagger})^{-1}\right)\right) = \frac{2c}{V}\mathrm{tr}\left(D^{-1}\right) \ , \tag{6.2.15}$$

where we used that the chiral condensate is a real quantity. Hence, by comparison we find the normalization constant to be

$$c = \frac{1}{2}\frac{N_f}{4} \ . \tag{6.2.16}$$

6.3. The Quark Number Density

Let us now introduce the measurement of the quark number density. We have found that the explicit diquark source does not seem to affect the results of the quark number density. Hence, we assume the $\lambda \to 0$ limit and derive the quark number density from the partition function (6.2.13). It will have an implicit dependence on the diquark source through the used gauge configurations only. The quark number couples to the chemical potential and thus the quark number density is obtained by taking the derivative of the partition function with respect to the chemical potential

$$\langle n\rangle = \frac{1}{V}\frac{\partial \ln Z}{\partial\mu} \ . \tag{6.3.1}$$

Using equation (6.2.5), we already arrive at our final result

$$\langle n\rangle = \frac{1}{V}\frac{N_f}{4}\mathrm{tr}\left(D^{-1}\frac{\partial D}{\partial\mu}\right) \ , \tag{6.3.2}$$

where the derivative of the staggered Dirac operator is given by

$$\frac{\partial D[\mu]_{nm}}{\partial\mu} = \frac{\eta_4(n)}{2a}\left(U_4(n)e^{a\mu}\delta_{m,n+\hat{4}} + U_{-4}(n)e^{-a\mu}\delta_{m,n-\hat{4}}\right) \tag{6.3.3}$$

and the trace is, again, approximated with noisy estimators.

6.4. The Rational HMC with a Diquark Source Term

We will find in section {10.1}, that the number of quark flavors can not be reduced by the methods explained in section {6.1}. Thus, we will use the rational HMC shown in section {4.3} for a quark flavor reduction. Note that now we do not need to deal with the matrix $\tilde{A}\tilde{A}^{\dagger}$ any more, as in section {6.1}. We are able to directly use

$$Z_F = \det\left(D[\mu]^{\dagger}D[\mu] + \lambda^2\right)^{\alpha} \tag{6.4.1}$$

and hence to include the diquark source into the rational HMC we only need to apply the replacement

$$DD^\dagger \to D[\mu]^\dagger D[\mu] + \lambda^2 \tag{6.4.2}$$

everywhere in section {4.3}. It follows that one can absorb the diquark source into the coefficients of the partial fraction form of the rational approximations

$$b_j^\alpha \to b_j^\alpha + \lambda^2 \ . \tag{6.4.3}$$

Hence, we are able to simulate a theory of $N_f = 2$ or $N_f = 4$ flavors of staggered quarks, according to $\alpha = \frac{1}{4}$ or $\alpha = \frac{1}{2}$ respectively, while including a diquark source term.

7. The Pattern of Symmetry Breaking on the Lattice

To obtain some expectations of the phase diagram of two-color lattice QCD in the staggered formalism, we will now inspect the pattern of symmetry breaking and also identify the induced Goldstone modes, whose masses we want to measure later. As a start, we consider a theory of $N_f = 1$ staggered fermion (corresponding to four continuum flavors, see section {3.2}) and later discuss the more general case of $N_f > 1$ staggered fermions. The cases of vanishing chemical potential and of non-vanishing chemical potential will be considered. Note that using the rational HMC from section {4.3} to reduce the number of continuum flavors, does not affect the symmetries of the original action and the remaining continuum flavors inherit the symmetries of the unrooted action.

7.1. $N_f = 1$ Staggered Fermion

We will investigate the pattern of symmetry breaking induced by the diquark condensate and the chiral condensate. For this, we introduce a new basis for the fermion fields, which separates the even and odd sites, given by [28]

$$\bar{X}_e = \begin{pmatrix} \bar{\chi}_e & -\chi_e^T \tau_2 \end{pmatrix} \ , \quad X_o = \begin{pmatrix} \chi_o \\ -\tau_2 \bar{\chi}_o^T \end{pmatrix} \ . \tag{7.1.1}$$

Using the pseudo-reality of the generators of the fundamental representation of SU(2) (see equation (5.3.3)) and the Grassmann nature of the fermion fields, the kinetic part of the staggered action can be rewritten to

$$\begin{aligned} S_{kin} = \sum_{n \in \Lambda', \nu} \frac{\eta_\nu(n)}{2} \Bigg[& \bar{X}_e(n) \begin{pmatrix} e^{\mu\delta_{\nu,4}} & 0 \\ 0 & e^{-\mu\delta_{\nu,4}} \end{pmatrix} U_\nu(n) X_o(n+\hat{\nu}) \\ & - \bar{X}_e(n) \begin{pmatrix} e^{-\mu\delta_{\nu,4}} & 0 \\ 0 & e^{\mu\delta_{\nu,4}} \end{pmatrix} U_\nu(n-\hat{\nu})^\dagger X_o(n-\hat{\nu}) \Bigg] \ , \end{aligned} \tag{7.1.2}$$

where the sum is running over the even sides only. From this form of the action it is easy to check, that in the massless and zero density limit the fermion action is invariant under the following rotations

$$X_o \to V X_o \ \ , \ \bar{X}_e \to \bar{X}_e V^\dagger \ \ ; \ V \in U(2) \ . \tag{7.1.3}$$

Hence, in this special case the original $U(1)_V \otimes U(1)_A$ symmetry is enlarged to a $U(2)$ symmetry. This is specific for the lattice formulation, as the axial anomaly would reduce the symmetry to $SU(2)$ in the continuum formulation. Rewriting the mass term and the diquark source term in the basis given by (7.1.1), we obtain [28]

$$\bar{\chi}\chi = \frac{1}{2}\left[\bar{X}_e \begin{pmatrix} 0 & 1 \\ 1 & 0 \end{pmatrix} \tau_2 \bar{X}_e^T + X_o^T \begin{pmatrix} 0 & 1 \\ 1 & 0 \end{pmatrix} \tau_2 X_o\right] , \tag{7.1.4}$$

$$qq_2 = \frac{1}{2}\left[\bar{X}_e \begin{pmatrix} 1 & 0 \\ 0 & -1 \end{pmatrix} \tau_2 \bar{X}_e^T + X_o^T \begin{pmatrix} 1 & 0 \\ 0 & -1 \end{pmatrix} \tau_2 X_o\right] . \tag{7.1.5}$$

The condensates are connected by an explicit $U(2)$ rotation

$$V = \frac{i}{\sqrt{2}} \begin{pmatrix} 1 & 1 \\ -1 & 1 \end{pmatrix} \tag{7.1.6}$$

and hence they are physically indistinguishable in the zero density limit. Which condensate forms in the lattice simulation depends on the choice of the explicit symmetry breaking term. If we include a mass term and no diquark source term we will measure a chiral condensate but no diquark condensate and vice versa. Thus, for vanishing chemical potential we can define a combined condensate $\sqrt{\langle\bar{\psi}\psi\rangle^2 + \langle\psi\psi\rangle^2}$ and every set of parameters (m, λ) laying on the same quarter circle defined by $\sqrt{m^2 + \lambda^2} = const$ will lead to the same combined condensate. This makes it clear that both condensates induce the same pattern of symmetry breaking in the zero density limit. To obtain insight in the differences between vanishing and non-vanishing chemical potential, we will investigate the Goldstone modes. To derive the Goldstone modes, we apply the infinitesimal $U(2)$ rotations

$$V_\delta = \mathbb{I} + i\delta\lambda \quad , \quad \lambda \in \{\mathbb{I}, \tau_i\} \tag{7.1.7}$$

on the chiral condensate (7.1.4) and the diquark condensate (7.1.5). The coefficient of $O(\delta)$ can then be identified as the Goldstone mode [28]. We obtain:

λ	$\langle\bar{\psi}\psi\rangle$	$\langle\psi\psi\rangle$
$\mathbb{I}$	$\bar{\chi}\epsilon\chi$	$\chi^T\tau_2\epsilon\chi + \bar{\chi}\tau_2\epsilon\bar{\chi}^T$
τ_1	$\chi^T\tau_2\chi - \bar{\chi}\tau_2\bar{\chi}^T$	$\mathbb{I}$
τ_2	$\chi^T\tau_2\chi + \bar{\chi}\tau_2\bar{\chi}^T$	$\bar{\chi}\chi$
τ_3	$\mathbb{I}$	$\chi^T\tau_2\chi - \bar{\chi}\tau_2\bar{\chi}^T$

Table 7.1.: The induced Goldstone modes by the chiral and the diquark condensate according to the generators of $U(2)$. The factor ϵ is given by $\epsilon(n) = \eta_5(n) = (-1)^{n_1+n_2+n_3+n_4}$.

Hence, both condensates induce the same pattern of symmetry breaking $U(2) \to U(1)$ in the zero density limit as they both leave one generator of $U(2)$ unbroken. In the case of a non-vanishing chemical potential, where the symmetry is reduced from $U(2)$ to $U(1)_V \otimes U(1)_A$, we are left with the generators $\{\mathbb{I}, \tau_3\}$ of $U(2)$, corresponding to axial charge and baryon number conservation, respectively. From the chiral condensate we now only obtain the pion, which is a pseudo Goldstone mode in the case of non-vanishing quark mass. We obtain a diquark and a pseudoscalar diquark, which again is a pseudo Goldstone mode in the case of non-vanishing quark mass, from the diquark condensate. Different numbers of Goldstone modes induced from the condensates is an indicator for a phase transition, happening at some critical value of the chemical potential μ_c. The expectation is now to find the usual non-vanishing chiral condensate in the low density regime which gradually rotates into a diquark condensate characterising the high density regime, as in this regime diquark condensation is favored due to the large Fermi surface at large chemical potentials. As there is no $U(2)$ symmetry of the action for non-vanishing chemical potential anymore, this rotation is expected to be non-trivial [28].

7.2. $N_f > 1$ Staggered Fermions

Let us generalize the pattern of symmetry breaking of the last section to the case of $N_f > 1$ staggered fermions. This will help us to identify a corresponding continuum theory, exhibiting the same pattern of symmetry breaking. We will apply chiral perturbation theory to this continuum theory, from which we will obtain the critical chemical potential μ_c of the phase transition mentioned in the previous section and also predictions for fermionic observables and the Goldstone modes. We have seen that in the $N_f = 1$ case the symmetry of the staggered action becomes enlarged at vanishing chemical potential $U(1) \times U(1) \to U(2)$. This is easily extended to the $N_f > 1$ case, where we have a $U(1) \times U(1)$ symmetry for each flavor and thus at zero density the enlarged symmetry becomes

$$U(N_f) \times U(N_f) \quad \to \quad U(2N_f) \ . \tag{7.2.1}$$

The combined condensate $\sqrt{\langle\bar{\psi}\psi\rangle^2 + \langle\psi\psi\rangle^2}$ is invariant under $O(2N_f)$ rotations, and thus the pattern of symmetry breaking is $U(2N_f) \to O(2N_f)$.

At non-vanishing chemical potential, the symmetry breaking of the condensates (or equivalently of the source terms) is different. For the chiral condensate we find the usual symmetry breaking from section {3.3}, with the exception of leaving $U(1)_A$ unbroken

$$U(N_f) \times U(N_f) \quad \to \quad U(N_f) \times U(1)_B \ . \tag{7.2.2}$$

The diquark condensate breaks the symmetry of baryon number conservation and is invariant under $O(N_f)$, as it is flavor symmetric [28], hence

$$U(N_f) \times U(N_f) \quad \rightarrow \quad O(N_f) \ . \tag{7.2.3}$$

Thus, we can sum up the pattern of symmetry breaking of N_f staggered fermions as

$$\begin{tikzcd}
U(2N_f) \arrow[r, "\sqrt{\langle\bar{\psi}\psi\rangle^2 + \langle\psi\psi\rangle^2}"] \arrow[d, "\mu \neq 0"] & O(2N_f) \\
U(N_f) \times U(N_f) \arrow[r, "\langle\bar{\psi}\psi\rangle"] \arrow[dr, "\langle\psi\psi\rangle"] & U(N_f) \times U(1)_B \arrow[d, "\langle\psi\psi\rangle"] \\
 & O(N_f)
\end{tikzcd}$$

The corresponding continuum theory exhibiting the same pattern of symmetry breaking, except for the additional breaking of $U(1)_A$ due to the axial anomaly, is any color QCD with quarks in the adjoint representation. See section {9} for the leading order chiral perturbation theory application. Note that continuum two-color QCD with quarks in the fundamental representation exhibits the pattern of symmetry breaking of $SU(N_f) \times SU(N_f) \rightarrow Sp(2N_f)$ in the zero density limit [29]. It is not clear, if the two-color lattice theory will change its pattern of symmetry breaking in the continuum limit to the corresponding continuum pattern or if it keeps its lattice pattern [28].

8. Spectroscopy at non-vanishing Chemical Potential

This section will introduce the interpolating operators which we use to extract the masses of (pseudo-)scalar meson modes and (pseudo-)scalar diquark modes. These modes correspond to the Goldstone modes which we derived in section {7.1}. It will be shown how the correlation functions can be expressed in terms of quark propagators using Wick's theorem, making them accessible to lattice simulations. The difference between lattice spectroscopy at vanishing and non-vanishing chemical potential will be stressed. Lastly, we explain the fitting functions used to extract masses of particle states from the correlation functions.

8.1. The Interpolating Operators

For the scalar meson mode and the pion mode, we consider the same interpolating operators as in [6], given by:

Channel	Operator	J^{PC}	States
1	$\bar{\chi}\chi$	0^{++}	f_0
		0^{-+}	π
2	$\eta_4\bar{\chi}\chi$	0^{+-}	-
		0^{-+}	π

Table 8.1.: The interpolating operators for the scalar meson mode and the pion mode.

Note that channel 1 contains the scalar meson which we wish to inspect, as well as an excited pion which is heavier than the groundstate pion in channel 2. The signals of the two states in channel 1 in the corresponding correlation function can be separated during the fitting procedure by making use of their opposite parity, see section {8.3}. Channel 2 has an exclusive signal from the groundstate pion.

For the (pseudo-)scalar diquark modes, we consider the same interpolating operators as in [1], given by:

Channel	Operator	States
3	$\frac{1}{2}\left(\chi^T\tau_2\chi - \bar{\chi}\tau_2\bar{\chi}^T\right)$	$qq/\bar{q}\bar{q}$
4	$\eta_5\frac{1}{2}\left(\chi^T\tau_2\chi + \bar{\chi}\tau_2\bar{\chi}^T\right)$	$\varepsilon qq/\varepsilon\bar{q}\bar{q}$

Table 8.2.: The interpolating operators for the (pseudo-)scalar diquark modes.

The diquark modes contain a contribution from their corresponding anti-diquark mode. As the propagation of particles is favored ($e^{a\mu}$) over the propagation of anti-particles ($e^{-a\mu}$) at non-vanishing chemical potential, the contributions of the anti-diquark states will be become less important with increasing chemical potential.

8.2. The Correlation Functions

Next, we calculate the correlation functions for the operators of the previous section. As we wish to extract the ground state masses of the particle states, we employ the zero-momentum projected correlations functions of the form

$$C(t) = \sum_{\vec{x}} \left\langle 0 \left| O(\vec{x},t)\bar{O}(\vec{0},0) \right| 0 \right\rangle \ , \tag{8.2.1}$$

where the zero-momentum projection corresponds to the spatial Fourier transformation[1] with $\vec{p} = 0$. The resulting correlation functions are derived in appendix {A.12}. Here, we only give the final results. Note that we only consider the connected contributions to the correlation functions.

- Channel 1 - Scalar Meson

$$C(t) = -\sum_{\vec{x}} \eta_5(\vec{x},t)\ \mathrm{tr}\left[G^\dagger[-\mu](\vec{x},t;0)G[\mu](\vec{x},t;0)\right] \tag{8.2.2}$$

- Channel 2 - Pion / Pseudoscalar Meson

$$C(t) = -(-1)^t \sum_{\vec{x}} \mathrm{tr}\left[G^\dagger[-\mu](\vec{x},t;0)G[\mu](\vec{x},t;0)\right] \tag{8.2.3}$$

- Channel 3 - Scalar Diquark

$$\begin{aligned} C(t) = \frac{1}{2}\sum_{\vec{x}} \big\{ &\mathrm{tr}\left[G^T[\mu](\vec{x},t;0)\tau_2 G[\mu](\vec{x},t;0)\tau_2\right] \\ &+\mathrm{tr}\left[G^\dagger[-\mu](\vec{x},t;0)\tau_2 (G^\dagger)^T[-\mu](\vec{x},t;0)\tau_2\right]\big\} \end{aligned} \tag{8.2.4}$$

[1] $f(\vec{p},t) = \sum_{\vec{x}} f(\vec{x},t)\ e^{i\vec{p}\vec{x}}$

- Channel 4 - Pseudoscalar Diquark

$$C(t) = \frac{1}{2}\sum_{\vec{x}} \eta_5(\vec{x},t)\left\{\mathrm{tr}\left[G^T[\mu](\vec{x},t;0)\tau_2 G[\mu](\vec{x},t;0)\tau_2\right]\right. \\ \left. +\mathrm{tr}\left[G^\dagger[-\mu](\vec{x},t;0)\tau_2 (G^\dagger)^T[-\mu](\vec{x},t;0)\tau_2\right]\right\} \tag{8.2.5}$$

For the derivation of the correlation functions, we used Wick's theorem

$$\langle 0|\chi_i(x)\bar{\chi}_j(y)|0\rangle = G_{ij}(x,y) \ , \tag{8.2.6}$$

where G is the quark propagator and i, j are color indices. Note that throughout this master thesis the abbreviation $G^\dagger = G^{\dagger_c}$ is used, where $\dagger_c$ corresponds to the conjugate transpose of the color-structure. Furthermore, to swap the spacetime argument of the quark propagators, so that we can calculate all point-to-all propagators with the same point source, the relation

$$G[\mu](0,x) = \eta_5(x)G^\dagger[-\mu](x,0)\eta_5(0) \tag{8.2.7}$$

is used [30]. Notice the sign flip of the chemical potential which is due to the property (A.9.3). We stress that at vanishing chemical potential only one quark propagator G has to be calculated, but at non-vanishing chemical potential we need to calculate $G[\mu]$ and $G[-\mu]$ separately. In two-color lattice QCD the propagators are given by SU(2) matrices at every spacetime point

$$G_{ij} = \begin{pmatrix} a & b \\ -b^* & a^* \end{pmatrix} \tag{8.2.8}$$

and are calculated by inverting the staggered Dirac operator on a point source $v_i(x) = (1,0)^T\delta_{x,x_0}$

$$D_{ij}[\mu](x,y)\ w_j(y) = v_i(x) \\ \Rightarrow \quad w(y) = (G_{11}[\mu](y,x_0), G_{21}[\mu](y,x_0))^T = (a,-b^*)^T[\mu](y,x_0) \ ,$$

$$D_{ij}[-\mu](x,y)\ w_j(y) = v_i(x) \\ \Rightarrow \quad w(y) = (G_{11}[-\mu](y,x_0), G_{21}[-\mu](y,x_0))^T = (\tilde{a},-\tilde{b}^*)^T[-\mu](y,x_0) \ .$$

Using this, we can simplify the traces in the correlation function, which then are explicitly given by

$$\mathrm{tr}\left[G[\mu]G^\dagger[-\mu]\right] = 2\left(\mathrm{Re}(a\tilde{a}^*) + \mathrm{Re}(b\tilde{b}^*)\right) \ , \\ \mathrm{tr}\left[G^T[\mu]\tau_2 G[\mu]\tau_2\right] = 2(a^2+b^2) \ , \\ \mathrm{tr}\left[G^\dagger[-\mu]\tau_2 (G^\dagger)^T[-\mu]\tau_2\right] = 2(\tilde{a}^2+\tilde{b}^2) \ .$$

To take care of the λ-dependence of the propagator, we just have to apply the usual replacement $D^\dagger D \to D^\dagger D + \lambda^2$ in the inversion of the staggered Dirac operator

$$G = D^{-1} = (D^\dagger D)^{-1} D^\dagger \to (D^\dagger D + \lambda^2)^{-1} D^\dagger \ , \tag{8.2.9}$$

which is explained in more detail in appendix {A.13}. At last, notice that at vanishing chemical potential we have $a = \tilde{a}$ and $b = \tilde{b}$, hence the contribution from diquarks is equal to the contributions from anti-diquarks, as expected. Furthermore, at vanishing chemical potential it is easy to see that the scalar meson is degenerate with the pseudoscalar diquark and the pion is degenerate with the scalar diquark. This can also be seen by noticing that from equation (6.1.6) it follows that

$$\tau_2 G^T[\mu]\tau_2 = G^\dagger[\mu] \ . \tag{8.2.10}$$

See figure (8.1) for a diagrammatic presentation.

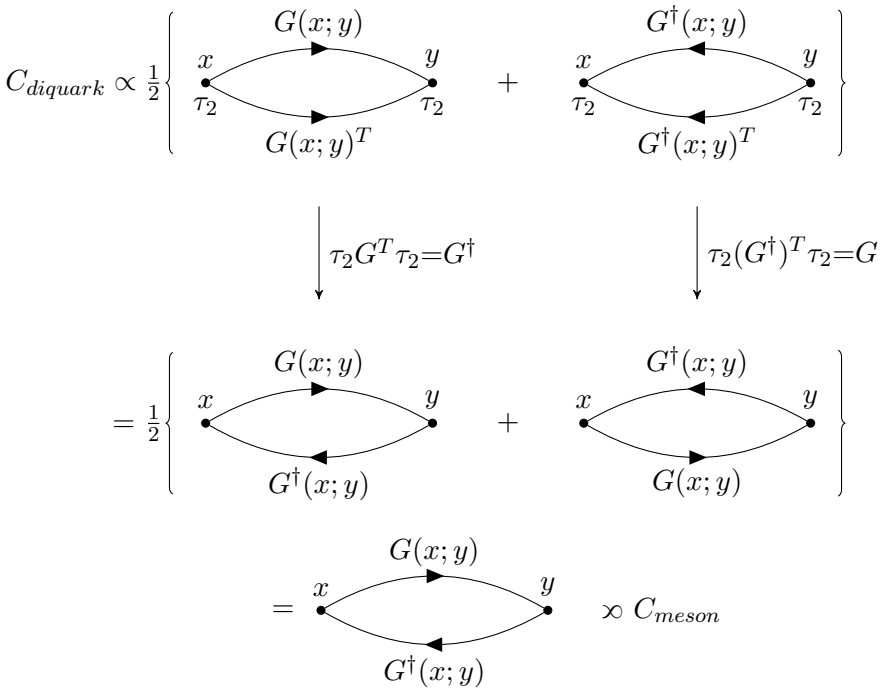

Figure 8.1.: Diagrammatic presentation of the connection of meson and diquark correlators at vanishing chemical potential. The diagram was created with [31].

8.3. The Fitting Procedure

In this section, we will discuss the fitting functions used to extract the masses of the particle modes from their corresponding correlation functions. For channel 1 the expected form of the correlation function is [6][28]

$$C(t; a, b, m_1, m_2) = a(e^{-m_1 t} + e^{-m_1(N_t - t)}) + (-1)^t b(e^{-m_2 t} + e^{-m_2(N_t - t)}) \ , \quad (8.3.1)$$

where we omit the contributions from excited states. This correlation function consists of two parts, one for the positive parity state with proportionality constant a and one for the negative parity state with proportionality constant b. The second term has a factor of $(-1)^t$, indicating the oscillatory behaviour of negative parity states. Each term consists of two exponential functions, one for the propagation in positive time direction and one for the propagation in negative time direction. As mesons do not carry a net baryon number and thus do not couple to the chemical potential, the masses of the two exponential functions are set equal for each parity state. It follows that the correlation function is invariant under time reversal

$$C(t) = C(N_t - t) \ , \quad (8.3.2)$$

indicating a symmetry axis at $t = \frac{N_t}{2}$. In the most cases, we will find that the contribution of the negative parity state is negligible and thus set $b = 0$. The correlation function of channel 2 consists exclusively of a negative parity state, the pion, and hence we use the same form as for channel 1 (8.3.1), however with $a = 0$.

To find the correct fitting form of the correlation functions for the diquark channels 3 and 4, we first discuss the diquark state qq without the explicit contribution from its corresponding anti-diquark. Diquarks couple to the chemical potential as they carry a net baryon number, leading to the favoring of forward propagation over backward propagation. Thus equation (8.3.2) changes for diquarks to [28]

$$C(t, \mu) = C(N_t - t, -\mu) \ , \quad (8.3.3)$$

leading to the expected form of the correlation function given as

$$C(t; a_{qq}, b_{qq}, m^+_{qq}, m^-_{qq}) = a_{qq} \ e^{-m^+_{qq} t} + b_{qq} \ e^{-m^-_{qq}(N_t - t)} \ , \quad (8.3.4)$$

where the +(-) index indicates the mass of the forward(backward) propagating diquark. The same reasoning goes through for purely anti-diquark states $\bar{q}\bar{q}$. Note that from equation (8.3.3) it is clear that the purely diquark or anti-diquark correlators will show an asymmetry in t. Let us now establish the expectation for our combined diquark and anti-diquark channels 3 and 4. For this, we first note that from equation (8.2.4) it follows that

$$C(t)_{qq} = \sum_{\vec{x}} \mathrm{tr}\left[G^T[\mu](\vec{x},t;0)\tau_2 G[\mu](\vec{x},t;0)\tau_2\right] \tag{8.3.5}$$

$$C(t)_{\bar{q}\bar{q}} = \sum_{\vec{x}} \mathrm{tr}\left[G^T[-\mu](\vec{x},t;0)\tau_2 G[-\mu](\vec{x},t;0)\tau_2\right]^* \tag{8.3.6}$$

$$\Rightarrow C(t,-\mu)^*_{qq} = C(t,\mu)_{\bar{q}\bar{q}} \tag{8.3.7}$$

As we expect the correlation function to be real, the complex conjugation in equation (8.3.7) will be ignored. Using this findings, we can obtain the following expectation for our combined diquark state

$$C(t,\mu)_{qq} + C(t,\mu)_{\bar{q}\bar{q}} = C(N_t - t,-\mu)_{qq} + C(N_t - t,-\mu)_{\bar{q}\bar{q}} \tag{8.3.8}$$

$$= C(N_t - t,\mu)_{\bar{q}\bar{q}} + C(N_t - t,\mu)_{qq} \ . \tag{8.3.9}$$

Hence, the asymmetry in t is removed and our combined diquark states have a symmetry axis at $t = \frac{N_t}{2}$, as the mesonic states of channel 1 and 2. If we combine the expected form of the correlation function for the purely diquark state and the purely anti-diquark state $\frac{1}{2}(C_{qq}+C_{\bar{q}\bar{q}})$, we obtain our final form of the fitting function

$$C(t,\bar{a}_{qq},\bar{a}_{\bar{q}\bar{q}},m^+_{qq},m^+_{\bar{q}\bar{q}}) = \bar{a}_{qq}(e^{-m^+_{qq}t} + e^{-m^+_{qq}(N_t-t)}) + \bar{a}_{\bar{q}\bar{q}}(e^{-m^+_{\bar{q}\bar{q}}t} + e^{-m^+_{\bar{q}\bar{q}}(N_t-t)}) \ , \tag{8.3.10}$$

for which we used that

$$m^-_{\bar{q}\bar{q}} = m^+_{qq} \qquad b_{qq} = a_{\bar{q}\bar{q}} \qquad \bar{a}_{qq} = \frac{a_{qq}}{2}$$

$$m^-_{qq} = m^+_{\bar{q}\bar{q}} \qquad b_{\bar{q}\bar{q}} = a_{qq} \qquad \bar{a}_{\bar{q}\bar{q}} = \frac{a_{\bar{q}\bar{q}}}{2} \ .$$

The contributions from excited states have been omitted again. Lastly, we note that we use the relation

$$e^{-mt} + e^{-m(N_t-t)} = 2\cosh\left(m\left(t - \frac{N_t}{2}\right)\right) \tag{8.3.11}$$

to rewrite the fitting functions, as this is found to give more stable fits.

To sum up, we have identified the correlation functions for the meson and diquark modes which we wish to inspect, we have shown how they can be calculated in lattice simulations and found suiting fitting functions to extract the masses of the particle modes. The extracted masses from our lattice simulations will then be compared to the predictions of leading order chiral perturbation theory, see section {9.3}.

9. Leading Order Chiral Perturbation Theory

This section will introduce leading order chiral perturbation theory applied to continuum any color QCD with quarks in the adjoint representation at finite chemical potential. The reason for not studying continuum two-color QCD with fundamental quarks is that it has the pattern of spontaneous symmetry breaking of $SU(2N_f) \to Sp(2N_f)$, whereas continuum any color QCD with quarks in the adjoint representation has the pattern of $SU(2N_f) \to SO(2N_f)$, which is more familiar to the pattern of two-color lattice QCD with staggered quarks $U(2N_f) \to O(2N_f)$. The difference only arises from the axial anomaly, as the $U(1)_A$ symmetry can not be broken spontaneously in a lattice formulation. As we did in the lattice formulation of two-color QCD, here we will also include an explicit diquark source term into the effective Lagrangian, which is possible because diquarks are colorless in the adjoint representation and thus the diquark source term is gauge invariant [29]. We will find predictions for the chiral condensate, the diquark condensate and the baryon number density, as well as for the Goldstone spectrum, which we later fit or compare to our data obtained from lattice simulations.

9.1. The Effective Lagrangian

Starting from the microscopic Lagrangian of any color QCD with N_f quarks in the adjoint representation at finite quark mass, diquark source and chemical potential [29]

$$\mathcal{L} = \bar{\psi}\gamma_\nu D_\nu \psi + m\bar{\psi}\psi - \mu\bar{\psi}\gamma_0\psi + \frac{\lambda}{2}\left(i\psi^T C\gamma_5\psi + h.c.\right) \ , \tag{9.1.1}$$

with an implicit sum over N_f quark flavors and suppressed color and spin indices, we show how the effective Lagrangian for the Goldstone modes, induced from the spontaneous symmetry breaking by quark condensation, can be obtained. We stress that we can use the antisymmetry property of the generators of the adjoint representation, which are the structure constants, $f_a^{bc} = -f_a^{cb}$ to rewrite the terms of the microscopic Lagrangian by introducing spinors of length $2N_f$, given by [29]

$$\Psi \equiv \begin{pmatrix} \psi_L \\ \sigma_2\psi_R^* \end{pmatrix} \equiv \begin{pmatrix} \psi_L \\ \tilde{\psi}_R \end{pmatrix} \ . \tag{9.1.2}$$

This is just the same approach as in section {7}, where now the antisymmetry property of the generators of the adjoint representation takes over the role of the

pseudo-reality of the generators of the fundamental representation. Note that here σ_2 (resp. σ_ν) is a Pauli matrix acting on the spinor indices as opposed to the Pauli matrix τ_2 acting on the color indices in previous chapters. The kinetic part can now be written as

$$\mathcal{L}_{kin} = i\Psi^\dagger \sigma_\nu D_\nu \Psi \ , \tag{9.1.3}$$

which has an enlarged $U(2N_f)$ symmetry compared to the original $U(N_f)_L \times U(N_f)_R$. As already noted in section {3.3}, the axial anomaly breaks this symmetry down to $SU(2N_f)$. For the source terms, mass term and diquark term, we obtain

$$\mathcal{L}_m = -\frac{1}{2}\ \Psi^T \sigma_2 M \Psi + h.c. \ , \tag{9.1.4}$$

$$\mathcal{L}_\lambda = -\frac{1}{2}\ \Psi^T \sigma_2 \Lambda \Psi + h.c. \ , \tag{9.1.5}$$

$$\text{with} \quad M = m\hat{M} = m \begin{pmatrix} 0 & 1 \\ 1 & 0 \end{pmatrix} \quad \text{and} \quad \Lambda = \lambda\hat{\Lambda} = \lambda \begin{pmatrix} -i & 0 \\ 0 & -i \end{pmatrix} \ .$$

The blocks of the matrices $\hat{M}$ and $\hat{\Lambda}$ are of dimension $N_f \times N_f$. The two terms can be combined by introducing the combined mass matrix [29]

$$M_\phi \equiv m\hat{M} + \lambda\hat{\Lambda} = \sqrt{m^2+\lambda^2}\left(\cos\phi\ \hat{M} + \sin\phi\ \hat{\Lambda}\right) \equiv \sqrt{m^2+\lambda^2}\ \hat{M}_\phi \ . \tag{9.1.6}$$

The angle ϕ is connected to the mass and the diquark source through $\tan(\phi) = \frac{\lambda}{m}$. As in the lattice formalism, at vanishing chemical potential the source terms can be rotated into each other by an explicit $SU(2N_f)$ rotation. Including non-vanishing source terms leads to an explicit symmetry breaking of the $SU(2N_f)$ symmetry down to $SO(2N_f)$, whereas a chiral condensate or a diquark condensate cause a spontaneous symmetry breaking. The explicit $SU(2N_f)$ rotation which connects the source terms also connects the condensates and thus they are physically indistinguishable. The Goldstone manifold of the spontaneous symmetry breaking is given by the coset $SU(2N_f)/SO(2N_f)$, corresponding to $N_f(2N_f+1)-1$ pseudo Goldstone bosons, which obtain mass from the explicit symmetry breaking [29]. From the combined mass term it follows that the condensate in the effective theory for the Goldstone modes is a symmetric unimodular unitary matrix denoted by Σ. The Goldstone boson spectrum will be inspected in section {9.3}. We construct the kinetic part of the effective Lagrangian of the pseudo Goldstone modes by requiring invariance under $SU(2N_f)$ rotations of the condensate $\Sigma \to V\Sigma V^T$, we obtain [32]

$$\mathcal{L}_{\text{eff},kin} = \frac{F^2}{2}\text{tr}\left[\partial_\nu \Sigma \partial_\nu \Sigma^\dagger\right] \ , \tag{9.1.7}$$

with F being the pion decay constant. To construct the combined source term for the effective theory, we note that we can achieve full $SU(2N_f)$ symmetry for the

microscopic source terms by formally transforming the combined mass matrix under $SU(2N_f)$ transformations according to [29]

$$M_\phi \to V^* M_\phi V^\dagger \tag{9.1.8}$$

and hence the leading order combined source term of the effective theory obeying this formal extended symmetry is given by

$$\mathcal{L}_\phi = -\sqrt{m^2+\lambda^2}G \text{ Re tr}\left[\hat{M}_\phi \Sigma\right] \ . \tag{9.1.9}$$

Using the Gell-Mann–Oakes–Renner relation, $m_\pi^2 F^2 = \sqrt{m^2+\lambda^2}G$ [2], we can trade the phenomenological coefficient G and obtain the effective Lagrangian for the Goldstone modes at vanishing chemical potential

$$\mathcal{L}_{\text{eff}}(\Sigma) = \frac{F^2}{2}\left\{\text{tr}\left[\partial_\nu \Sigma \partial_\nu \Sigma^\dagger\right] - 2m_\pi^2 \text{Re tr}\left[\hat{M}_\phi \Sigma\right]\right\} \ . \tag{9.1.10}$$

Next, we shall consider the influences of a non-vanishing chemical potential to the pattern of symmetry breaking and the effective Lagrangian of the Goldstone modes. The chemical potential dependent term of the microscopic Lagrangian can be rewritten in the new basis as [29]

$$\mathcal{L}_\mu = \mu \Psi^\dagger B \Psi \quad , \quad B = \begin{pmatrix} 1 & 0 \\ 0 & -1 \end{pmatrix} \ . \tag{9.1.11}$$

Like the source terms, this term is $SU(2N_f)$ symmetry violating

$$SU(2N_f) \to SU(N_f)_R \times SU(N_f)_L \times U(1)_B \tag{9.1.12}$$

and again one tries to find a formal symmetry transformation for the matrix B to restore the full symmetry. By introducing the four-vector $B_\nu = (B, \vec{0})$ [29], we can write the chemical potential dependent term together with the kinetic term

$$\mathcal{L}_{kin} + \mathcal{L}_\mu = i\Psi^\dagger \sigma_\nu \left(D_\nu - \mu B_\nu\right)\Psi \ . \tag{9.1.13}$$

In this form we can see that the chemical potential dependent term looks like an additional gauge field. Thus, in the usual manner for gauge fields [2], we can even find a local symmetry transformation for the four-vector B_ν given by [32]

$$B_\nu \to V B_\nu V^\dagger + \frac{1}{\mu} V \partial_\nu V \ . \tag{9.1.14}$$

To ensure this formal symmetry in the effective theory, the derivatives of the condensate have to be replaced by covariant derivatives [29]

$$\begin{aligned} \nabla_\nu \Sigma &= \partial_\nu \Sigma - \mu\left(B_\nu \Sigma + \Sigma B_\nu^T\right) \\ \nabla_\nu \Sigma^\dagger &= \partial_\nu \Sigma^\dagger + \mu\left(\Sigma^\dagger B_\nu + B_\nu^T \Sigma^\dagger\right) \end{aligned} \tag{9.1.15}$$

and the final result for the leading order effective Lagrangian at non-vanishing chemical potential, including a mass term and a diquark term, is thus given by

$$\mathcal{L}_{\text{eff}}(\Sigma) = \frac{F^2}{2}\left\{\text{tr}\left[\nabla_\nu \Sigma \nabla_\nu \Sigma^\dagger\right] - 2m_\pi^2 \text{Re tr}\left[\hat{M}_\phi \Sigma\right]\right\} \ . \tag{9.1.16}$$

9.2. Predictions for the Condensates and the Baryon Number Density

Next, we want to obtain the predictions for the chiral condensate, the diquark condensate and the baryon number density coming from the effective Lagrangian (9.1.16). For this, we need to find the orientation of the condensate in dependence on the chemical potential, which is in general fixed by the vacuum alignment of the condensate Σ and is determined by the static part of the effective Lagrangian. It can be shown that the condensate rotates from a mixed condensate at $\mu = 0$ to a purely diquark condensate at $\mu = \infty$ [29], parameterized by a rotation angle α

$$\Sigma_\alpha \equiv \Sigma_c \ \cos\alpha + \Sigma_d \ \sin\alpha \ , \tag{9.2.1}$$

where Σ_c is the chiral condensate and Σ_d is the diquark condensate at vanishing chemical potential. For $\mu = 0$ the static part of the effective Lagrangian is completely determined by the combined mass term, which is minimized for $\Sigma = M_\phi^\dagger$ and thus we find the two matrices for the condensates

$$\Sigma_c = \hat{M}^\dagger = \begin{pmatrix} 0 & 1 \\ 1 & 0 \end{pmatrix} \ , \ \Sigma_d = \hat{\Lambda}^\dagger = \begin{pmatrix} i & 0 \\ 0 & i \end{pmatrix} \ . \tag{9.2.2}$$

The boundary values of the rotation angular are given by $\alpha \in \left[\phi, \frac{\pi}{2}\right]$. To obtain the dependence of the rotation angular α on the chemical potential, we substitute Σ_α into the static part of the Lagrangian and obtain [29]

$$\mathcal{L}_{st}(\Sigma_\alpha) = F^2 m_\pi^2 N_f \left[\frac{2\mu^2}{m_\pi^2}\left(\cos(2\alpha) - 1\right) - 2\cos(\alpha - \phi)\right] \ . \tag{9.2.3}$$

Minimizing with respect to α gives the equation

$$4\mu^2 \sin\alpha \ \cos\alpha = m_\pi^2 \sin(\alpha - \phi) \ , \tag{9.2.4}$$

which can be solved for α, giving an analytic function $\alpha(\mu)$. To obtain the desired predictions, we calculate the vacuum energy, which is given by the effective Lagrangian at the minimum $\Sigma_{\alpha(\mu)}$. After some resorting, we obtain

$$\varepsilon_{vac} = -4N_f F^2 \mu^2 \sin^2\alpha(\mu) - 2N_f G\left(m\cos\alpha(\mu) + j\sin\alpha(\mu)\right) \ , \tag{9.2.5}$$

from which we arrive at the leading order predictions for the chiral condensate, the diquark condensate and the baryon number density, given by [29]

$$\langle\bar{\psi}\psi\rangle = -\frac{\partial\varepsilon_{vac}}{\partial m} = 2N_f G\cos\alpha(\mu)\ , \tag{9.2.6}$$

$$\langle\psi\psi\rangle = -\frac{\partial\varepsilon_{vac}}{\partial\lambda} = 2N_f G\sin\alpha(\mu)\ , \tag{9.2.7}$$

$$\langle n_B\rangle = -\frac{\partial\varepsilon_{vac}}{\partial\lambda} = 8N_f F^2\mu\sin^2\alpha(\mu)\ . \tag{9.2.8}$$

It is easy to see, that chiral perturbation theory at this order predicts the condensate $\sqrt{\langle\bar{\psi}\psi\rangle^2 + \langle\psi\psi\rangle^2}$ to be independent of the chemical potential. In figure (9.1) we have plotted these functions for a diquark source of $\lambda = 0.1m$. We can see that up to a critical value of the chemical potential, denoted by μ_c, the baryon number density is zero and then increasing with the chemical potential. Around this point, also the chiral condensate begins to decrease and the diquark condensate begins to increase. It is visible that the condensate will be a pure diquark condensate for $\mu = \infty$, as already noted. To get a better insight on the value of μ_c, we now inspect the limit of vanishing diquark source $\lambda \to 0$.

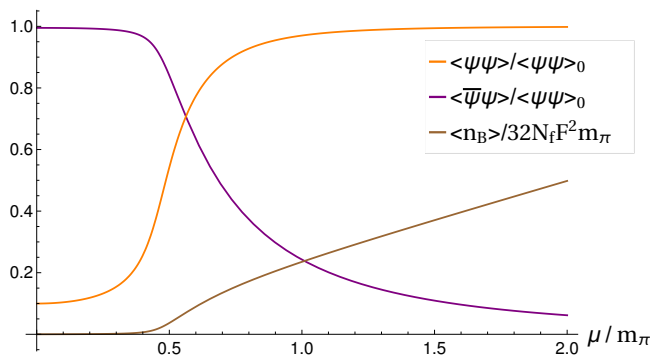

Figure 9.1.: Predictions from leading order chiral perturbation theory with a diquark source of $\lambda = 0.1m$.

From setting $\lambda = 0$ it follows that $\phi = 0$ and hence the effective Lagrangian (9.2.3) is now minimized by [29]

$$\alpha = \begin{cases} 0 & , \frac{2\mu}{m_\pi} < 1 \\ \arccos\left(\frac{m_\pi^2}{4\mu^2}\right) & , \frac{2\mu}{m_\pi} > 1 \end{cases} .$$

As for $\alpha = 0$ the diquark condensate and the baryon density vanish, we find for the critical chemical potential $\mu_c = \frac{m_\pi}{2}$. Figure (9.2) shows the predictions for the condensates and the baryon number density at vanishing diquark source. Note that the non-analytic dependence of the rotation angle α is an indication of a phase

transition at $\mu = \mu_c$ with the diquark condensate as order parameter, which will become more evident by the following symmetry considerations.

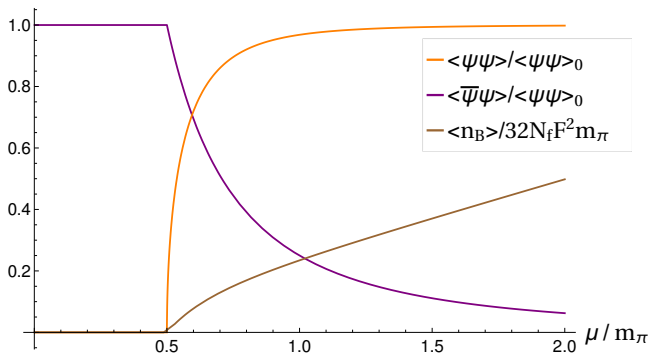

Figure 9.2.: Predictions from leading order chiral perturbation theory at vanishing diquark source.

Let us summarize the spontaneous symmetry breaking induced by the chiral condensate and the diquark condensate at non-vanishing chemical potential:

$$\begin{aligned}
&\text{Symmetry at } \mu \neq 0: \\
&SU(N_f)_L \times SU(N_f)_R \times U(1)_B \quad \Rightarrow \quad \Sigma_c \quad \rightarrow \quad SU(N_f)_V \times U(1)_B \\
&\qquad\qquad\qquad\qquad\qquad\qquad\qquad\quad \Sigma_d \quad \rightarrow \quad SO(N_f)_V
\end{aligned}$$

As we still consider a non-vanishing quark mass, the symmetries which are broken by the chiral condensate are already broken explicitly, therefore the corresponding Goldstone bosons will be massive. Whereas for vanishing diquark source we have an exclusive spontaneous symmetry breaking of baryon number conservation and also from $SU(N_f)_V$ to $SO(N_f)_V$, inducing massless Goldstone bosons into the system. Thus, it is obvious that the system undergoes a phase transition at $\mu = \mu_c$, where diquarks start to condense. If a diquark source term is included into the effective Lagrangian, the remaining symmetry of the system is $SO(N_f)_V$ for all values of the chemical potential and hence there is only one phase. By fitting the predictions (9.2.6)-(9.2.8) to our numerical data, we can obtain the value of the critical chemical potential μ_c for the systems of our simulations. Lastly, for a better intuition we visualized the dependence of these predictions on the chemical potential and the diquark source in figure (9.3).

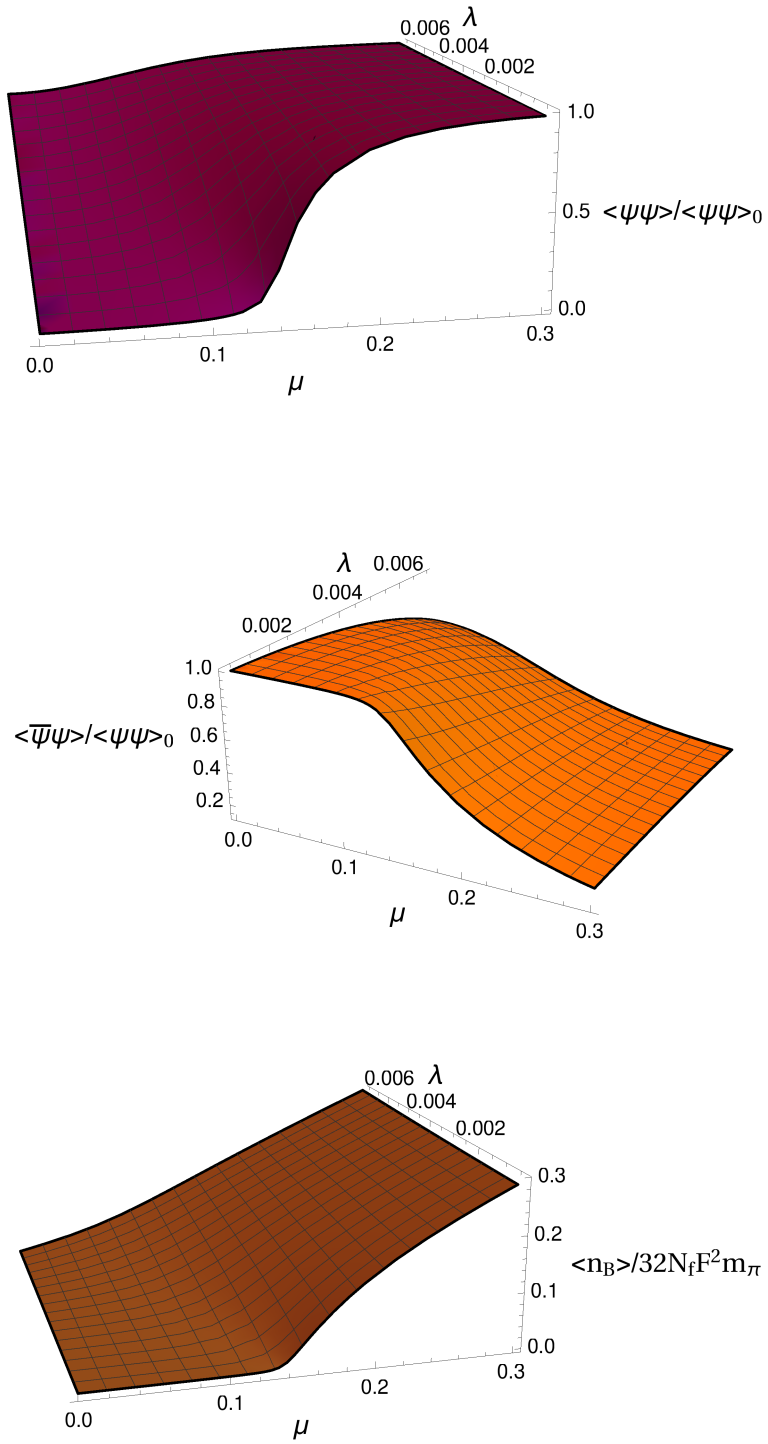

Figure 9.3.: Dependence of the diquark condensate (top), the chiral condensate (middle) and the baryon number density (bottom) on the chemical potential and the diquark source.

9.3. Predictions for the Goldstone Spectrum

Lastly, we will consider the predictions of leading order chiral perturbation theory for the masses and the degeneracies of the (pseudo) Goldstone bosons. Again, we first inspect the general case of a non-vanishing diquark source and then take the limit $\lambda \to 0$. The whole Goldstone manifold given by the coset $SU(2N_f)/SO(2N_f)$, corresponding to the fluctuations of the condensate Σ around its vacuum value Σ_α, can be parameterized by applying the rotations [29]

$$\Sigma = V_\alpha U \Sigma_c U^T V_\alpha^T \tag{9.3.1}$$

$$U = \exp\left(\frac{i\Pi}{2F}\right) \quad , \quad \Pi = \pi_a \frac{X_a}{\sqrt{2N_f}} \quad , \quad V_\alpha^2 = \exp\left(i\alpha X_2\right) \ , \tag{9.3.2}$$

where the Goldstone modes are described by the fields π_a, the matrices X_a are the generators of the coset $SU(2N_f)/SO(2N_f)$ and F is the pion decay constant. The matrix V_α is used to express the parameterization (9.2.1) in another way [29]

$$\Sigma_\alpha = V_\alpha \Sigma_c V_\alpha^T \ , \tag{9.3.3}$$

where the chiral condensate Σ_c is rotated into a diquark condensate Σ_d by the generator X_2. It can be shown that the Goldstone matrix Π can be split up into $N_f \times N_f$ blocks with the following properties [29]

$$\Pi = \begin{pmatrix} P^T & Q \\ Q^\dagger & P \end{pmatrix} \ , \tag{9.3.4}$$

$$\mathrm{tr} P = 0 \ , \quad P^\dagger = P \ , \quad Q^T = Q \ . \tag{9.3.5}$$

The quark-antiquark modes belong to the P modes and the (anti-)diquark modes belong to the $Q^{(\dagger)}$ modes. The number of independent components of the matrices P and Q is equal to the degeneracies of the Goldstone modes. Using the properties (9.3.5), one can count them in dependence of the number of quark flavors N_f

$$N_P = N_f^2 - 1 \ , \tag{9.3.6}$$

$$N_Q = N_f(N_f + 1) \ . \tag{9.3.7}$$

To obtain the leading order predictions of the spectrum of the Goldstone modes, the parameterization of the condensate (9.3.1) is plugged into the effective Lagrangian, which then is expanded up to second order in the Goldstone matrix Π

$$U = \left(1 + \frac{i\Pi}{2F} - \frac{\Pi^2}{4F^2} + \cdots\right) \tag{9.3.8}$$

and finally one uses a Fourier decomposition of the Goldstone fields to obtain the dispersion laws. This procedure is lengthy and thus we here only state the final results for the dispersion laws, for which also the projections

$$P_S = \frac{1}{2}\left(P + P^T\right) \qquad P_A = \frac{1}{2}\left(P - P^T\right) \tag{9.3.9}$$

$$Q_R = \frac{1}{2}\left(Q + Q^\dagger\right) \qquad Q_L = \frac{1}{2}\left(Q - Q^\dagger\right) \tag{9.3.10}$$

are used. Refer for details to [29]. For the number of independent components of the projected P and Q modes it can be found that

$$N_{P_A} = \frac{N_f(N_f-1)}{2}\ , \tag{9.3.11}$$

$$N_{P_S} = \frac{N_f(N_f+1)}{2} - 1\ , \tag{9.3.12}$$

$$N_{Q_R} = N_{Q_I} = \frac{N_f(N_f+1)}{2}\ . \tag{9.3.13}$$

Let us now state the final result for the dispersion laws of the Goldstone modes

$$\begin{aligned}
P_A \quad &\Rightarrow \quad E^2 = \vec{p}^2 + m_\pi^2\left(\frac{4\mu^2}{m_\pi^2} + \frac{\sin\phi}{\sin\alpha}\right) \\
P_S \quad &\Rightarrow \quad E^2 = \vec{p}^2 + m_\pi^2\left(\frac{4\mu^2}{m_\pi^2}\cos^2\alpha + \frac{\sin\phi}{\sin\alpha}\right) \\
\tilde{Q} \quad &\Rightarrow \quad E^2 = \vec{p}^2 + m_\pi^2\frac{\sin\phi}{\sin\alpha} + 2\mu^2\left(1+3\cos^2\alpha\right) \\
&\qquad - 2\mu\sqrt{\mu^2\left(1+3\cos^2\alpha\right)^2 + 4\cos^2\alpha\left(\vec{p}^2 + m_\pi^2\frac{\sin\phi}{\sin\alpha}\right)} \\
\tilde{Q}^\dagger \quad &\Rightarrow \quad E^2 = \vec{p}^2 + m_\pi^2\frac{\sin\phi}{\sin\alpha} + 2\mu^2\left(1+3\cos^2\alpha\right) \\
&\qquad + 2\mu\sqrt{\mu^2\left(1+3\cos^2\alpha\right)^2 + 4\cos^2\alpha\left(\vec{p}^2 + m_\pi^2\frac{\sin\phi}{\sin\alpha}\right)}\ ,
\end{aligned} \tag{9.3.14}$$

where $\tilde{Q}$ and $\tilde{Q}^\dagger$ are independent linear combinations of Q_R and Q_I. In figure (9.4) we have plotted the masses of the Goldstone bosons at a diquark source of $\lambda = 0.1m$. Notice that the meson modes P are degenerate up to the critical chemical potential μ_c, whereas here the diquark modes $\tilde{Q}$ and the antidiquark modes $\tilde{Q}^\dagger$ split up according to their baryon charges of $b = \pm 2$. For $\mu > \mu_c$ the meson modes P also split up and become degenerate with (anti-)diquark states for large values of the chemical potential. We stress again that there are no true Goldstone bosons due to the explicit symmetry breaking. Next, we turn to the spectrum for vanishing diquark source, where we have true Goldstone bosons.

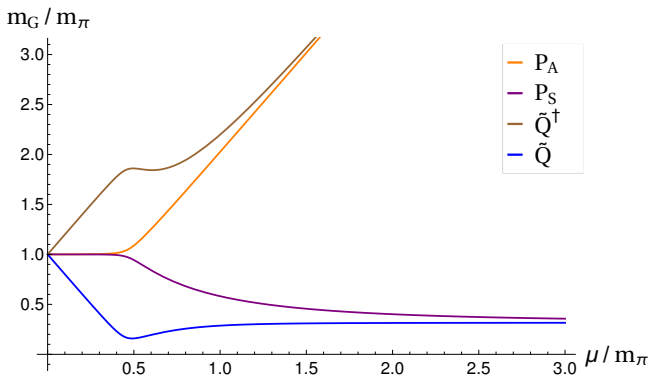

Figure 9.4.: Predictions from leading order chiral perturbation theory with a diquark source of $\lambda = 0.1m$.

The spectrum for $\mu > \mu_c$ at vanishing diquark source can be obtained by setting $\phi = 0$ in equations (9.3.14), but for $\mu < \mu_c$ one has to do a separate calculation as we now have a phase transition at μ_c and the residual symmetry for $\mu < \mu_c$ is given by $SU(N_f)_V \times U(1)_B$. In this phase the dispersion laws for the Goldstone modes are given by [29]

$$\begin{aligned} P &\Rightarrow E = \sqrt{\vec{p}^2 + m_\pi^2} \\ Q &\Rightarrow E = \sqrt{\vec{p}^2 + m_\pi^2} + 2\mu \\ Q^\dagger &\Rightarrow E = \sqrt{\vec{p}^2 + m_\pi^2} - 2\mu \end{aligned} \tag{9.3.15}$$

These dispersion laws explicitly show the splitting of the modes in dependence on their baryon charges $b = 0, \pm 2$. A combined plot showing the masses of the Goldstone bosons for the two distinct phases is given in figure (9.5). A true Goldstone mode, induced by the spontaneous symmetry breaking of baryon number conservation, is now visible in the diquark condensation phase for $\mu > \mu_c$.

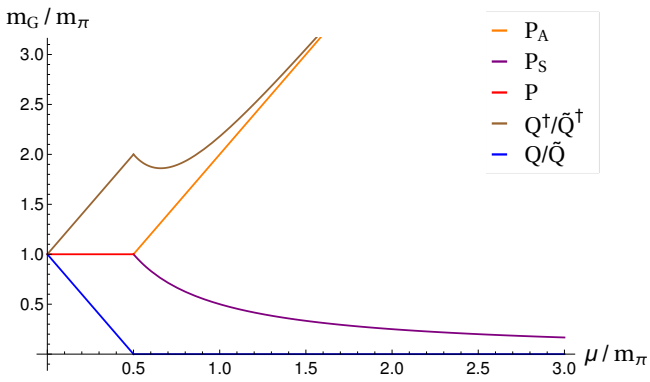

Figure 9.5.: Predictions from leading order chiral perturbation theory at vanishing diquark source.

10. Numerical Results

The numerical results obtained from our lattice simulations shall now be presented. We will start with a discussion on the possibility of using real pseudofermions to reduce the number of continuum quark flavors, motivated in section {6.1}. Then, first results of the condensates and the quark number density at non-vanishing chemical potential are presented. We compare the diquark condensate of a two flavor and a four flavor simulation. The influence of the $\mathbb{Z}(2)$ monopole density will be discussed, leading to a new choice of lattice parameters for our final simulation. This simulation will show the need to renormalize the chiral condensate. Furthermore, the meson spectrum at finite density for both simulations is investigated.

The numerical results were produced using the OpenCL code from Lukas Holicki and the CUDA code from Dominik Smith, both capable of $\mathrm{LQC_2D}$ Monte Carlo simulations with (rooted) staggered quarks.

Note that from lattice simulations we only obtain dimensionless quantities. Every physical quantity is multiplied by a corresponding order of the lattice spacing a. For example, we do not measure $\langle\bar{\psi}\psi\rangle$ in lattice simulations but $a^3\langle\bar{\psi}\psi\rangle$. Furthermore, the parameters of the fermion action, which we regulate, have a factor of the lattice spacing, $m \to am$ and $\mu \to a\mu$, whereas the inverse coupling β and the diquark source λ are already dimensionless. For clarity, we do not explicitly show these factors of the lattice spacing a in this section.

10.1. Real Pseudofermions

We measured the Polyakov loop expectation value for a $20^3 \times 8$ lattice with a quark mass of $m = 0.15$ at vanishing chemical potential μ and diquark source λ. To check if we really reduce the number of flavors, we run the calculations with real and complex pseudofermions, which should correspond to four and eight quark flavors, respectively. Furthermore, we checked if the rescaling of the fermion action, and therefore of the fermion force, by a factor of $\frac{1}{2}$ as suggested by [7] might have the same effect as using real pseudofermions. Remember that we do not generate real pseudofermions directly, but instead use real η for the generation of the pseudofermions so that they have the same number of degrees of freedom as real pseudofermions. The results are shown in figure (10.1), where we also compare them to a four flavor calculation obtained by using the rational HMC.

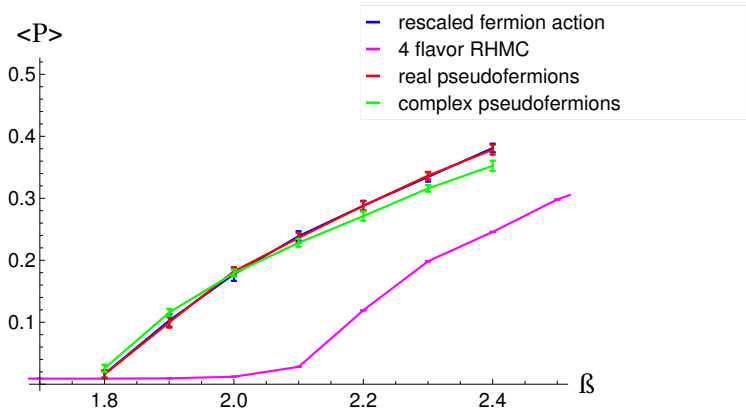

Figure 10.1.: The Polyakov loop for $N_s = 20$, $N_t = 8$, $m = 0.15$, $\mu = 0$ and $\lambda = 0$.

From figure (10.1) we see that using real pseudofermions or rescaling by $\frac{1}{2}$ actually has the same result. However, they do not agree with the Polyakov loop obtained by using the rational HMC to reduce to $N_f = 4$. Still, they do not lie on the resulting curve from using complex fermions either. We conclude that we neither obtain a theory of $N_f = 4$ nor remain at the theory of $N_f = 8$ quark flavors. From an additional calculation of the Polyakov loop we found that the rescaling factor of $\frac{1}{2}$ can be compensated by adjusting the standard deviation of the Gaussian distribution for the generation of the η from $\sigma = \frac{1}{\sqrt{2}}$ to $\sigma = 1$, giving the $N_f = 8$ case again. Hence, the number of quark flavors can not be reduced by simply using real pseudofermions or rescaling the fermion action by $\frac{1}{2}$. An explanation for this can be found by noticing that using real η changes the measure of the pseudofermions. Remember that, when using pseudofermions to express the fermion determinant, the expectation value of an operator is given by

$$\langle O \rangle = \frac{1}{Z} \int \mathcal{D}U \int\limits_{\mathbb{C}^{N_c} \times \mathbb{C}^{N_c}} \left[\mathcal{D}\phi^\dagger \mathcal{D}\phi \right] O\left(U, D^{-1}\right) \; e^{-S_G[U] - S_F[\phi, \phi^\dagger, U]} \; . \tag{10.1.1}$$

As the integral of the pseudofermions is over the whole complex space, we can treat them as a constant background field during the integration of the link variables and update them only at the beginning of the molecular dynamics trajectory, as already mentioned in section {4.2}. In the case of complex η the pseudofermions get generated over the whole complex space through $\phi = D(U)\eta$, where the current gauge field configuration does not matter. We have

$$D(U) \; : \; \mathbb{C}^{N_c} \; \rightarrow \; \mathbb{C}^{N_c} \quad \forall U \; . \tag{10.1.2}$$

If we go over to real η, the gauge field configuration becomes important in the generation of the pseudofermions and now we have

$$D(U) \;:\; \mathbb{R}^{N_c} \;\rightarrow\; A(U) \subset \mathbb{C}^{N_c} \;, \tag{10.1.3}$$

according to the reduction of the fermionic degrees of freedom. The expectation value of an operator changes in the same manner

$$\langle O \rangle = \frac{1}{Z} \int \mathcal{D}U \int\limits_{V(U)} \left[\mathcal{D}\phi^\dagger \mathcal{D}\phi\right] O\left(U, D^{-1}\right) \; e^{-S_G[U] - S_F[\phi,\phi^\dagger,U]} \;, \tag{10.1.4}$$

with $V(U) \subset \mathbb{C}^{N_c} \times \mathbb{C}^{N_c}$. The pseudofermion integral is reduced to a subspace of the complex space which depends on the current gauge field configuration. This means that we can not treat the pseudofermions as a constant background field anymore as a change of a single link variable $U \rightarrow U'$ can cause the $\phi \in A(U)$, created at the beginning of the molecular dynamics trajectory, to lie outside of the resulting new $A(U')$: $\phi \notin A(U')$. Hence, the reduction of the number of fermionic degrees of freedom is not guaranteed to maintain during the molecular dynamics trajectory. After updating a single link variable, we would need to recalculate the pseudofermions, making the HMC algorithm not feasible.

Based on this first finding, we decided to use the rational HMC for our simulations at finite density, reducing to $N_f = 2$ quark flavors.

10.2. Simulating inside the Bulk Phase

Our first simulations at non-vanishing chemical potential were done on a $N_s = 12$ and $N_t = 24$ lattice, at an inverse coupling of $\beta = 1.5$ and a quark mass of $m = 0.025$. We used two different diquark sources $\lambda = 0.0025, 0.005$. These are the same parameters as in [1] for a $N_f = 4$ quark flavor study. The results for the flavor-normalized condensates and the flavor-normalized quark number density are shown in figures (10.2) and (10.3).

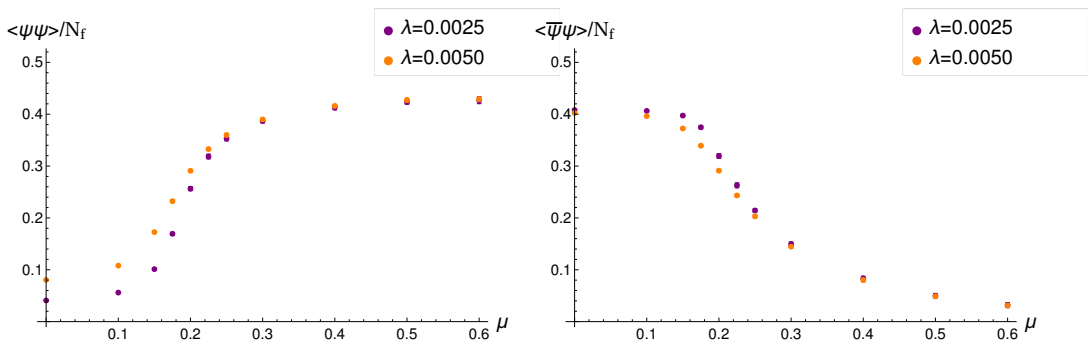

Figure 10.2.: The diquark condensate (left panel) and the chiral condensate (right panel).

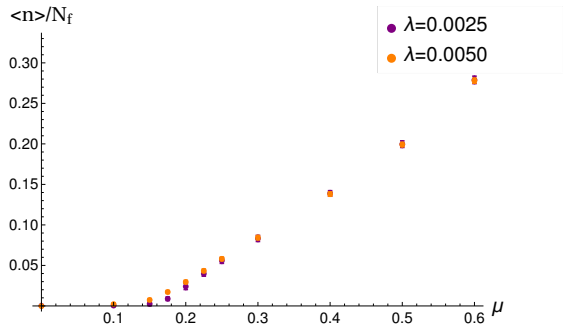

Figure 10.3.: The quark number density.

These results look very similar to the expectations from leading order chiral perturbation theory (see section {9.2}). We see a non-vanishing diquark condensate at $\mu = 0$ due to the explicit symmetry breaking of the included diquark source term. The diquark condensate and the quark number density begin to increase at a critical value of the chemical potential μ_c, where the chiral condensate begins to decrease. To obtain the according value of μ_c, we fitted our numerical data to the expectations from leading order chiral perturbation theory, equations (9.2.6)-(9.2.8). The resulting fits for both diquark sources λ are shown in figure (10.4) and the results for the fit parameters are shown in table (10.1).

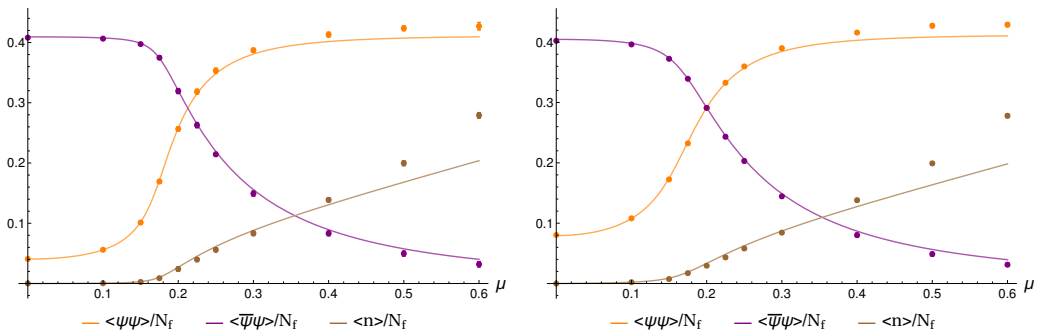

Figure 10.4.: Fits to leading order chiral perturbation theory for $\lambda = 0.0025$ (left panel) and $\lambda = 0.005$ (right panel).

λ	$2G$	$8F^2$	μ_c	m	χ^2/DOF
0.0025	0.41135(88)	0.3430(68)	0.18889(45)	0.02527(13)	1.93
0.0050	0.41235(73)	0.3335(46)	0.18931(47)	0.02547(15)	3.64

Table 10.1.: The resulting fit parameters.

We obtain similar fit parameters for both λ, the χ^2/DOF is not that much larger than 1 and the quark mass is close to its lattice value of $m = 0.025$, indicating the goodness of the fits. Notice that a deviation of the data from the fit becomes visible at large chemical potential. This can be explained with next to leading order chiral perturbation theory, from which follows that the combined condensate is not independent of μ anymore [33]. A rising combined condensate at large μ is also found in a quark-meson-diquark model study [34]. Chiral perturbation theory predicts the connection between the critical chemical potential μ_c and the pion mass as $\mu_c = \frac{m_\pi}{2}$ (see section {9.2}), which is still true beyond leading order. To check this connection, we have measured the pion correlator at vanishing chemical potential (channel 2 from section {8}) and extracted the pion mass from it by employing a single-cosh fit. The correlation functions with the resulting fits are shown in figure (10.5) and the pion masses are listed in table (10.2), where we also show the corresponding μ_c. The two values in the brackets account for the statistical and the total error. We approximated the systematic error by varying both ends of the fit interval by ± 1 and combined the statistical and systematic error quadratically $\sigma_{\text{tot}} = \sqrt{\sigma_{\text{stat}}^2 + \sigma_{\text{sys}}^2}$.

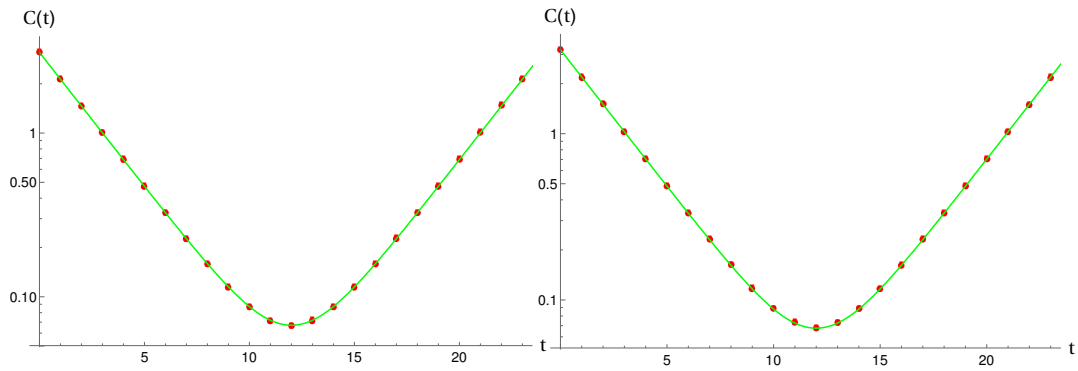

Figure 10.5.: Fits to the pion correlator for $\lambda = 0.0025$ (left panel) and $\lambda = 0.005$ (right panel).

λ	m_π	μ_c
0.0025	0.3774(03)(11)	0.1887(02)(06)
0.0050	0.3791(06)(16)	0.1896(03)(08)

Table 10.2.: The extracted pion masses and corresponding critical chemical potentials.

The obtained values for μ_c from the chiral perturbation theory fits and from the pion correlators are in perfect agreement. In figure (10.6) we show the results for the Polyakov loop and the $\mathbb{Z}(2)$ monopole density. The Polyakov loop is constant

within the errorbars over the whole range of μ, but close to zero. It obtains its small finite value from the dynamical quarks due to the string breaking, as explained in section {2.6}, and the finite volume. The $\mathbb{Z}(2)$ monopole density is very large for all values of μ at which we simulated, meaning that we are deep inside the unphysical bulk phase. Thus, even though the obtained results look really good and match chiral perturbation theory predictions, the influence of the artificial bulk phase on the physical behaviour of the system is unclear. Due to this result, we decided to run a simulation at a smaller $\mathbb{Z}(2)$ monopole density, leading to different lattice parameters. The choice of the new lattice parameters is explained in the next section {10.3}, where we also show the obtained results. To explain the increase in the $\mathbb{Z}(2)$ monopole density at large μ we also refer to this section.

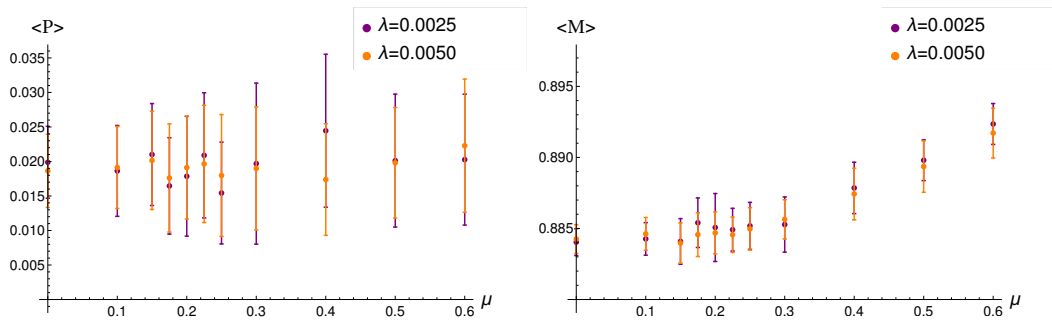

Figure 10.6.: The Polyakov loop (left panel) and the $\mathbb{Z}(2)$ monopole density (right panel).

Furthermore, we compare our $N_f = 2$ flavor result of the diquark condensate to the $N_f = 4$ flavor result in [1], shown in figure (10.7), where we also include our fit to leading order chiral perturbation theory to guide the eye. Notice the different normalization of the diquark condensate for comparison. We see that the flavor-normalized diquark condensate for less flavors is larger at all values of μ simulated here.

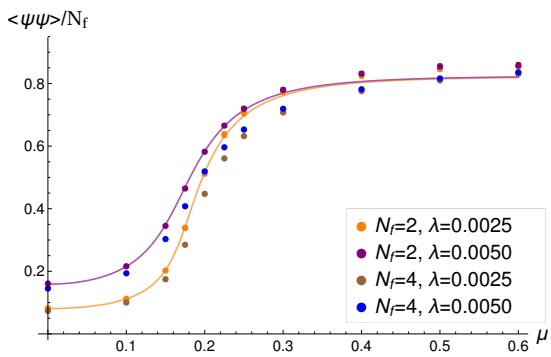

Figure 10.7.: The flavor dependence of the flavor-normalized diquark condensate.

Lastly, we measured the correlation functions for the four channels from section {8} in dependence of the chemical potential and extracted the according particle masses. We were not able to extract the masses of the anti-diquarks from channel 3 and 4 from the double-cosh fits (8.3.10) as their contribution becomes suppressed with increasing chemical potential according to the factor of $e^{-a\mu}$ and mixes with higher excitations. To have good statistics, we generally used $N_q = 16$ point sources randomly distributed over the $t = 0$ timeslice. In the case that this still was not enough, we increased to $N_q = 32$ or even $N_q = 48$ point sources. We will now present the results for both values of the diquark source in parallel and later compare them to each other. We start with an overview of the four channels with masses extracted from single-cosh fits in figure (10.8), here we only show the total error for better visibility.

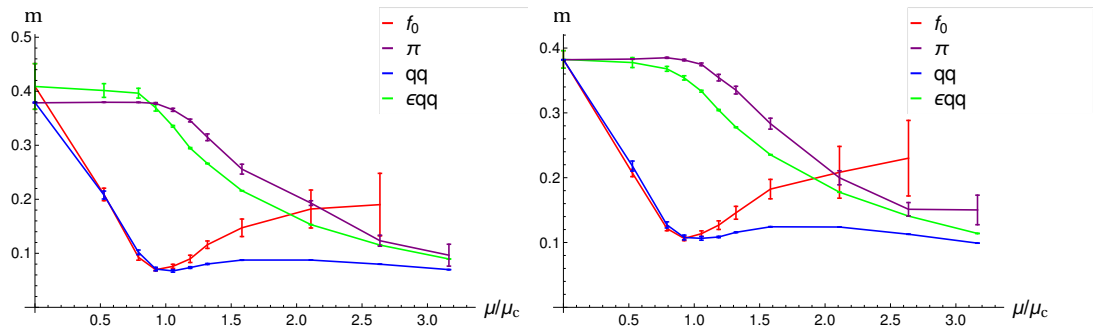

Figure 10.8.: An overview of the masses of the four channels in dependence of the chemical potential for $\lambda = 0.0025$ (left panel) and $\lambda = 0.0050$ (right panel).

We see that the masses of the pseudoscalar modes π and ϵqq behave very similar. They stay constant until the critical chemical potential is reached and then start to decrease. The masses of the scalar modes f_0 and qq are nearly degenerated until the mass of the f_0 meson begins to increase at the critical chemical potential. This can be understood by remembering table (7.1). If we suppose that the Goldstone modes induced from the chiral condensate rotate into the respective Goldstone mode induced from the diquark condensate, just like the condensate themselves do (see equation (9.2.1)), we can introduce the following two linear combinations of the correlators of our four channels [1]:

$$f_0/qq\colon\ \tfrac{1}{2}\left(\chi^T\tau_2\chi + \bar{\chi}\tau_2\bar{\chi}^T\right)\cos\alpha + \bar{\chi}\chi\sin\alpha$$

$$\pi/\epsilon qq\colon\ \bar{\chi}\epsilon\chi\cos\alpha + \tfrac{1}{2}\left(\chi^T\tau_2\epsilon\chi + \bar{\chi}\tau_2\epsilon\bar{\chi}^T\right)\sin\alpha$$

The angle α depends on the chemical potential and is given by solving equation (9.2.4). Note that we were able to apply a double-cosh-fit to the f_0/qq mode, where the lower mass was equal to the mass of the pure qq mode, so that we plot only the

higher mass in the following. In figure (10.9) we show the results along with the leading order chiral perturbation theory predictions of the P_s, $\tilde{Q}$ and $\tilde{Q}^\dagger$ mode from section {9.3}.

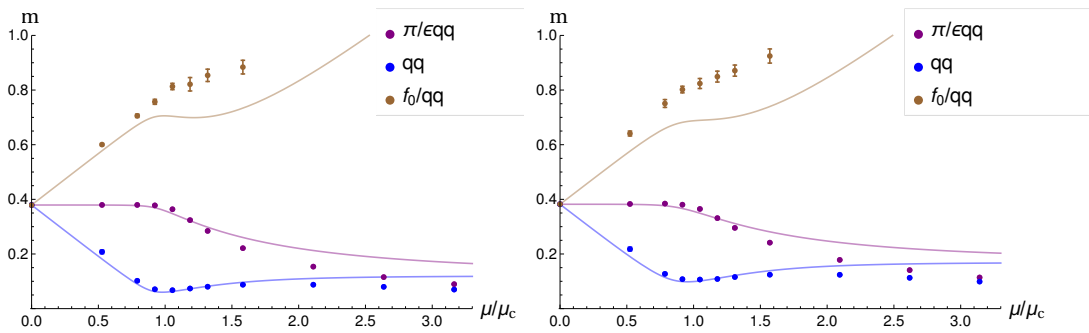

Figure 10.9.: The masses of the linear combinations and the scalar diquark mode in dependence of the chemical potential for $\lambda = 0.0025$ (left panel) and $\lambda = 0.0050$ (right panel) along with their respective leading order chiral perturbation theory prediction.

Before we discuss these results, let us show the comparisons between the results for $\lambda = 0.0025$ and $\lambda = 0.0050$ as they give a better insight at the separate channels, see figure (10.10) to (10.12). We find that the deviations from the leading order chiral perturbation theory predictions become larger for increasing chemical potential. It can be found that the term proportional to μ^2 in the effective Lagrangian, which gives the quark number density, also enters in the predictions of the Goldstone modes, thus the deviations of the quark number density at large μ in figure (10.4) is connected to the deviations of the Goldstone modes seen here [1]. The obtained masses for the scalar diquark match their predictions quite well until the deviations become significant. Same goes for the pseudoscalar diquark and the pion. The pion decrease is a little bit too late, which might be corresponding to the neglecting of disconnected diagrams. The combined $\pi/\epsilon qq$ mode shows a better agreement around the critical chemical potential as it here begins to be dominated by the contribution of the pseudoscalar diquark. The combined f_0/qq mode is very similar for both values of the diquark source, as also the prediction is, but for both λ from the critical chemical potential on it deviates hugely from the prediction. Again, this might be due to the neglecting of the disconnected diagrams for the purely f_0 mode which dominates the combined f_0/qq mode at large chemical potential.

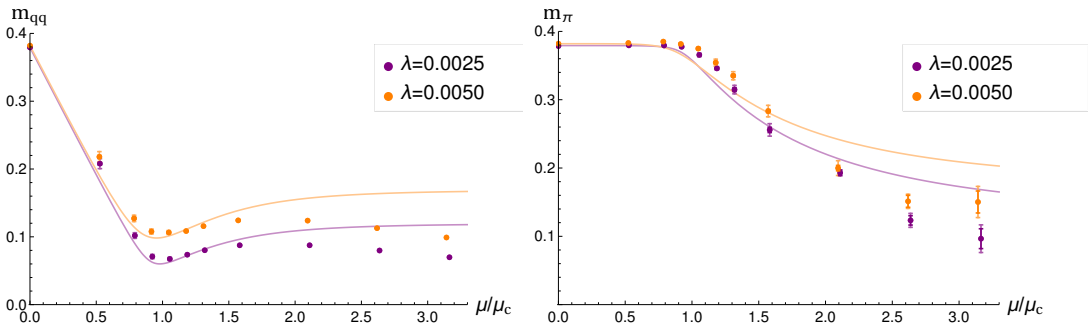

Figure 10.10.: The scalar diquark (left panel) and the pion (right panel) for both values of the diquark source.

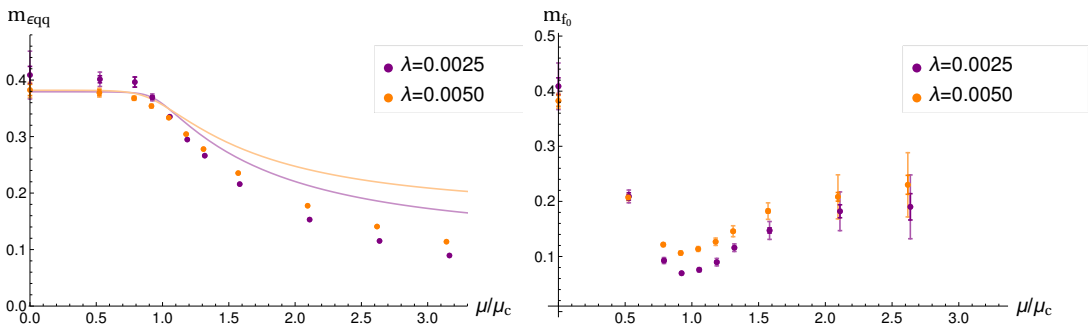

Figure 10.11.: The pseudoscalar diquark (left panel) and the scalar meson (right panel) for both values of the diquark source.

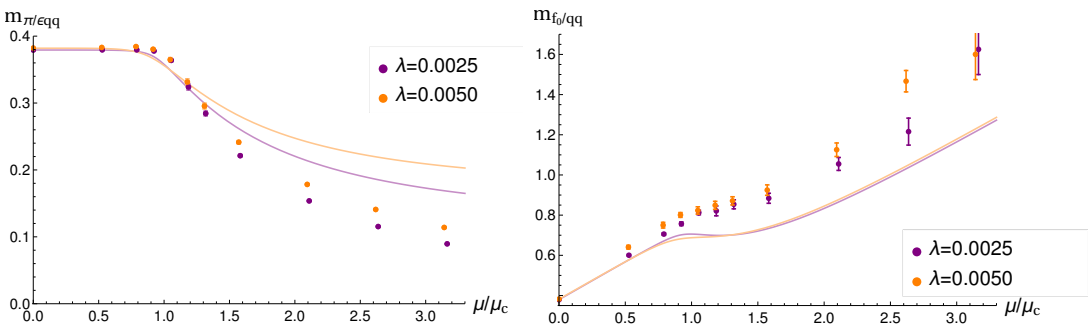

Figure 10.12.: The mass of the $\pi/\epsilon qq$ mode (left panel) and the mass of the f_0/qq mode (right panel) for both values of the diquark source.

10.3. A First Step for Leaving the Bulk Phase

After noticing the large value of the $\mathbb{Z}(2)$ monopole density for the used parameters of the last section, we wanted to run a simulation outside the artificial bulk phase. For this, we will now use the improved gauge action (2.4.11) as we saw in section {2.7} that it suppresses the $\mathbb{Z}(2)$ monopole density. Furthermore, we need to increase the inverse coupling β to further reduce the $\mathbb{Z}(2)$ monopole density and increase the lattice volume to suppress finite volume effects, as explained in section {2.7}. We decided to use a lattice volume of $16^3 \times 32$ and a quark mass of $m = 0.01$ to keep the computing time endurable. At this lattice size and quark mass, we found the inverse coupling of $\beta = 1.7$ to be a good compromise as for $\mu = 0$ the $\mathbb{Z}(2)$ monopole density is about 0.27 and the lattice volume is large enough so that the scalar meson and the pion are not degenerated due to finite size effects (see figure 10.13). Furthermore, the pion and the scalar meson, as well as the ρ meson and the a_1 meson, are not degenerate at this inverse coupling, meaning that chiral symmetry is broken. Hence at vanishing chemical potential we simulate inside the confined regime.

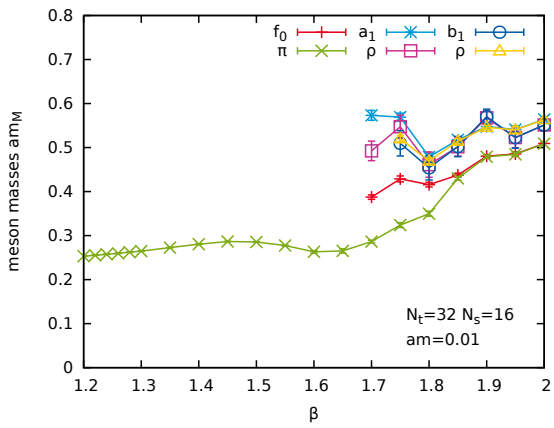

Figure 10.13.: The meson masses in dependence of the inverse coupling β [6].

This time, we used three values of the diquark source $\lambda = 0.001, 0.0025, 0.005$ to be able to do a meaningful extrapolation $\lambda \to 0$. See figure (10.14) and (10.15) for the resulting flavor-normalized condensates and quark number density.

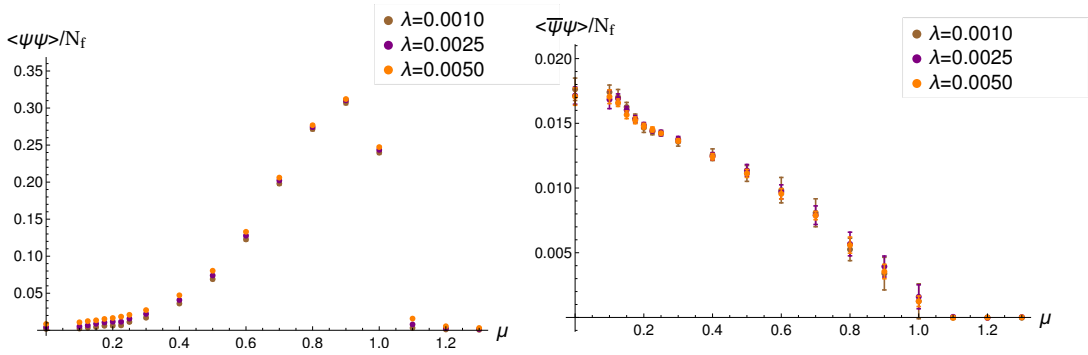

Figure 10.14.: The diquark condensate (left panel) and the chiral condensate (right panel).

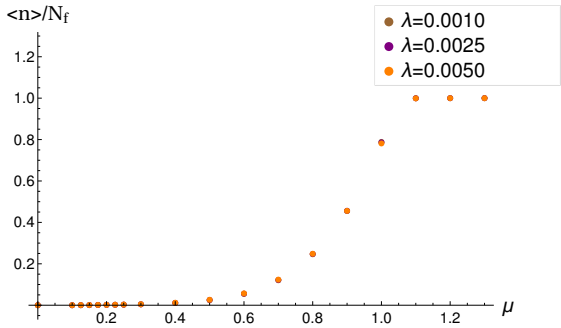

Figure 10.15.: The quark number density.

First, notice that the quark number density saturates at $\mu = 1.1$. Saturation is a lattice artifact, here the maximal number of quarks possible on the lattice is reached, given by $n_s = 2N_cN_fV$. Due to our normalization factor of the quark number density, it saturates at one, see equation (6.3.2). In the continuum there is no limit on the rise of the quark number density with the chemical potential. Thus, starting from the inflection point of the lattice quark number density, the physical behaviour of the lattice system is greatly disturbed and simulations in this regime are not meaningful. This explains the rapid fall of the diquark condensate, starting at $\mu = 1.0$. Notice the strange decrease of the chiral condensate, starting around $\mu = 0.3$, which we expect to be due to a UV-divergent contribution to the chiral condensate. Remember, a larger inverse coupling effects a smaller lattice spacing, that is why we did not see this effect in the simulations of the previous section at a smaller value of β. Hence we now need to investigate a renormalized chiral condensate without the UV-divergent contribution. It has been shown in [35] that renormalization can be achieved with the help of the chiral susceptibility. The chiral condensate and the chiral susceptibility are expected to behave like

$$\langle\bar{\psi}\psi\rangle_{m_q} = \langle\bar{\psi}\psi\rangle_0 + c_2 m_q + \frac{c_{UV}}{a^2} m_q + O(m_q^3) \ , \tag{10.3.1}$$

$$\chi_{m_q} = c_2 + \frac{c_{UV}}{a^2} + O(m_q^2) \ . \tag{10.3.2}$$

Notice that both quantities also contain an additional constant c_2, next to the UV-divergent contribution with constant c_{UV}. Both constants can be removed from the chiral condensate by defining the *subtracted chiral condensate*

$$\Sigma = \langle\bar{\psi}\psi\rangle_{m_q} - m_q \chi_{m_q} \ . \tag{10.3.3}$$

The susceptibility splits up in a connected and a disconnected contribution, where it has been found that the UV-divergent contribution mainly belongs to the connected part [35]. Thus, here we only calculate the connected chiral susceptibility, given by [6]

$$\chi^{con} = \frac{1}{V}\frac{N_f}{4} \ \mathrm{tr}\left(D^{-2}\right) \ , \tag{10.3.4}$$

and investigate the *connected susceptibility subtraction*

$$\Sigma^{con} = \langle\bar{\psi}\psi\rangle - m\chi^{con}. \tag{10.3.5}$$

Notice that in this initial study we neglect a possible explicit dependence of the connected chiral susceptibility on the diquark source λ. It only depends on λ through the used gauge configurations. In figure (10.16) we show the results for the diquark source of $\lambda = 0.005$ over the whole range of the chemical potential. Notice the large fluctuations in the chiral susceptibility due to the double inversion of the Dirac matrix in its calculation. Starting from $\mu > 0.2$, the chiral susceptibility is very close to the chiral condensate, leading to a renormalized condensate consistent with zero. For $\mu < 0.2$, we expected to see the decrease of the chiral condensate according to chiral perturbation theory predictions which can not be seen really good in this results.

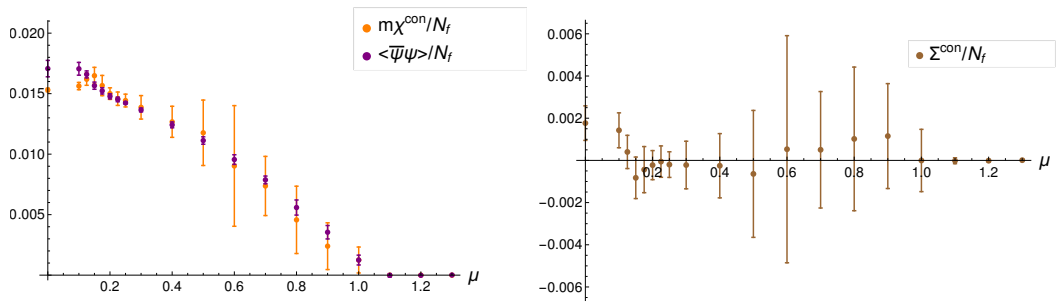

Figure 10.16.: The chiral condensate and mass times the connected chiral susceptibility (left panel) and the resulting renormalized chiral condensate (right panel) for $\lambda = 0.005$.

For further investigation, we measured the chiral susceptibility for all three values of the diquark source up to $\mu = 0.3$ to check its implicit dependence on λ and exploring if the expected behaviour of the renormalized condensate in the $\lambda \to 0$ limit can be seen. The results are shown in figures (10.17) to (10.19), where we also show the condensates and the quark number density for this limited range of the chemical potential. We only include the linear extrapolation to $\lambda = 0$ for the diquark condensate as for the other observables it is consistent with the result for $\lambda = 0.001$.

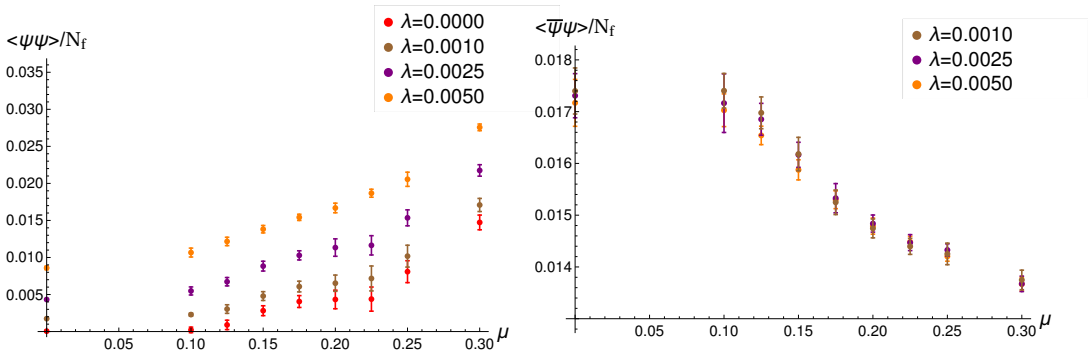

Figure 10.17.: The diquark condensate (left panel) and the chiral condensate (right panel).

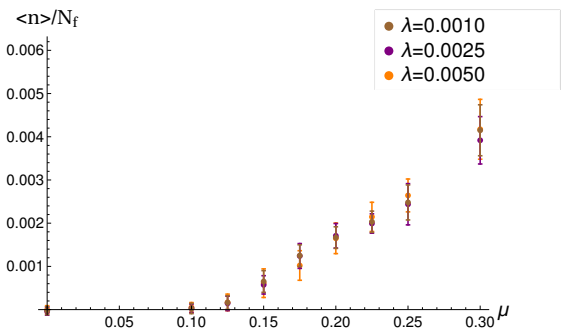

Figure 10.18.: The quark number density.

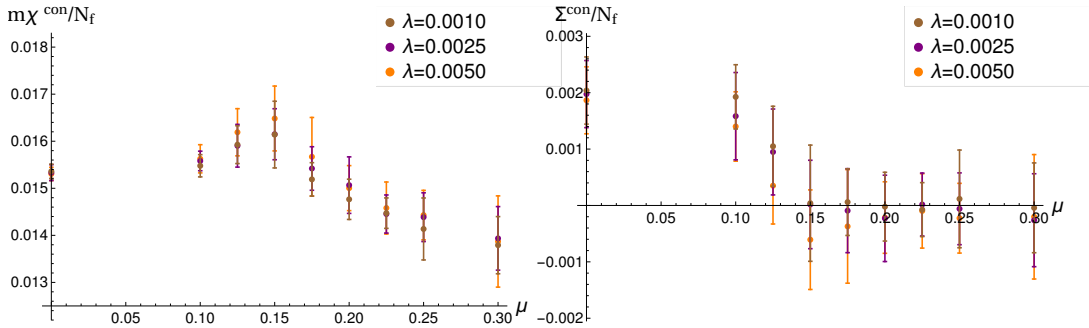

Figure 10.19.: Mass times the connected chiral susceptibility (left panel) and the renormalized chiral condensate (right panel).

In figure (10.20) we combine the $\lambda = 0$ results for the renormalized chiral condensate, the diquark condensate and the quark number density. Note that we have joined the points by lines for a better visualization of the data, these are no fitting curves.

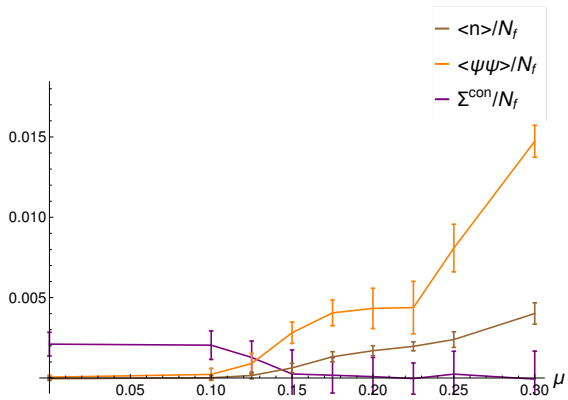

Figure 10.20.: The results for the $\lambda \to 0$ extrapolated diquark condensate, renormalized chiral condensate and quark number density.

The quark number density shows the expected rise at some critical value of the chemical potential μ_c. We still find an unexpected decrease of the renormalized chiral condensate which does not match to the chiral perturbation theory prediction. This might be due to the bump of the chiral susceptibility around $\mu = 0.15$, which we suggest to come from a contribution of the singular part of the scaling function. In general, the scaling behaviour of the chiral susceptibility at the phase transition due to the singular part of the scaling function is given by $\chi \sim |z|^{\gamma}$ with the reduced chemical potential $z = (\mu - \mu_c)/\mu_c$ and the critical exponent γ, resulting in a peak around the critical chemical potential μ_c. Note that it has been seen that the singular part of the scaling function only contributes to the disconnected part of the chiral susceptibility at $\mu = 0$ for the chiral transition [6]. From this scaling considerations

it follows that the peak height should increase when the diquark source λ is reduced. Due to the large errorbars, we can neither refute nor confirm this, which might also be due to the neglecting of the explicit dependence on λ. In a finite volume the peak height of the chiral susceptibility at a phase transition is restricted by a spatial volume dependent factor. Thus, for smaller spatial volumes the observed bump of the chiral susceptibility should vanish, if this bump really comes from the singular part of the scaling function. In figure (10.21) the results for the chiral susceptibility and the chiral condensate are shown for different spatial lattice sizes N_s, where again points have been joined for a better visualisation. The vanishing of the bump in the chiral susceptibility is visible, confirming our suggestion.

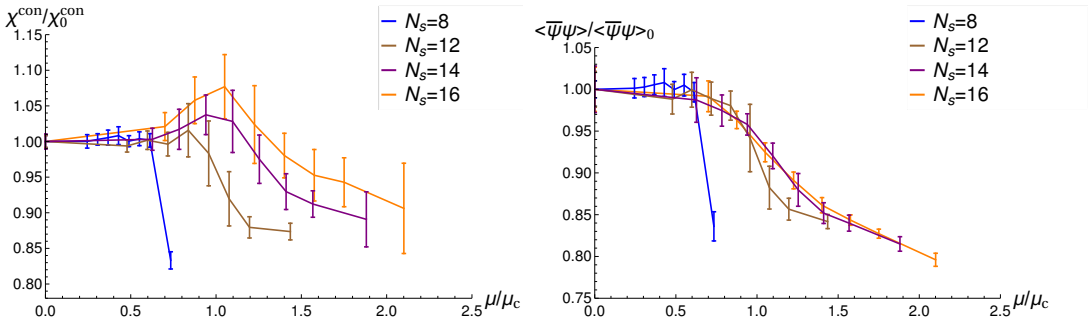

Figure 10.21.: Spatial volume dependence of the connected chiral susceptibility (left panel) and the chiral condensate (right panel). The value of μ_c for rescaling the x-axis was determined by measuring the pion correlator at $\mu = 0$ and extracting the pion mass: $\mu_c = \frac{m_\pi}{2}$.

At $N_s = 8$ the chiral susceptibility sharply drops already before the critical chemical potential is reached, which we think is due to large volume effects at this small spatial volume. Before we discuss the behavior of the chiral condensate in dependence of the spatial volume, we stress the decrease of the pion mass with increasing spatial volume, see table (10.3).

N_s	8	12	14	16
m_π	0.817(32)(45)	0.418(28)(35)	0.319(10)(11)	0.2856(51)(61)

Table 10.3.: The pion mass in dependence of the spatial lattice size N_s.

Generally, the smearing of the sharpness of a phase transition is driven by a Boltzmann factor, which in this case is given by

$$\exp\left(\frac{m_\pi - 2\mu}{T}\right) = \exp\left(\frac{m_\pi}{T}\left(1 - \frac{\mu}{\mu_c}\right)\right) , \tag{10.3.6}$$

where $(1 - \mu/\mu_c)$ is the distance from the transition point and the temperature

T is fixed due to the fixed time extend N_t. Therefore, the ratio m_π/T governs the sharpness of the phase transition so that for increasing pion mass the phase transition becomes sharper. Again, at $N_s = 8$ large volume effects are visible as the chiral condensate sharply drops already before the critical chemical potential is reached. For $N_s = 14$ and $N_s = 16$ the chiral condensate is nearly the same due to the small difference in the pion mass for these two spatial volumes. As the pion mass for $N_s = 12$ is larger than at $N_s = 14$ and $N_s = 16$, the decrease of the chiral condensate around the critical chemical potential is sharper. We think that the ratio m_π/T also influences the peak position of the chiral susceptibility which moves to larger values of μ/μ_c for larger spatial volumes, as seen in figure (10.21). From this observations, we conclude that the connected part of the chiral susceptibility can not be used to renormalize the chiral condensate at non-vanishing chemical potential. For this, different methods have to be employed. Here, we will investigate a simple model of the UV-divergent contribution in equation (10.3.2) to obtain the renormalized chiral condensate. The chiral condensate is expected to be constant until the critical chemical potential is reached, thus we also model the UV-divergent contribution by a constant c_m in this interval which is given by the value of connected chiral susceptibility at vanishing chemical potential. From figure (10.22) we can see that both, the chiral condensate and the connected chiral susceptibility, become zero at $\mu_1 = 1.05$.

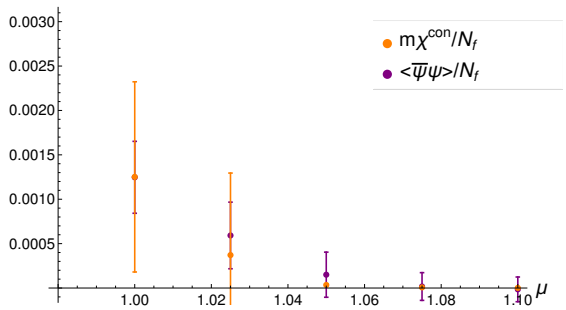

Figure 10.22.: The connected chiral susceptibility and the chiral condensate.

Consequently, we will set our model equal to zero for $\mu \geq \mu_1$. For the interval $\mu_c < \mu < \mu_1$ we employ the simplest case of a straight line. Hence, our model of the UV-divergent contribution is given by equation (10.3.7) and shown in figure (10.23).

$$\left(\frac{c_{UV}}{a^2} m_q\right)_{\text{model}}(\mu) = \begin{cases} c_m & \mu \leq \mu_c \\ c_m \left(1 - \frac{\mu - \mu_c}{\mu_1 - \mu_c}\right) & \mu_c \leq \mu \leq \mu_1 \\ 0 & \mu_1 \leq \mu \end{cases} \tag{10.3.7}$$

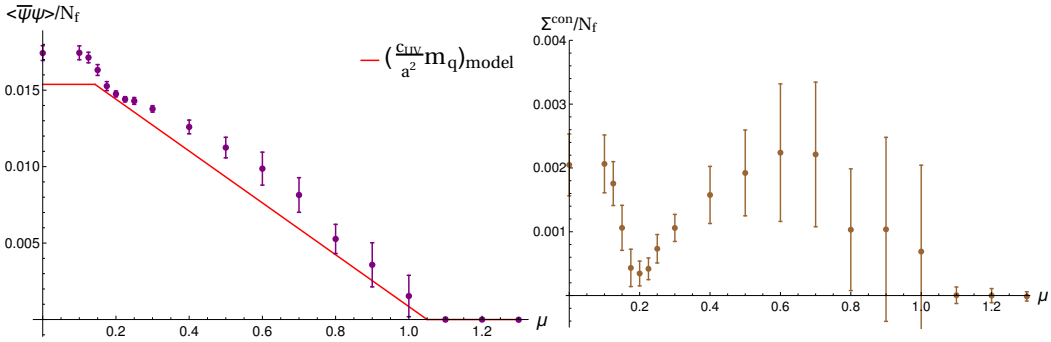

Figure 10.23.: The model of the UV-divergent contribution (left panel) and the resulting renormalized chiral condensate (right panel).

We see that the renormalized chiral condensate decreases already before μ_c, which is believed to be due to the same reasonings as for the bare chiral condensate, explained earlier. Furthermore, a huge bump in the range of $0.25 < \mu < 1.0$ is visible. It is yet unclear if this bump is an artifact or physically meaningful. We will refer to a physical suggestion in the following after studying the diquark condensate. Closing, due to the bump and the small m_π/T ratio at this lattice parameters, we are still not able to fit the prediction of leading order chiral perturbation theory to our modelled renormalized chiral condensate. For an improvement of this situation, a better model could be developed and the time extent of the lattice could be increased, where the latter is computational costly.

Now, instead of doing a combined fit to the chiral perturbation theory predictions, we only fit the diquark condensate in the interval $\mu \in [0.125, 0.225]$ to its $\lambda = 0$ prediction, given by $\langle\psi\psi\rangle = \langle\bar{\psi}\psi\rangle_0 \sqrt{1-(\mu_c/\mu)^4}$ for $\mu > \mu_c$ and zero otherwise. The result is combined in figure (10.24). The critical chemical potential obtained from this fit is consistent with the critical chemical potential obtained from measuring the pion mass: $\mu_c = 0.1428(26)(31)$. The fitting value of $\langle\bar{\psi}\psi\rangle_0$ is not consistent with the value of the renormalized chiral condensate at $\mu = 0$, given by $\langle\bar{\psi}\psi\rangle_0 = 0.00204(48)$. Notice also that the large increase of the diquark condensate, beginning at $\mu = 0.225$, is a huge deviation from the chiral perturbation theory prediction. This has also been seen in [36] and argued to be due to a BEC-BCS crossover transition. Coming back to the observed bump in our modeled renormalized chiral condensate, one could suggest that this bump is also due to the BEC-BCS crossover transition. To clarify this, more investigations are needed as the used model might just be too simple.

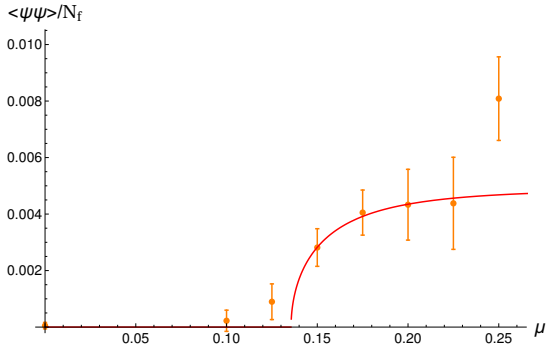

$$\langle\bar{\psi}\psi\rangle_0 = 0.00490(65)$$
$$\mu_c = 0.1356(86)$$
$$\chi^2/\mathrm{DOF} = 0.48$$

Figure 10.24.: The resulting fit of the $\lambda = 0$ diquark condensate to the chiral perturbation theory prediction.

The obtained results for the Polyakov loop and the $\mathbb{Z}(2)$ monopole density are shown in figure (10.25).

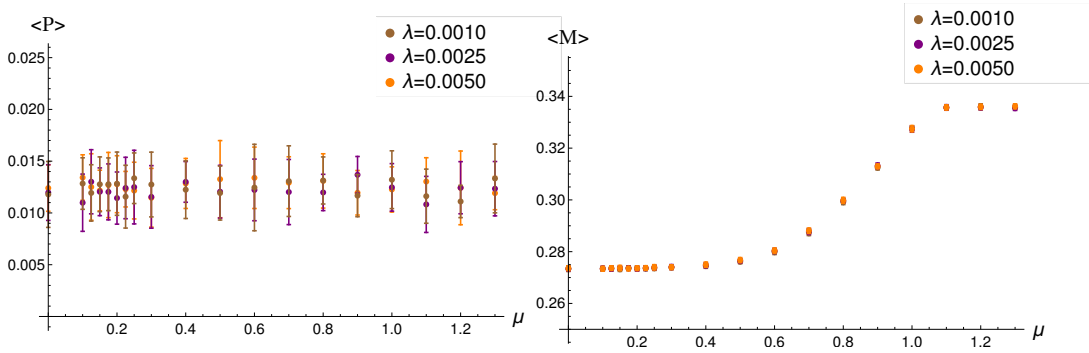

Figure 10.25.: The Polyakov loop (left panel) and the $\mathbb{Z}(2)$ monopole density (right panel).

The $\mathbb{Z}(2)$ monopole density increases with μ and saturates at $\mu = 1.1$, as the quark number density. We suppose that in the saturated regime the system corresponds to that obtained by pure gauge theory as there are no fermionic degrees of freedom any more. Thus, the difference in the $\mathbb{Z}(2)$ monopole density between $\mu = 1.1 - 1.3$ and $\mu = 0$ is the same as between pure gauge theory and including dynamical fermions at $\mu = 0$, which we confirmed with the data of figure (2.3). Again, the Polyakov loop is constant within the errorbars over the whole range of μ. In comparison, it has been seen in simulations with Wilson fermions [37] and also in an effective Polyakov loop model study [38], that the Polyakov loop has a peak at the reflection point of the quark number density. As the $\mathbb{Z}(2)$ monopole does, we expected the Polyakov loop to show quenching effects, too, but these are not visible. To obtain more insight, we also measured the local Polyakov loop distribution. We show the distribution for three values of the chemical potential, but it is consistent at all values of μ, see figure

(10.26), and does not make any quenching effects visible either. Consequently, we measured the value of the Polyakov loop in pure gauge theory $\langle P \rangle = 0.012896(29)$ which is consistent within the errorbars with our results in the unquenched case. We conclude that finite volume effects overshadow the difference of the quenched and unquenched cases.

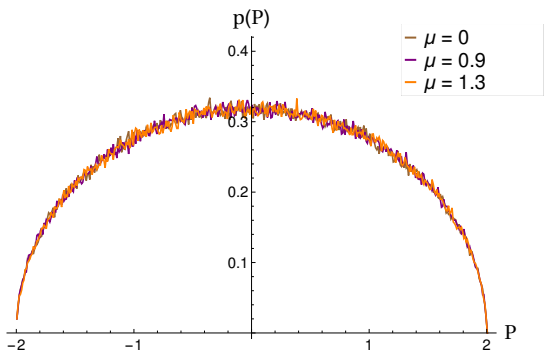

Figure 10.26.: The local Polyakov loop distribution.

We measured the correlation functions for the four channels from section {8} in dependence of the chemical potential. Let us first show the results for the three values of the diquark source in parallel and at the end illustrate the λ-dependence. When we tried to extract the masses of the meson channels 1 and 2, we found that an oscillatory contribution, which becomes large for $\mu > \mu_c$, pollutes the correlation functions. Thus, we employed a double-cosh fit, where one cosh is multiplied by $(-1)^t$ to filter out the oscillation. See figure (10.27) for an overview of the extracted masses of the four channels, where we joined points and showed only the total error for better visualisation. Notice the large errors for $\mu > \mu_c$ in the meson channels due to the oscillatory contribution.
We find a quite different behaviour for the spectrum than in section {10.2}. Only the scalar diquark behaves as seen before. The pseudoscalar diquark mass now begins to decrease with increasing chemical potential, becoming degenerated with the scalar diquark mass at large μ. The pion mass is still constant until the critical chemical potential is reached, but then begins to increase. The scalar meson still first decreases with increasing chemical potential, but is not degenerated with the scalar diquark in this regime any more, and then starts to increase. The non-degeneracy of the scalar meson and the scalar diquark for $\mu < \mu_c$ might be due to the non-degeneracy of the pion and the scalar meson at vanishing chemical potential. Still, the slope of the scalar meson and the scalar diquark seem very similar for $\mu < \mu_c$. One could suggest, that the scalar meson becomes degenerate with the pion at large chemical potential. Due to this different behaviour, the introduced combined modes from section {10.2} do not give any meaningful results. For small chemical potentials we can still obtain the mass of the $\tilde{Q}^\dagger$ mode by fitting the correlation function of the purely anti-diquark state $\bar{q}\bar{q}$ to equation (8.3.4).

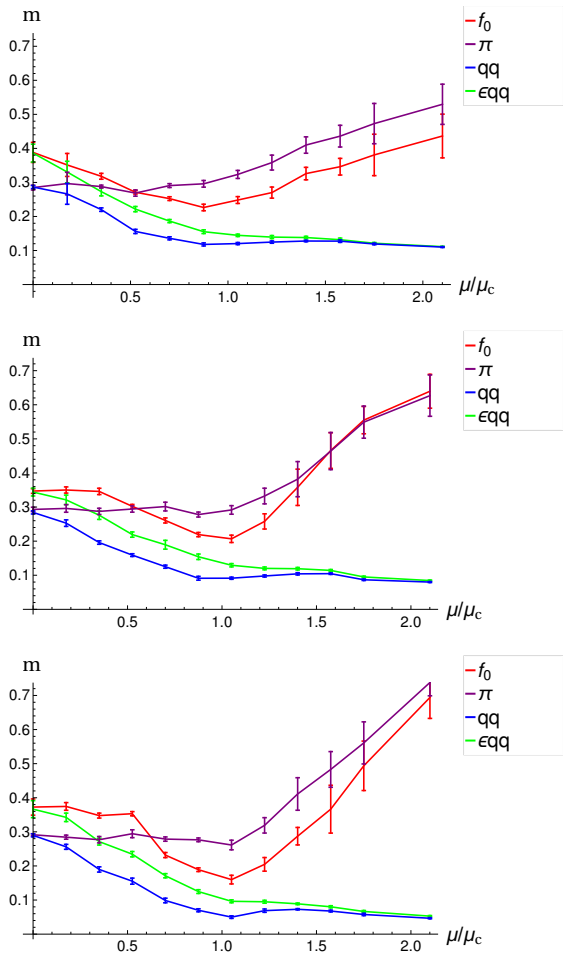

Figure 10.27.: The extracted masses of the meson modes and diquark modes in dependence of the chemical potential for $\lambda = 0.0050$ (top), $\lambda = 0.0025$ (middle) and $\lambda = 0.0010$ (bottom).

We compare the scalar diquark, the scalar anti-diquark and the pion to the leading order chiral perturbation theory predictions, see figure (10.28).

Note that here we compare the pion to the P_A mode, instead of the P_S mode. Remember that the pattern of symmetry breaking on the lattice corresponds to the pattern of symmetry breaking of any color QCD with quarks in the adjoint representation. Studying leading order chiral perturbation theory for two-color QCD with quarks in the fundamental representation, one will find that the P_A mode and the P_S mode interchange [29]. Thus, a naive suggestion would be that our lattice spacing a is now already small enough to be able to observe the continuum pattern of symmetry breaking, instead of the lattice pattern of symmetry breaking. This suggestion needs further inspection.

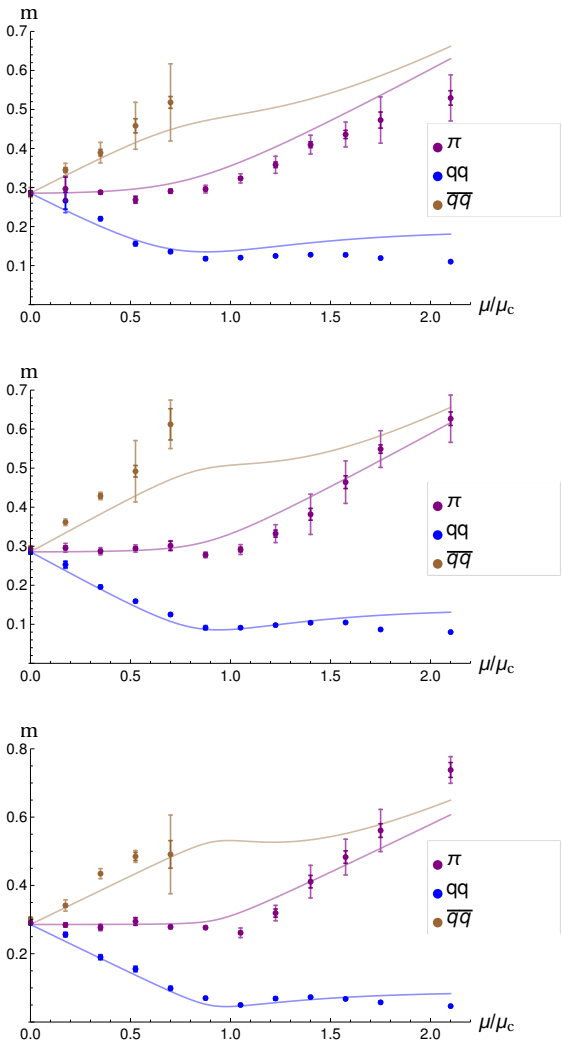

Figure 10.28.: Comparing the scalar diquark, the scalar anti-diquark and the pion to their leading order chiral perturbation theory predictions for $\lambda = 0.0050$ (top), $\lambda = 0.0025$ (middle) and $\lambda = 0.0010$ (bottom).

Finally, let us illustrate the dependence on the diquark source of the measured modes, see figures (10.29) to (10.31).

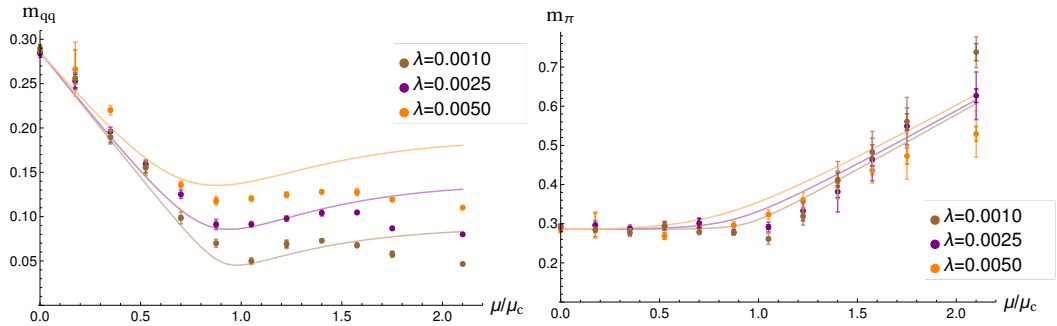

Figure 10.29.: The scalar diquark (left panel) and the pion (right panel) for three values of the diquark source.

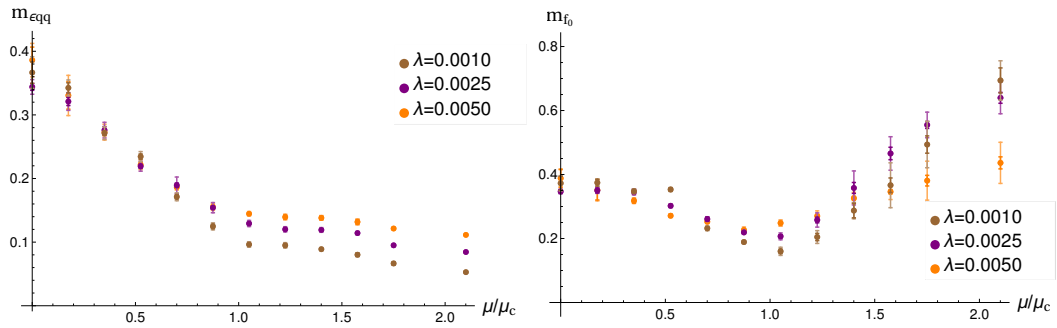

Figure 10.30.: The pseudoscalar diquark (left panel) and the scalar meson (right panel) for three values of the diquark source.

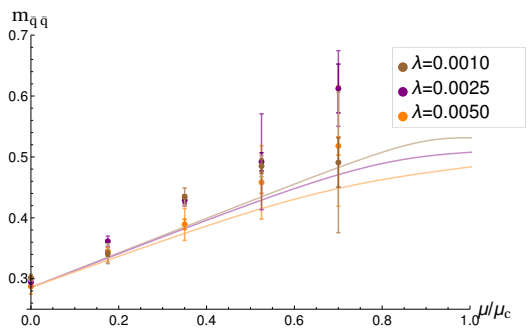

Figure 10.31.: The scalar anti-diquark for three values of the diquark source.

11. Conclusion and Outlook

In this work, an introduction into lattice Monte Carlo simulations of QCD was given, which are able to give insight into the confined regime, where perturbative methods are not applicable. It has been shown how the fundamental degrees of freedom of QCD, quarks and gluons, are implemented on the lattice and the used algorithm to calculate expectation values has been introduced. We focused on simulations at non-vanishing baryon chemical potential. Here, lattice QCD suffers from the sign-problem and thus we decided to simulate two-color QCD, where the fermion determinant is real at non-vanishing chemical potential due to the pseudo-reality of the generators of $SU(2)$ in the fundamental representation. Two-color QCD exhibits the properties of confinement and diquark condensation and is thus treated as a QCD-like theory, which should give insight into the phase diagram of full three-color QCD. We were able to successfully introduce a diquark source term into the lattice fermion action, which allows for a study of the spontaneous breaking of baryon number conservation at non-vanishing chemical potential.
First, we tried to reduce the simulated number of quark flavors by using real pseudofermions in the HMC algorithm. A comparison with results using rooted-fermions showed a huge difference. We found that a reduction of quark flavors by using real pseudofermions needs further adjustments of the HMC algorithm, which are computationally costly and hence we decided to use two flavors of rooted staggered fermions.
A simulation at finite chemical potential was done on a medium size lattice $12^3 \times 24$ at a relatively small inverse coupling $\beta = 1.5$. We found a good agreement of our results with predictions from leading order chiral perturbation theory. The prediction for the critical chemical potential of diquark condensation $\mu_c = \frac{m_\pi}{2}$ was confirmed. The Goldstone meson spectrum was studied and found to generally agree with leading order chiral perturbation theory predictions, but showed huge deviations at large chemical potential. The measurement of the $\mathbb{Z}(2)$ monopole density revealed that we simulated deep inside the artificial bulk phase, where lattice artifacts have a huge influence on physical processes. Hence, we decided to run another simulation as far outside the bulk phase as possible.
For this, we employed an improved gauge action, which suppresses the bulk phase and increased our inverse coupling to $\beta = 1.7$, leading to a $\mathbb{Z}(2)$ monopole density of about 0.27. Due to the increased inverse coupling, we had to increase the lattice size to $16^3 \times 32$ to handle finite size effects. In this simulation, we observed the occurrence of saturation, where the maximum number of fermions on the lattice is reached. We found evidence that in the saturated regime the system behaves like in its corresponding pure gauge theory. We were able to fit the leading order chiral per-

turbation theory prediction to our obtained diquark condensate, but here it showed larger deviations at large chemical potential, which might be due to a BEC-BCS crossover transition. The chiral condensate suffers from UV-divergent contributions due to the smaller lattice spacing. Thus, we attempted a renormalization with the connected chiral susceptibility, which exhibits the same UV-divergent contribution. Then, it was found that the connected chiral susceptibility contains a contribution from the singular part of the scaling function around the onset of diquark condensation and hence we decided to use a simple model of the UV-divergent contribution for renormalization. The Goldstone spectrum was found to be different to the previous simulation. Only the scalar diquark showed its usual behaviour. The most important change was that the pion mass started to increase for $\mu > \mu_c$, which led to the suggestion that we observed the continuum pattern of symmetry breaking.
In conclusion, this work shows that a simulation outside the bulk phase requires quite more effort. The computational cost increases as the lattice volume has to be increased due to the larger inverse couplings, leading also to the need of renormalization as UV-divergent contributions become larger. We found that the usual method of additive renormalization by subtracting the connected chiral susceptibility does not work at finite chemical potential. We employed a simple model for the UV-divergent contributions, which needs more investigations and maybe improvements. A next step would be to investigate the chiral condensate for free fermions ($U_\mu = \mathbb{I}$), which should exhibit the same UV-divergent contribution and thus might give insight into the accuracy of our model. Furthermore, the spectroscopy results of the meson modes need further investigations as disconnected diagrams were omitted, which could be responsible for some of the deviations of the meson masses from leading order chiral perturbation theory. Moreover, noisy sources could improve the extraction of masses from the correlation functions, leading to smaller statistical and systematic errors.

A. Appendix

A.1. The Euclidean γ-Matrices

The Euclidean anti-commutation relations given by [5]

$$\{\gamma_\mu, \gamma_\nu\} = 2\ \delta_{\mu\nu}\ \mathbb{I}_4 \tag{A.1.1}$$

can be obtained from the Minkowski anti-commutation relations ($\{\gamma_\mu^M, \gamma_\nu^M\} = 2\ g_{\mu\nu}\ \mathbb{I}_4$, with $g_{\mu\nu} = (1, -1, -1, -1)$ as metric) by setting

$$\gamma_i = -i\gamma_i^M\ ;\ i = 1, 2, 3, \quad \gamma_4 = \gamma_0^M\ . \tag{A.1.2}$$

The γ-matrices obey

$$\gamma_\mu = \gamma_\mu^\dagger = \gamma_\mu^{-1}\ . \tag{A.1.3}$$

In addition, one defines a fifth γ matrix as the product

$$\gamma_5 = \prod_{i=1}^{4}\ \gamma_i\ . \tag{A.1.4}$$

It anti-commutes with all other γ-matrices and obeys $\gamma_5^2 = 1$. An explicit representation of the γ-matrices is given by the so-called *chiral representation* [5]

$$\gamma_{1,2,3} = \begin{pmatrix} 0 & -i\sigma_{1,2,3} \\ i\sigma_{1,2,3} & 0 \end{pmatrix}\ ,\quad \gamma_4 = \begin{pmatrix} 0 & \mathbb{I}_2 \\ \mathbb{I}_2 & 0 \end{pmatrix}\ ,\quad \gamma_5 = \begin{pmatrix} \mathbb{I}_2 & 0 \\ 0 & -\mathbb{I}_2 \end{pmatrix}\ . \tag{A.1.5}$$

A.2. Continuum Limit of the Naive Fermion Action

Here, we calculate the continuum limit of the naive fermion action (2.1.9). It is obvious that the mass term approaches the continuum mass term and thus we only show the calculation for the derivative term explicitly. To calculate the continuum limit of the derivative term, one uses Taylor expansions for the fields like

$$\psi(n \pm \hat{\mu}) = \psi(n) \pm a\ \psi'(n) + \cdots\ , \tag{A.2.1}$$

$$U_{\pm\mu}(n) = \mathbb{I} \pm ia\ A_\mu\left(n \pm \frac{\hat{\mu}}{2}\right) + \cdots \tag{A.2.2}$$

$$= \mathbb{I} \pm ia\ \left(A_\mu(n) \pm \frac{a}{2}A'_\mu(n) + \cdots\right) + \cdots\ . \tag{A.2.3}$$

Plugging the Taylor expansions into the μ-direction of the derivative term, one obtains

$$\begin{aligned}
\bar{\psi}\not{D}_\mu\psi =& \frac{1}{2a}\bar{\psi}(n)\ \gamma_\mu\left[U_\mu(n)\psi(n+\hat{\mu}) - U_{-\mu}(n)\psi(n-\hat{\mu})\right] \\
=& \frac{1}{2a}\bar{\psi}(n)\ \gamma_\mu\left[\left(\mathbb{I} + ia\ A_\mu\left(n+\frac{\hat{\mu}}{2}\right) + \cdots\right)\left(\psi(n) + a\ \psi'(n) + \cdots\right)\right. \\
& \left. - \left(\mathbb{I} - ia\ A_\mu\left(n-\frac{\hat{\mu}}{2}\right) + \cdots\right)\left(\psi(n) - a\ \psi'(n) + \cdots\right)\right] \\
=& \bar{\psi}(n)\ \gamma_\mu\left(\partial_\mu + \frac{a^2}{6}\partial_\mu^3 + \cdots\right)\ \psi(n) \\
& + i\ \bar{\psi}(n)\ \gamma_\mu\left[A_\mu(n) + \frac{a^2}{2}\left(\frac{1}{4}\partial_\mu^2 A_\mu(n) + (\partial_\mu A_\mu(n))\,\partial_\mu + A_\mu(n)\partial_\mu^2 + \cdots\right)\right]\psi(n).
\end{aligned} \tag{A.2.4}$$

Taking the continuum limit, it follows that

$$\lim_{a\to 0}\bar{\psi}\not{D}_\mu\psi = \bar{\psi}(x)\left(\gamma_\mu\partial_\mu + i\ \gamma_\mu A_\mu(x)\right)\psi(x) + O(a^2)\ . \tag{A.2.5}$$

Therefore, one recovers the form of the continuum action in the continuum limit and the discretization error of the naive fermion action starts at $O(a^2)$.

A.3. The traceless Anti-Hermitian Projection

A general formula for the projection of a 2×2 complex Matrix to its traceless anti-hermitian part can be achieved by a straight forward calculation of

$$A\Big|_{TA} = \frac{1}{2}\left(A - A^\dagger\right) - \frac{1}{4}\mathrm{tr}\left(A - A^\dagger\right)\ . \tag{A.3.1}$$

Starting with the Matrix A, parametrised as

$$A = \begin{pmatrix} a_{00} + ia_{01} & a_{10} + ia_{11} \\ a_{20} + ia_{21} & a_{30} + ia_{31} \end{pmatrix}\ , \tag{A.3.2}$$

we calculate $A - A^\dagger$, given by

$$A - A^\dagger = \begin{pmatrix} 2ia_{01} & a_{10} - a_{20} + i(a_{11} + a_{21}) \\ -(a_{10} + a_{20}) + i(a_{11} + a_{21}) & 2ia_{31} \end{pmatrix} \tag{A.3.3}$$

and hence we have $\mathrm{tr}\left(A - A^\dagger\right) = 2i(a_{01} + a_{31})$. Plugging $A - A^\dagger$ and its trace into equation (A.3.1), we arrive at

$$A\Big|_{TA} = \begin{pmatrix} i\frac{1}{2}(a_{01} - a_{31}) & \frac{1}{2}(a_{10} - a_{20}) + i\frac{1}{2}(a_{11} + a_{21}) \\ -\frac{1}{2}(a_{10} - a_{20}) + i\frac{1}{2}(a_{11} + a_{21}) & -i\frac{1}{2}(a_{01} - a_{31}) \end{pmatrix} . \tag{A.3.4}$$

This can be written in the quaternion representation for SU(2) group elements [6] with a four vector $x = (x_0, x_1, x_2, x_3)$, whose components are then given by

$$\begin{aligned} x_0 &= 0 \\ x_1 &= \frac{1}{2}(a_{11} + a_{21}) \\ x_2 &= \frac{1}{2}(a_{10} - a_{20}) \\ x_3 &= \frac{1}{2}(a_{01} - a_{31}) \ . \end{aligned} \tag{A.3.5}$$

A.4. Force Term of the Wilson Gauge Action

Here, we will show the force term calculation for the Wilson gauge action (2.4.6)

$$F_{G,\mu}(n)_{fg}\Big|_{TA} = U_\mu(n)_{fb} \frac{\partial S_G}{\partial U_\mu(n)_{gb}}\Big|_{TA} \ . \tag{A.4.1}$$

For simplicity, we here consider the equivalent form given by

$$F_{G,\mu}(n)\Big|_{TA} = \sum_{j=1}^{N_c^2-1} T_j \frac{\partial S_G}{\partial (iA_\mu^j(n))}\Big|_{TA} \ , \tag{A.4.2}$$

with T_j being the generators of the SU(N_c) group. We find the local contribution to the action from one particular link variable to be [5]

$$\begin{aligned} S_{loc.}[U_\mu(n)] &= -\frac{\beta}{N_c} \mathrm{Re}\ \mathrm{tr}\left[U_\mu(n) A_\mu(n)\right] \\ &= -\frac{\beta}{2N_c} \mathrm{tr}\left[U_\mu(n) A_\mu(n) + A_\mu(n)^\dagger U_\mu(n)^\dagger\right] \ , \end{aligned} \tag{A.4.3}$$

$$\begin{aligned} \text{with } A_\mu(n) = \sum_{\nu \neq \mu} \Big(& U_\nu(n+\hat{\mu})\ U_\mu^\dagger(n+\hat{\nu})\ U_\nu^\dagger(n) \\ & + U_\nu^\dagger(n+\hat{\mu}-\hat{\nu})\ U_\mu^\dagger(n-\hat{\nu})\ U_\nu(n-\hat{\nu}) \Big) \ . \end{aligned} \tag{A.4.4}$$

Hence, using the exponential representation of the link variables from equation (4.1.1), the derivative of the action is easily calculated and we obtain for the force term of the Wilson gauge action the following result

$$\begin{aligned} F_{G,\mu}(n) &= -\frac{\beta}{2N_c} \sum_{j=1}^{N_c^2-1} T_j \text{ tr} \left[\left(U_\mu(n) A_\mu(n) - A_\mu(n)^\dagger U_\mu(n)^\dagger \right) T_j \right] \\ &= -\frac{\beta}{2N_c} \left(U_\mu(n) A_\mu(n) - A_\mu(n)^\dagger U_\mu(n)^\dagger \right) \end{aligned} \tag{A.4.5}$$

$$\Rightarrow F_{G,\mu}(n)\Big|_{TA} = -\frac{\beta}{N_c} U_\mu(n) A_\mu(n)\Big|_{TA} . \tag{A.4.6}$$

A.5. Force Term of the Improved Gauge Action

To calculate the force term of the improved gauge action, we split it up in a sum of the plaquette contributions and the rectangle contributions. Dropping some constants, we obtain

$$S = -\frac{\beta}{N_c} \sum_{n\in\Lambda} \left[c_0 \sum_{\mu>\nu} \text{Re tr}(P_{\mu\nu}) + c_1 \sum_{\mu\neq\nu} \text{Re tr}(R_{\mu\nu}) \right] . \tag{A.5.1}$$

The constants c_0, c_1 can be read off from equation (2.4.11). The plaquette contributions correspond to the Wilson gauge action, with an additional factor of c_0, whose force we already calculated in appendix {A.4}. Thus, we focus on the rectangle contributions now. The calculation is completely analogue to the case of the Wilson gauge action, we only need to adjust the local contribution of a given link $A_\mu(n)$, which we now call $R_\mu(n)$. The link $U_\mu(n)$ contributes to rectangles at three different positions and two different orientations, each for all $\nu \neq \mu$, visualized in figure (A.1).

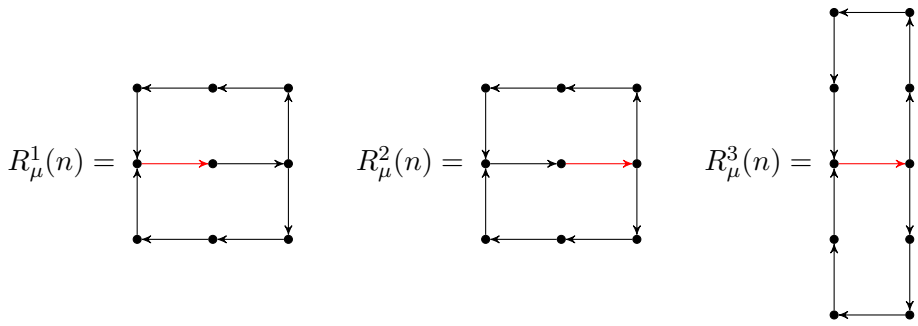

Figure A.1.: The local contribution of the link $U_\mu(n)$ (marked red).

In formulas we have

$$
\begin{aligned}
R^1_\mu(n) = \sum_{\mu\neq\nu} \Big(& U_\mu(n+\hat\mu)U_\nu(n+2\hat\mu)U_\mu(n+\hat\mu+\hat\nu)^\dagger U_\mu(n+\hat\nu)^\dagger U_\nu(n)^\dagger \\
& U_\mu(n+\hat\mu)U_\nu(n+2\hat\mu-\hat\nu)^\dagger U_\mu(n+\hat\mu-\hat\nu)^\dagger U_\mu(n-\hat\nu)^\dagger U_\nu(n-\hat\nu)\Big) \ , \\
R^2_\mu(n) = \sum_{\mu\neq\nu} \Big(& U_\nu(n+\hat\mu)U_\mu(n+\hat\nu)^\dagger U_\mu(n-\hat\mu+\hat\nu)^\dagger U_\nu(n-\hat\mu)^\dagger U_\mu(n-\hat\mu) \\
& U_\nu(n+\hat\mu-\hat\nu)^\dagger U_\mu(n-\hat\nu)^\dagger U_\mu(n-\hat\mu-\hat\nu)^\dagger U_\nu(n-\hat\mu-\hat\nu)U_\mu(n-\hat\mu)\Big) \ , \\
R^3_\mu(n) = \sum_{\mu\neq\nu} \Big(& U_\nu(n+\hat\mu)U_\nu(n+\hat\mu+\hat\nu)U_\mu(n+2\hat\nu)^\dagger U_\nu(n+\hat\nu)^\dagger U_\nu(n)^\dagger \\
& + U_\nu(n+\hat\mu-\hat\nu)^\dagger U_\nu(n+\hat\mu-2\hat\nu)^\dagger U_\mu(n-2\hat\nu)^\dagger U_\nu(n-2\hat\nu)U_\nu(n-\hat\nu)\Big) \ .
\end{aligned}
$$

Hence, we can state the final result for the contributions of the rectangles to the force term of the improved gauge action

$$
F_{R,\mu}(n)\Big|_{TA} = -\frac{c_1\beta}{N_c}\sum_{i=1}^{3} U_\mu(n)R^i_\mu(n)\Big|_{TA} \ . \tag{A.5.2}
$$

A.6. Force term of the Staggered Fermion Action

Here, we will show the calculation of the force term of the staggered fermion action (3.1.3)

$$
F_{F,\mu}(n)_{ef}\Big|_{TA} = U_\mu(n)_{ec}\frac{\partial S_F}{\partial U_\mu(n)_{fc}}\Big|_{TA} \ . \tag{A.6.1}
$$

Exploiting the relation [5]

$$
\frac{\partial M^{-1}}{\partial U} = -M^{-1}\,\frac{\partial M}{\partial U}\,M^{-1} \ , \tag{A.6.2}
$$

we can rewrite the force term as

$$
\begin{aligned}
F_{F,\mu}(n)_{ef} &= U_\mu(n)_{ec}\ \phi^\dagger_a\ \frac{\partial (DD^\dagger)^{-1}_{ab}}{\partial U_\mu(n)_{fc}}\ \phi_b \\
&= -U_\mu(n)_{ec}\ \phi^\dagger_a (DD^\dagger)^{-1}_{ah}\left(\frac{\partial D_{hm}}{\partial U_\mu(n)_{fc}}D^\dagger_{mn} + D_{hm}\frac{\partial D^\dagger_{mn}}{\partial U_\mu(n)_{fc}}\right)(DD^\dagger)^{-1}_{nb}\phi_b \\
&= -U_\mu(n)_{ec}\ \left((\chi\chi^\dagger)_{nh}D_{hm}\frac{\partial D^\dagger_{mn}}{\partial U_\mu(n)_{fc}} + D^\dagger_{mn}(\chi\chi^\dagger)_{nh}\frac{\partial D_{hm}}{\partial U_\mu(n)_{fc}}\right) \ ,
\end{aligned} \tag{A.6.3}
$$

where we have identified $\chi = (DD^\dagger)^{-1}\phi$. The χ fields can be calculated by solving the equivalent equation $(DD^\dagger)\chi = \phi$ with the method of conjugate gradients [39]. This has to be done for every force calculation during the HMC algorithm, making the algorithm computational costly. The derivative of the staggered Dirac operator (4.2.2) with respect to the link variables is easily calculated to

$$\frac{\partial D(k|l)_{hm}}{\partial U_\mu(n)_{fc}} = \frac{\eta_\mu(k)}{2a}\delta_{kn}\delta_{l,k+\hat{\mu}}\delta_{hf}\delta_{mc} = -\frac{\partial D(k|l)^\dagger_{hm}}{\partial U_\mu(n)_{fc}} \ . \tag{A.6.4}$$

Using this, we can calculate the two terms in the bracket

$$(\chi\chi^\dagger)_{nh} D_{hm} \frac{\partial D^\dagger_{mn}}{\partial U_\mu(n)_{fc}} = \frac{\eta_\mu(n)}{2a}\chi_c(n+\hat{\mu})\ (D^\dagger\chi)^\dagger_f(n) \ , \tag{A.6.5}$$

$$D^\dagger_{mn}(\chi\chi^\dagger)_{nh} \frac{\partial D_{hm}}{\partial U_\mu(n)_{fc}} = -\frac{\eta_\mu(n)}{2a}(D^\dagger\chi)_c(n+\hat{\mu})\ \chi^\dagger_f(n) \ , \tag{A.6.6}$$

giving the final result for the fermion force of the staggered action as

$$F_{F,\mu}(n)_{ef} = -\frac{\eta_\mu(n)}{2a}U_\mu(n)_{ec}\Big(\chi_c(n+\hat{\mu})\ (D^\dagger\chi)_f(n) - (D^\dagger\chi)_c(n+\hat{\mu})\ \chi^\dagger_f(n)\Big) \tag{A.6.7}$$

$$\Rightarrow F_{F,\mu}(n)\Big|_{TA} = -\frac{\eta_\mu(n)}{2a}U_\mu(n)\Big(\chi(n+\hat{\mu})\ (D^\dagger\chi)^\dagger(n) - (D^\dagger\chi)(n+\hat{\mu})\ \chi^\dagger(n)\Big)\Big|_{TA} \ . \tag{A.6.8}$$

A.7. The Leap Frog Integrator

A simple algorithm to numerically solve the equations of motions for conjugate variables will be shown here. As the exact evolution of a system according to the equations of motion from a Hamiltonian formulation preserves the phase space volume (Liouville's theorem) and is reversible, thus deterministic, we also require these two properties for our numerical integrator. Integrators fulfilling these properties are *symplectic integrators*, like the leap frog integrator [40], which shall be explained here. The equations of motion we want to solve are

$$\frac{d}{d\tau}U_\mu = U_\mu\,(i\pi_\mu) \ , \tag{A.7.1}$$

$$\frac{d}{d\tau}\,(i\pi_\mu) = F_\mu\,[U_\mu] \ . \tag{A.7.2}$$

The basic idea of the leap frog integrator is to use the midpoint rule alternating for both equations of motion. Thus, the leap frog integrator is an iterative algorithm

starting at a given phase space point $(U_{\mu,0}, \pi_{\mu,0})$ and ending after n steps at the point $(U_{\mu,n}, \pi_{\mu,n})$. The total evolution time is given through the step size $\Delta\tau$ as $T = n\Delta\tau$. Consider equation (A.7.2) first, using the midpoint rule we can calculate a step $\pi_{\mu,k} \to \pi_{\mu,k+1}$ as

$$(i\pi_\mu)_{k+1} = (i\pi_\mu)_k + \Delta\tau F_\mu \left[U_{\mu,k+\frac{1}{2}}\right] \ . \tag{A.7.3}$$

Hence, a integration step for the conjugate momenta only requires the knowledge of the link variables at the mid-point. Same follows for the integration of the link variables according to equation (A.7.1), a step $U_{\mu,k} \to U_{\mu,k+1}$ is calculated as

$$U_{\mu,k+1} = \exp\left(\Delta\tau\,(i\pi_\mu)_{k+\frac{1}{2}}\right)\ U_{\mu,k} \ . \tag{A.7.4}$$

Therefore, to alternately solve the equations of motions, we only need to do an initial half-step for the conjugate momenta so that the intermediate values for the link variables and conjugate momenta are shifted by $\Delta\tau/2$. This can be done by using the Euler method

$$(i\pi_\mu)_{\frac{1}{2}} = (i\pi_\mu)_0 + \frac{\Delta\tau}{2} F_\mu\left[U_{\mu,0}\right] \ , \tag{A.7.5}$$

which only needs the information of the starting point $(U_{\mu,0}, \pi_{\mu,0})$. To end both integrations at the same time, a final half-step for the conjugate momenta is done

$$(i\pi_\mu)_n = (i\pi_\mu)_{n-\frac{1}{2}} + \frac{\Delta\tau}{2} F_\mu\left[U_{\mu,n}\right] \ . \tag{A.7.6}$$

To sum up, the leap frog integrator evolves the conjugate variables from phase space point $(U_{\mu,0}, \pi_{\mu,0})$ to $(U_{\mu,n}, \pi_{\mu,n})$ according to the following three steps:

1. Initial step (A.7.5)
2. Intermediate steps

$$U_{\mu,k+1} = \exp\left(\Delta\tau\,(i\pi_\mu)_{k+\frac{1}{2}}\right)\ U_{\mu,k} \tag{A.7.7}$$

$$(i\pi_\mu)_{k+\frac{3}{2}} = (i\pi_\mu)_{k+\frac{1}{2}} + \Delta\tau F_\mu\left[U_{\mu,k+1}\right] \tag{A.7.8}$$

3. Final step (A.7.6)

Figure (A.2) shows the evolution of the conjugate variables, after the initial half-step they leap frog over each other ending with the final half-step. One might wonder why we do not use Euler's method from the beginning, saving the additional effort for the half-steps. The reasons for this are that Euler's method does not preserve the phase space volume and is not reversible [40]. From this it follows that the leap frog integrator is a second order method, whereas Euler's method is only of order one. Hence, for the leap frog integrator the overall error for the integration of a finite time T is $\sim \Delta\tau^2$.

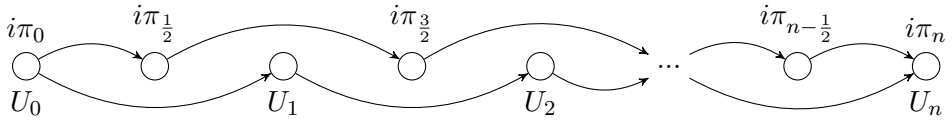

Figure A.2.: An illustration of the evolution of the conjugate variables.

A.8. The Fermion Determinant for SU(2)

We will show here that the fermion determinant is real when SU(2) is the gauge group, even if a non-vanishing chemical potential is included in the Dirac operator, which violates the property of γ_5-hermiticity. For this, we stress that the fundamental representation of SU(2) is pseudo-real, see equation (5.3.3). We introduce the matrix $S = C\gamma_5\tau_2$, where C is the charge conjugation matrix ($C\gamma_\mu C^{-1} = -\gamma_\mu^T$) and τ_2 is a Pauli matrix, and apply it on the continuum Dirac operator including a chemical potential to achieve [24]

$$\begin{aligned} S\ D(\mu)\ S^{-1} &= (C\gamma_5\tau_2)\ (\gamma_\mu(\partial_\mu + iA_\mu) + m + \gamma_4\mu)\ (C\gamma_5\tau_2)^{-1} \\ &= (C\gamma_5)\ (\gamma_\mu(\partial_\mu - iA_\mu^*) + m + \gamma_4\mu)\ (C\gamma_5)^{-1} \\ &= C\ (-\gamma_\mu(\partial_\mu - iA_\mu^*) + m - \gamma_4\mu)\ C^{-1} \\ &= ((\gamma_\mu^T)^*(\partial_\mu + iA_\mu) + m + (\gamma_4^T)^*\mu)^* \\ &= (\gamma_\mu(\partial_\mu + iA_\mu) + m + \gamma_4\mu)^*\ , \end{aligned} \tag{A.8.1}$$

where we have used equation (A.1.3). For the determinant follows that

$$\det(D(\mu)) = \det\left(S\ D(\mu)\ S^{-1}\right) = \det(D(\mu)^*) = \det(D(\mu))^*\ . \tag{A.8.2}$$

Hence, the fermion determinant in two-color QCD is real and the interpretation of it as an additional possibility weight for the gauge configurations is possible.

A.9. The conjugate transpose Staggered Dirac Operator

Here, the conjugate transpose of the staggered Dirac operator (5.2.8) with non-vanishing mass and chemical potential will be calculated. Using $U_\mu(m)^\dagger = U_{-\mu}(m + \hat{\mu})$ and $U_{-\mu}(m)^\dagger = U_\mu(m - \hat{\mu})$, we achieve

$$
\begin{aligned}
D^\dagger(n|m) &= \sum_{\mu=1}^{4} \frac{\eta_\mu(m)}{2a} \left[U_{-\mu}(m+\hat{\mu})\ e^{a\mu\delta_{\mu,4}}\ \delta_{n,m+\hat{\mu}} - U_\mu(m-\hat{\mu})\ e^{-a\mu\delta_{\mu,4}}\ \delta_{n,m-\hat{\mu}} \right] + m\ \delta_{mn} \\
&= -\sum_{\mu=1}^{4} \frac{\eta_\mu(n)}{2a} \left[U_\mu(n)\ e^{-a\mu\delta_{\mu,4}}\ \delta_{n,m-\hat{\mu}} - U_{-\mu}(n)\ e^{a\mu\delta_{\mu,4}}\ \delta_{n,m+\hat{\mu}} \right] + m\ \delta_{mn} \\
&= -\left(\sum_{\mu=1}^{4} \frac{\eta_\mu(n)}{2a} \left[U_\mu(n)\ e^{-a\mu\delta_{\mu,4}}\ \delta_{n+\hat{\mu},m} - U_{-\mu}(n)\ e^{a\mu\delta_{\mu,4}}\ \delta_{n-\hat{\mu},m} \right] - m\ \delta_{mn} \right) .
\end{aligned}
\tag{A.9.1}
$$

For the staggered phase we have used the property

$$
\eta_\mu(m \pm \nu) = \begin{cases} -\eta_\mu(m), & \nu < \mu \\ \eta_\mu(m), & \nu \geqslant \mu \end{cases} . \tag{A.9.2}
$$

Hence, the staggered Dirac operator obeys

$$
D[\mu, m]^\dagger = -D[-\mu, -m] . \tag{A.9.3}
$$

A.10. Proving the Spin-Taste Transformation

Here, we will show the calculation of the staggered action in taste basis, obtained by applying the spin-taste transformation (3.2.4) to the staggered action (3.1.3). First, using the orthogonally and completeness relations of the Γ matrices [5]

$$
\begin{aligned}
&\frac{1}{4}\mathrm{tr}\left(\Gamma_s^\dagger \Gamma_{s'}\right) = \delta_{ss'} , \\
&\frac{1}{4}\sum_s \Gamma^\dagger_{s,a\alpha}\Gamma_{s,\beta b} = \delta_{ab}\delta_{\alpha\beta} ,
\end{aligned}
\tag{A.10.1}
$$

we can invert the spin-taste transformation (3.2.4) and obtain

$$
\begin{aligned}
\chi(2y+s) &= 2\ \mathrm{tr}\left(\Gamma_s^\dagger\ q(y)\right) = 2\sum_{a\alpha} \Gamma^\dagger_{s,a\alpha}\ q(y)_{\alpha a} , \\
\bar{\chi}(2y+s) &= 2\ \mathrm{tr}\left(\bar{q}(y)\ \Gamma_s\right) = 2\sum_{a\alpha} \bar{q}(y)_{a\alpha}\Gamma_{s,\alpha a} .
\end{aligned}
\tag{A.10.2}
$$

The mass term is readily transformed and one arrives at

$$
\begin{aligned}
a^4 \sum_n \bar{\chi}(n)\chi(n) &= 4a^4 \sum_y \sum_s \bar{q}(y)_{a\alpha}\Gamma_{s,\alpha a}\ \Gamma^\dagger_{s,a'\alpha'} q(y)_{\alpha' a'} \\
&= 16a^4 \sum_y \bar{q}(y)_{a\alpha} q(y)_{\alpha a} \\
&= b^4 \sum_y \bar{q}(y)\left(\mathbb{I}\otimes\mathbb{I}\right) q(y)\ ,
\end{aligned}
\tag{A.10.3}
$$

where we have used the relations for the Γ matrices in equations (A.10.1) and identified the lattice spacing b of the hypercubes as $b = 2a$. We employ the notation of the direct product $\gamma \otimes t$ to separate matrices γ acting on the Dirac space and matrices t acting on the taste space [9]. Thus, the mass term is Dirac and taste diagonal. To transform the kinetic term, it is important to notice that the shifted fields $\chi(2y + s \pm \hat{\mu})$ mix components from different hypercubes. Depending on the value of s, we need to assign the correct hypercube for the spin taste transformation, one finds [5]

$$
\begin{aligned}
\chi(2y+s+\hat{\mu}) &= 2\left(\delta_{s_\mu 0}\Gamma^\dagger_{s+\hat{\mu},a\alpha} q(y)_{a\alpha} + \delta_{s_\mu 1}\Gamma^\dagger_{s-\hat{\mu},a\alpha} q(y+\hat{\mu})_{a\alpha}\right) \\
\chi(2y+s-\hat{\mu}) &= 2\left(\delta_{s_\mu 0}\Gamma^\dagger_{s+\hat{\mu},a\alpha} q(y-\hat{\mu})_{a\alpha} + \delta_{s_\mu 1}\Gamma^\dagger_{s-\hat{\mu},a\alpha} q(y)_{a\alpha}\right)\ .
\end{aligned}
\tag{A.10.4}
$$

Furthermore, reminding that $\gamma_\mu^2 = \mathbb{I}$, we find for the staggered phases (3.1.4)

$$
\eta_\mu(n) = \eta_\mu(2y+s) = \eta_\mu(s)\ . \tag{A.10.5}
$$

Using this for the kinetic term, we achieve after some resorting

$$
\begin{aligned}
& a^4 \sum_n \sum_\mu \frac{\eta_\mu(n)}{2a}\left(\bar{\chi}(n)\chi(n+\hat{\mu}) - \bar{\chi}(n)\chi(n-\hat{\mu})\right) \\
&= \frac{a^3}{2}\sum_y \sum_s \sum_\mu \eta_\mu(s)\bar{\chi}(2y+s)\left(\chi(2y+s+\hat{\mu}) - \chi(2y+s-\hat{\mu})\right) \\
&= \frac{a^3}{2}\sum_y \sum_s \sum_\mu \eta_\mu(s) 2q(y)_{b\beta}\Gamma_{s,\beta b}\Big[2\delta_{s_\mu 1}\Gamma^\dagger_{s-\hat{\mu},a\alpha} q(y+\hat{\mu})_{\alpha a} - 2\delta_{s_\mu 0}\Gamma^\dagger_{s+\hat{\mu},a\alpha} q(y-\hat{\mu})_{\alpha a} \\
&\quad -2\left(-\delta_{s_\mu 0}\Gamma^\dagger_{s+\hat{\mu},a\alpha} + \delta_{s_\mu 1}\Gamma^\dagger_{s-\hat{\mu},a\alpha}\right) q(y)_{\alpha a}\Big]\ .
\end{aligned}
\tag{A.10.6}
$$

For the next step, we need to use some properties of the Γ matrices which are shown in appendix {A.11}, this leads to

$$= \frac{a^3}{2} \sum_y \sum_s \sum_\mu 2q(y)_{b\beta} \Gamma_{s,\beta b} \Gamma^\dagger_{s,a'\alpha'} \left[\left((\gamma_\mu)_{\alpha'\alpha} \delta_{a'a} - (\gamma_5)_{\alpha'\alpha} (t_5 t_\mu)_{a'a} \right) q(y+\hat{\mu})_{\alpha a} \right.$$
$$\left. - \left((\gamma_\mu)_{\alpha'\alpha} \delta_{a'a} + (\gamma_5)_{\alpha'\alpha} (t_5 t_\mu)_{a'a} \right) q(y-\hat{\mu})_{\alpha a} + 2 \left((\gamma_5)_{\alpha'\alpha} (t_5 t_\mu)_{a'a} \right) q(y)_{\alpha a} \right] \ . \tag{A.10.7}$$

In this form, we can do the sum over the corners of the hypercubes s by using the completeness relation of the Γ matrices (A.10.1). After some more resorting, we arrive at

$$\begin{aligned} &= \frac{a^3}{2} \sum_y \sum_\mu 8 \ \bar{q}(y)_{a'\alpha'} \left[(\gamma_\mu)_{\alpha'\alpha} \delta_{a'a} \left(q(y+\hat{\mu})_{\alpha a} - q(y-\hat{\mu})_{\alpha a} \right) \right. \\ &\left. -(\gamma_5)_{\alpha'\alpha} (t_5 t_\mu)_{a'a} \left(q(y+\hat{\mu})_{\alpha a} - 2q(y)_{\alpha a} + q(y-\hat{\mu})_{\alpha a} \right) \right] \ . \end{aligned} \tag{A.10.8}$$

Lastly, we introduce the two derivative operators [5]

$$\begin{aligned} \nabla_\mu q(y) &= \frac{q(y+\hat{\mu}) - q(y-\hat{\mu})}{2b} \ , \\ \Delta_\mu q(y) &= \frac{q(y+\hat{\mu}) - 2q(y) + q(y-\hat{\mu})}{b^2} \end{aligned} \tag{A.10.9}$$

and arrive at our final result for the kinetic term, given by

$$= b^4 \sum_y \sum_\mu \bar{q}(y) \left[(\gamma_\mu \otimes \mathbb{I}) \nabla_\mu - \frac{b}{2} (\gamma_5 \otimes t_5 t_\mu) \ \Delta_\mu \right] q(y) \ . \tag{A.10.10}$$

Hence, putting the mass term and the kinetic term back together the free staggered action in taste basis can be written as

$$S_F[q,\bar{q}] = b^4 \sum_y \bar{q}(y) \left\{ m \left(\mathbb{I} \otimes \mathbb{I} \right) + \sum_\mu \left[(\gamma_\mu \otimes \mathbb{I}) \nabla_\mu - \frac{b}{2} (\gamma_5 \otimes t_5 t_\mu) \ \Delta_\mu \right] \right\} q(y) \ . \tag{A.10.11}$$

A.11. Useful Relations of the Γ matrices

From the definition of the Γ matrices

$$\Gamma_s = \gamma_0^{s_0} \gamma_1^{s_1} \gamma_{s_2}^{s_2} \gamma_3^{s_3} \ , \tag{A.11.1}$$

where $s_\mu = 0, 1$, the following relation can be obtained

$$(\gamma_\mu)_{\alpha'\alpha}\Gamma_{s,\alpha a} = \delta_{s_\mu 0}\ \eta_\mu(s)\ \Gamma_{s+\hat{\mu},\alpha' a} + \delta_{s_\mu 1}\ \eta_\mu(s)\ \Gamma_{s-\hat{\mu},\alpha' a}\ . \tag{A.11.2}$$

It is also easy to find that [17]

$$\Gamma_s\gamma_\mu = (-1)^{s_0+s_1+s_2+s_3}\ (-1)^\mu\ \gamma_\mu\Gamma_s \tag{A.11.3}$$

$$\Gamma_s\gamma_5 = (-1)^{s_0+s_1+s_2+s_3}\ \gamma_5\Gamma_s \tag{A.11.4}$$

$$\Rightarrow\quad (\gamma_5)_{\alpha'\alpha}\Gamma_{s,\alpha a}(\gamma_\mu\gamma_5)_{aa'} = -(-1)^{s_\mu}(\gamma_\mu)_{\alpha'\alpha}\Gamma_{s,\alpha a'}\ . \tag{A.11.5}$$

Defining the taste matrices $t_\mu = \gamma_\mu^T$, we can rewrite the right-hand side of equation (A.11.5) and use equation (A.11.2) for the left-hand side to achieve the equation

$$(\gamma_5)_{\alpha'\alpha}(t_5 t_\mu)_{a'a}\Gamma_{s,\alpha a} = -\delta_{s_\mu 0}\ \eta_\mu(s)\ \Gamma_{s+\hat{\mu},\alpha' a'} + \delta_{s_\mu 1}\ \eta_\mu(s)\ \Gamma_{s-\hat{\mu},\alpha' a'}\ . \tag{A.11.6}$$

Finally, we can combine equation (A.11.2) and equation (A.11.6) to arrive at two equations which are needed for the calculation of the staggered action in the taste basis

$$\left((\gamma_\mu)_{\alpha'\alpha}\delta_{a'a} - (\gamma_5)_{\alpha'\alpha}(t_5 t_\mu)_{a'a}\right)\Gamma_{s,\alpha a} = 2\delta_{s_\mu 0}\ \eta_\mu(s)\ \Gamma_{s+\hat{\mu},\alpha' a'}\ , \tag{A.11.7}$$

$$\left((\gamma_\mu)_{\alpha'\alpha}\delta_{a'a} + (\gamma_5)_{\alpha'\alpha}(t_5 t_\mu)_{a'a}\right)\Gamma_{s,\alpha a} = 2\delta_{s_\mu 1}\ \eta_\mu(s)\ \Gamma_{s-\hat{\mu},\alpha' a'}\ . \tag{A.11.8}$$

By taking the complex conjugate of the equations in this section, one finds similar equations for the $\Gamma^\dagger$ matrices with the only change that $(t_5 t_\mu)^\dagger = -(t_5 t_\mu)$ introduces a minus sign on the left-hand side of equation (A.11.6) and thus changes the relative signs of the two terms on the left-hand side of equations (A.11.7) and (A.11.8).

A.12. The zero-momentum projected Correlation Functions

Here, we will show the explicit calculations of the correlation functions from section {8.2} at non-vanishing chemical potential. For this, we employ Wick's theorem (8.2.6) and the γ_5-hermiticity of the staggered Dirac operator (8.2.7). For channel 1 we obtain

$$\begin{aligned}
C(t) &= \sum_{\vec{x}} \left\langle 0 \left| \bar{\chi}_i(\vec{x},t)\chi_i(\vec{x},t)\bar{\chi}_j(\vec{0},0)\chi_j(\vec{0},0) \right| 0 \right\rangle \\
&= \sum_{\vec{x}} \left(G_{ii}(\vec{x},t;\vec{x},t)G_{jj}(0,0) - G_{ji}(0;\vec{x},t)G_{ij}(\vec{x},t;0)\right) \\
C(t)_c &= -\sum_{\vec{x}} \eta_5(\vec{x},t)\ \mathrm{tr}\left[G^\dagger[-\mu](\vec{x},t;0)G[\mu](\vec{x},t;0)\right]\ ,
\end{aligned}$$

where the index c identifies the connected contribution. Channel 2 follows now easily by noticing that $\eta_5(\vec{x},t)\cdot\eta_4(\vec{x},t) = (-1)^t$, the result is

$$C(t)_c = -(-1)^t \sum_{\vec{x}} \mathrm{tr}\left[G^\dagger[-\mu](\vec{x},t;0)G[\mu](\vec{x},t;0)\right] \ .$$

The correlation function for channel 3 consists of connected contributions only and is given by

$$\begin{aligned}
C(t) &= \frac{1}{4}\sum_{\vec{x}} \Big\langle 0 \Big| \big(\chi^T(\vec{x},t)\tau_2\chi(\vec{x},t) - \bar{\chi}(\vec{x},t)\tau_2\bar{\chi}^T(\vec{x},t)\big) \\
&\qquad \Big(\chi^T(\vec{0},0)\tau_2\chi(\vec{0},0) - \bar{\chi}(\vec{0},0)\tau_2\bar{\chi}^T(\vec{0},0)\Big)\Big| 0\Big\rangle \\
&= \frac{1}{4}\sum_{\vec{x}} \Big\langle 0 \Big| \chi_i(\vec{x},t)\tau_2^{ij}\chi_j(\vec{x},t)\bar{\chi}_k(0)\tau_2^{kl}\bar{\chi}_l(0) + \bar{\chi}_k(\vec{x},t)\tau_2^{kl}\bar{\chi}_l(\vec{x},t)\chi_i(0)\tau_2^{ij}\chi_j(0)\Big| 0\Big\rangle \\
&= \frac{1}{4}\sum_{\vec{x}} \Big(G_{il}(\vec{x},t;0)\tau_2^{ij}G_{jk}(\vec{x},t;0)\tau_2^{kl} - G_{ik}(\vec{x},t;0)\tau_2^{ij}G_{jl}(\vec{x},t;0)\tau_2^{kl} \\
&\qquad -G_{ki}(0;\vec{x},t)\tau_2^{ij}G_{lj}(0;\vec{x},t)\tau_2^{kl} + G_{li}(0;\vec{x},t)\tau_2^{ij}G_{kj}(0;\vec{x},t)\tau_2^{kl}\Big) \\
&= \frac{1}{4}\sum_{\vec{x}} \Big((G^T)_{li}(\vec{x},t;0)\tau_2^{ij}G_{jk}(\vec{x},t;0)\tau_2^{kl} + (G^T)_{ki}(\vec{x},t;0)\tau_2^{ij}G_{jl}(\vec{x},t;0)\tau_2^{lk} \\
&\qquad +G_{ki}(0;\vec{x},t)\tau_2^{ij}(G^T)_{jl}(0;\vec{x},t)\tau_2^{lk} + G_{li}(0;\vec{x},t)\tau_2^{ij}(G^T)_{jk}(0;\vec{x},t)\tau_2^{kl}\Big) \\
&= \frac{1}{2}\sum_{\vec{x}} \left\{\mathrm{tr}\left[G^T(\vec{x},t;0)\tau_2 G(\vec{x},t;0)\tau_2\right] + \mathrm{tr}\left[G(0;\vec{x},t)\tau_2 G^T(0;\vec{x},t)\tau_2\right]\right\} \\
&= \frac{1}{2}\sum_{\vec{x}} \left\{\mathrm{tr}\left[G^T[\mu](\vec{x},t;0)\tau_2 G[\mu](\vec{x},t;0)\tau_2\right] + \mathrm{tr}\left[G^\dagger[-\mu](\vec{x},t;0)\tau_2 (G^\dagger)^T[-\mu](\vec{x},t;0)\tau_2\right]\right\} \ ,
\end{aligned}$$

where the two terms correspond to a diquark and anti-diquark contribution, respectively. Lastly, Channel 4 follows in the same manner

$$\begin{aligned}
C(t) = \frac{1}{2}\sum_{\vec{x}} \eta_5(\vec{x},t) \Big\{&\mathrm{tr}\left[G^T[\mu](\vec{x},t;0)\tau_2 G[\mu](\vec{x},t;0)\tau_2\right] + \\
&\mathrm{tr}\left[G^\dagger[-\mu](\vec{x},t;0)\tau_2 (G^\dagger)^T[-\mu](\vec{x},t;0)\tau_2\right]\Big\} \ .
\end{aligned}$$

A.13. The Dependence of the Correlation Functions on the Diquark Source

This section will derive the dependence of the correlation functions from section {8.2} on the diquark source. Once more, we rewrite the staggered action with an explicit diquark source term into a new basis

$$S_F = \phi^\dagger \tilde{A} \phi = \begin{pmatrix} \bar{\chi} & \chi^T \tau_2 \end{pmatrix} \begin{pmatrix} \lambda & D[\mu] \\ -D[\mu]^\dagger & \lambda \end{pmatrix} \begin{pmatrix} \tau_2 \bar{\chi}^T \\ \chi \end{pmatrix} , \tag{A.13.1}$$

giving the usual result for the fermionic part of the partition function

$$Z_f = \int \mathcal{D}\phi^\dagger \mathcal{D}\phi e^{-\phi^\dagger \tilde{A} \phi} = \det(\tilde{A}) . \tag{A.13.2}$$

Now, the propagator is given by

$$G = \tilde{A}^{-1} = \left(\tilde{A}^\dagger \tilde{A}\right)^{-1} \tilde{A}^\dagger = \begin{pmatrix} \left(DD^\dagger + \lambda^2\right)^{-1} \lambda & -\left(DD^\dagger + \lambda^2\right)^{-1} D \\ \left(D^\dagger D + \lambda^2\right)^{-1} D^\dagger & \left(D^\dagger D + \lambda^2\right)^{-1} \lambda \end{pmatrix} . \tag{A.13.3}$$

Let us have a closer look at the components of the new fields

$$\phi^\dagger = \begin{pmatrix} \bar{\chi}_1 & \bar{\chi}_2 & \chi_i (\tau_2)_{i1} & \chi_i (\tau_2)_{i2} \end{pmatrix} , \quad \phi = \begin{pmatrix} (\tau_2)_{1i} \bar{\chi}_i \\ (\tau_2)_{2i} \bar{\chi}_i \\ \chi_1 \\ \chi_2 \end{pmatrix} , \tag{A.13.4}$$

where we explicitly show the two color components. In section {8.2} we used Wick's theorem $\langle 0 | \chi_i(x) \bar{\chi}_j(y) | 0 \rangle = G^0_{ij}(x,y)$ to calculate the correlation functions. Here, we have to find the corresponding equations for the new fields $\phi^\dagger$ and ϕ, which have to be consistent with the underlying theory. Thus, there are no contributions like $\langle 0 | \chi_i(x) \chi_j(y) | 0 \rangle$ or $\langle 0 | \bar{\chi}_i(x) \bar{\chi}_j(y) | 0 \rangle$. Therefore, we have only contributions from an upper component of $\phi^\dagger / \phi$ times a lower component of $\phi^\dagger / \phi$ or vice versa. We introduce the new notation $\phi_{i\alpha}$, where i is the color index and $\alpha = 1, 2$ is for the upper or lower component, respectively. The adapted Wick's theorem now reads

$$\begin{aligned}
\left\langle 0 \left| \phi_{i\alpha}(x) \phi^\dagger_{j\beta}(y) \right| 0 \right\rangle &= G_{i2,j1}(x,y)\ \delta_{\alpha 2} \delta_{\beta 1} - (\tau_2 G \tau_2)_{j2,i1}(y,x)\ \delta_{\alpha 1} \delta_{\beta 2} , \\
\left\langle 0 \left| \phi^\dagger_{i\alpha}(x) \phi_{j\beta}(y) \right| 0 \right\rangle &= (\tau_2 G \tau_2)_{i2,j1}(x,y)\ \delta_{\alpha 2} \delta_{\beta 1} - G_{j2,i1}(y,x)\ \delta_{\alpha 1} \delta_{\beta 2} , \\
\left\langle 0 \left| \phi_{i\alpha}(x) \phi_{j\beta}(y) \right| 0 \right\rangle &= (\tau_2)_{jk} G_{i2,k1}(x,y)\ \delta_{\alpha 2} \delta_{\beta 1} - (\tau_2)_{ik} G_{j2,k1}(y,x)\ \delta_{\alpha 1} \delta_{\beta 2} , \\
\left\langle 0 \left| \phi^\dagger_{i\alpha}(x) \phi^\dagger_{j\beta}(y) \right| 0 \right\rangle &= (\tau_2)_{ki} G_{k2,j1}(x,y)\ \delta_{\alpha 2} \delta_{\beta 1} - (\tau_2)_{kj} G_{k2,i1}(y,x)\ \delta_{\alpha 1} \delta_{\beta 2} .
\end{aligned} \tag{A.13.5}$$

Next, we rewrite the interpolating operators from section {8.1} into the form

$$O_X(x) = \phi^\dagger(x)\Gamma_X(x)\phi(x) \ , \tag{A.13.6}$$

where the Γ_X matrices can easily be read off to be

$$\text{Channel 1:} \ \ \Gamma_{f_0}(x) = \begin{pmatrix} 0 & 1 \\ 0 & 0 \end{pmatrix} \tag{A.13.7}$$

$$\text{Channel 2:} \ \ \Gamma_{\pi}(x) = \eta_4(x) \begin{pmatrix} 0 & 1 \\ 0 & 0 \end{pmatrix} \tag{A.13.8}$$

$$\text{Channel 3:} \ \ \Gamma_{qq/\bar{q}\bar{q}}(x) = \begin{pmatrix} -1 & 0 \\ 0 & 1 \end{pmatrix} \tag{A.13.9}$$

$$\text{Channel 4:} \ \ \Gamma_{\epsilon qq/\epsilon\bar{q}\bar{q}}(x) = \eta_5(x) \begin{pmatrix} -1 & 0 \\ 0 & 1 \end{pmatrix} \ . \tag{A.13.10}$$

Let us finally calculate the zero-momentum projected correlation function, where we again omit disconnected contributions

$$\begin{aligned}
C(t) &= \sum\nolimits_{\vec{x}} \left\langle 0 \left| \phi^\dagger_{i\alpha}(x)\Gamma_X^{i\alpha,j\beta}(x)\phi_{j\beta}(x)\phi^\dagger_{k\gamma}(0)\Gamma_X^{k\gamma,l\delta}(0)\phi_{l\delta}(0) \right| 0 \right\rangle \\
&= \sum\nolimits_{\vec{x}} \ ((\tau_2 G \tau_2)_{i2,l1}(x,0)\ \delta_{\alpha 2}\delta_{\delta 1} - G_{l2,i1}(0,x)\ \delta_{\alpha 1}\delta_{\delta 2})\,\Gamma_X^{i\alpha,j\beta}(x) \\
&\qquad \cdot (G_{j2,k1}(x,0)\ \delta_{\beta 2}\delta_{\gamma 1} - (\tau_2 G \tau_2)_{k2,j1}(0,x)\ \delta_{\beta 1}\delta_{\gamma 2})\,\Gamma_X^{k\gamma,l\delta}(0) \\
&\qquad - ((\tau_2)_{mi} G_{m2,k1}(x,0)\ \delta_{\alpha 2}\delta_{\gamma 1} - (\tau_2)_{mk} G_{m2,i1}(0,x)\ \delta_{\alpha 1}\delta_{\gamma 2})\,\Gamma_X^{i\alpha,j\beta}(x) \\
&\qquad \cdot ((\tau_2)_{lm} G_{j2,m1}(x,0)\ \delta_{\beta 2}\delta_{\delta 1} - (\tau_2)_{jm} G_{l2,m1}(0,x)\ \delta_{\beta 1}\delta_{\delta 2})\,\Gamma_X^{k\gamma,l\delta}(0) \\
&= \sum\nolimits_{\vec{x}} \ (\tau_2 G \tau_2)_{i2,l1}(x,0)\ \Gamma_X^{i2,j2}(x)\ G_{j2,k1}(x,0)\ \Gamma_X^{k1,l1}(0) \\
&\qquad - \ G_{l2,i1}(0,x)\ \Gamma_X^{i1,j2}(x)\ G_{j2,k1}(x,0)\ \Gamma_X^{k1,l2}(0) \\
&\qquad - (\tau_2 G \tau_2)_{i2,l1}(x,0)\ \Gamma_X^{i2,j1}(x)\ (\tau_2 G \tau_2)_{k2,j1}(0,x)\ \Gamma_X^{k2,l1}(0) \\
&\qquad + \ G_{l2,i1}(0,x)\ \Gamma_X^{i1,j1}(x)\ (\tau_2 G \tau_2)_{k2,j1}(0,x)\ \Gamma_X^{k2,l2}(0) \\
&\qquad - \ G_{m2,k1}(x,0)(\tau_2)_{mi}\ \Gamma_X^{i2,j2}(x)\ G_{j2,m1}(x,0)(\tau_2)_{lm}\ \Gamma_X^{k1,l1}(0) \\
&\qquad + \ G_{m2,i1}(0,x)(\tau_2)_{mk}\ \Gamma_X^{i1,j2}(x)\ G_{j2,m1}(x,0)(\tau_2)_{lm}\ \Gamma_X^{k2,l1}(0) \\
&\qquad + \ G_{m2,k1}(x,0)(\tau_2)_{mi}\ \Gamma_X^{i2,j1}(x)\ G_{l2,m1}(0,x)(\tau_2)_{jm}\ \Gamma_X^{k1,l2}(0) \\
&\qquad - \ G_{m2,i1}(0,x)(\tau_2)_{mk}\ \Gamma_X^{i1,j1}(x)\ G_{l2,m1}(0,x)(\tau_2)_{jm}\ \Gamma_X^{k2,l2}(0) \ .
\end{aligned}$$

Hence, we can plug in the Γ matrices for our four channels. We start with channel 1 and obtain the correlation function of the scalar meson as

$$C(t) = -\sum_{\vec{x}} \mathrm{tr}\left[G_{21}(0,x)G_{21}(x,0)\right] \ , \tag{A.13.11}$$

where the trace runs over color indices only. The propagator is given by

$$G_{21} = \left(D^\dagger D + \lambda^2\right)^{-1} D^\dagger \ , \tag{A.13.12}$$

which in the $\lambda \to 0$ limit reproduces the used propagator in section {8.2}, $G = D^{-1}$. Thus, as $G = D^{-1}$ does, also G_{21} should fulfill the property

$$G_{21}[\mu](0,x) = \eta_5(x) G_{21}^\dagger[-\mu](x,0)\eta_5(0) \ . \tag{A.13.13}$$

Using this property, we obtain the final result for the correlation function of the scalar meson from channel 1

$$C(t) = -\sum_{\vec{x}} \eta_5(x) \mathrm{tr}\left[(G_{21})^\dagger[-\mu](x,0)G_{21}(x,0)\right] \ , \tag{A.13.14}$$

which is just the same result as in section {8.2} except for the replacement $G \to G_{21}$, which brings in the λ-dependence of the correlation function. Note that we calculate G through

$$G = D^{-1} = (D^\dagger D)^{-1} D^\dagger \tag{A.13.15}$$

and hence we only have to do the usual replacement $D^\dagger D \to D^\dagger D + \lambda^2$ in this step to incorporate the full λ-dependence. This is true for all four channels. For completeness we now explicitly show the remaining three channels, which, again, are the same as in section {8.2} expect for the replacement $G \to G_{21}$. The correlation function for the pion follows immediately by using $\eta_5(\vec{x},t) \cdot \eta_4(\vec{x},t) = (-1)^t$

$$C(t) = -(-1)^t \sum_{\vec{x}} \mathrm{tr}\left[(G_{21})^\dagger[-\mu](x,0)G_{21}(x,0)\right] \ . \tag{A.13.16}$$

For the (pseudo)scalar diquark of channel 3(4) we obtain

$$\begin{aligned} C(t) = \frac{1}{2}\sum_{\vec{x}} \mathrm{tr}\big[&(G_{21})^T[\mu](x,0)\ \tau_2\ G_{21}[\mu](x,0)\ \tau_2 \\ &+ (G_{21})^\dagger[-\mu](x,0)\ \tau_2\ (G_{21})^{\dagger,T}[-\mu](x,0)\ \tau_2\big] \ , \end{aligned} \tag{A.13.17}$$

$$\begin{aligned} C(t) = \frac{1}{2}\sum_{\vec{x}} \eta_5(x)\ \mathrm{tr}\big[&(G_{21})^T[\mu](x,0)\ \tau_2\ G_{21}[\mu](x,0)\ \tau_2 \\ &+ (G_{21})^\dagger[-\mu](x,0)\ \tau_2\ (G_{21})^{\dagger,T}[-\mu](x,0)\ \tau_2\big] \ . \end{aligned} \tag{A.13.18}$$

Acknowledgements

First of all, I want to thank Lorenz von Smekal for guiding me through this master thesis and taking the time to answer all my questions.

Furthermore I want to thank Dominik Smith for preparing and providing the CUDA code for LQCD Monte Carlo simulations and for supporting me during my coding.

The next thank you goes to Björn Wellegehausen for all of the good advises during this master thesis.

A big thanks goes to Lukas Holicki for enduring all of my questions at any time and for letting me use his OpenCl code for LQC_2D Monte Carlo simulations. I learned a lot from you about lattice gauge theories and about live. You made this last year one of the best, thank you.

More thanks go out to the rest of the Quantum Field Theory group. I enjoyed the nice working atmosphere.

Lastly, I want to thank my fellow students, Pascal Gunkel, Konstantin Otto and Jonas Schäfer for being good friends during the five years of studying physics in Gießen.

Selbstständigkeitserklärung

Hiermit versichere ich, die vorgelegte Thesis selbstständig und ohne unerlaubte fremde Hilfe und nur mit den Hilfen angefertigt zu haben, die ich in der Thesis angegeben habe. Alle Textstellen, die wörtlich oder sinngemäß aus veröffentlichten Schriften entnommen sind, und alle Angaben die auf mündlichen Auskünften beruhen, sind als solche kenntlich gemacht. Bei den von mir durchgeführten und in der Thesis erwähnten Untersuchungen habe ich die Grundsätze guter wissenschaftlicher Praxis, wie sie in der ‚Satzung der JustusLiebig-Universität zur Sicherung guter wissenschaftlicher Praxis' niedergelegt sind, eingehalten. Gemäß § 25 Abs. 6 der Allgemeinen Bestimmungen für modularisierte Studiengänge dulde ich eine Überprüfung der Thesis mittels Anti-Plagiatssoftware.

Ort, Datum *Jonas Wilhelm*

Bibliography

[1] J. B. Kogut, D. Toublan, and D. K. Sinclair. *Pseudo Goldstone spectrum of 2-color QCD at finite density.* Phys.Rev. D68 (2003) 054507, arXiv:hep-lat/0305003.

[2] Mark Srednicki. *Quantum Field Theory.* Cambridge University Press, 2007.

[3] Edmond Iancu. *QCD in heavy ion collisions.* CERN-2014-003, pp. 197-266, arXiv:1205.0579, 2012.

[4] Lochlainn O'Raifeartaigh. *Group Structure of Gauge Theories.* Cambridge University Press, 1988.

[5] C. Gattringer and C.B. Lang. *Quantum Chromodynamics on the Lattice - An Introductory Presentation.* Lect. Notes Phys. 788 (Springer, Berlin Heidelberg 2010), DOI 10.1007/978-3-642-01850-3.

[6] David Scheffler. *Two-Color Lattice QCD with Staggered Quarks.* PhD thesis, TU Darmstadt, 2015.

[7] J. B. Kogut, D. K. Sinclair, S. J. Hands, and S. E. Morrison. *Two-colour QCD at non-zero quark-number density.* Phys.Rev.D64:094505, arXiv:hep-lat/0105026, 2001.

[8] J. B. Kogut, D. Toublan, and D. K. Sinclair. *Diquark condensation at nonzero chemical potential and temperature.* Phys.Lett.B514:77-87, arXiv:hep-lat/0104010, 2001.

[9] Istvan Montway and Gernot Münster. *Quantum Fields on a Lattice.* Cambridge University Press, 1994.

[10] Rajan Gupta. *Introduction to lattice QCD.* arXiv:hep-lat/9807028, 1998.

[11] Thomas DeGrand and Carleton DeTar. *Lattice Methods for Quantum Chromodynamics.* World Scientific, 2006.

[12] B. Sheikholeslami and R. Wohlert. *Improved continuum limit lattice action for QCD with wilson fermions.* Nucl.Phys.B259:572-596, DOI 10.1016/0550-3213(85)90002-1, 1985.

[13] Michael E. Peskin and Daniel V. Schroeder. *An Introduction to Quantum Field Theory.* Addison-Wesley, 1995.

[14] G. Peter Lepage. *Lattice QCD for novices.* arXiv:hep-lat/0506036, 2005.

[15] M. Lüscher and P. Weisz. *On-shell improved lattice gauge theories.* Comm. Math. Phys. 97, no. 1-2, 59–77, 1985.

[16] Frithjof Karsch. *Lattice QCD at High Temperature and Density.* Lect.Notes Phys. 583 (2002) 209-249, arXiv:hep-lat/0106019, 2001.

[17] Sergio Caracciolo and Fabrizio Palumbo. *Transfer matrix for Kogut-Susskind fermions in the spin basis.* Phys. Rev. D 87 (2013) 014507, arXiv:1210.1786v1, 2012.

[18] D. B. Kaplan. *Chiral Symmetry and Lattice Fermions.* arXiv:0912.2560, 2009.

[19] Michael Creutz. *Anomalies and chiral symmetry in QCD.* Annals Phys.324:1573-1584, arXiv:0901.0150v2, 2009.

[20] Shao-jing Dong and Keh-fei Liu. *Stochastic Estimation with Z2 Noise.* Phys.Lett. B328 (1994) 130-136, arXiv:hep-lat/9308015v1, 1993.

[21] B.A. Berg. *Markov Chain Monte Carlo Simulations and Their Statistical Analysis.* World Scientific, Singapore, 2004.

[22] A. D. Kennedy. *Approximation theory for matrices.* Nucl.Phys.Proc.Suppl. 128C (2004) 107-116, arXiv:hep-lat/0402037.

[23] B. Jegerlehner. *Krylov space solvers for shifted linear systems.* arXiv:hep-lat/9612014v1, 1996.

[24] Owe Philipsen. *Lattice QCD at non-zero temperature and baryon density.* arXiv:1009.4089, 2010.

[25] Tamer Boz, Pietro Giudice, Simon Hands, Jon-Ivar Skullerud, and Anthony G. Williams. *Two-color QCD at high density.* arXiv:1502.01219, DOI 10.1063/1.4938682, 2015.

[26] Susan Morrison and Simon Hands. *Two Colours QCD at Nonzero Chemical Potential.* arXiv:hep-lat/9902012v1, 1999.

[27] Simon Hands. *Lattice Matter.* Nucl.Phys.Proc.Suppl. 106 (2002) 142-150, arXiv:hep-lat/0109034v1, 2001.

[28] Simon Hands, John B Kogut, Maria-paola Lombardo, and Susan E Morrison. *Symmetries and spectrum of SU(2) lattice gauge theory at finite chemical potential.* Nucl.Phys. B558 (1999) 327-346, arXiv:hep-lat/9902034.

[29] J B Kogut, M A Stephanov, D Toublan, J J M Verbaarschot, and A Zhitnitsky. *QCD-like Theories at Finite Baryon Density.* Nucl.Phys. B582 (2000) 477-513, arXiv:hep-ph/0001171v2.

[30] J. B. Kogut, M. P. Lombardo, and D. K. Sinclair. *Quenched QCD at finite density.* Phys.Rev. D51 (1995) 1282-1291, arXiv:hep-lat/9401039, 1994.

[31] Joshua Ellis. *TikZ-Feynman: Feynman Diagrams with TikZ.* arXiv:1601.05437, 2016.

[32] J. B. Kogut, M. a. Stephanov, and D. Toublan. *On two-color QCD with baryon chemical potential.* Phys.Lett. B464 (1999) 183-191, arXiv:hep-ph/9906346.

[33] K. Splittorff, D. Toublan, and J. J. M. Verbaarschot. *Diquark Condensate in QCD with Two Colors at Next-to-Leading Order.* Nucl.Phys. B620 (2002) 290-314, arXiv:hep-ph/0108040, 2001.

[34] Nils Strodthoff, Bernd-Jochen Schaefer, and Lorenz von Smekal. *Quark-meson-diquark model for two-color QCD.* Phys.Rev. D85 (2012) 074007, arXiv:1112.5401v2, 2011.

[35] Wolfgang Unger. *The Chiral Phase Transition of QCD with 2 + 1 Flavors.* PhD thesis, University of Bielefeld, 2010.

[36] V. V. Braguta, E. M. Ilgenfritz, A. Yu. Kotov, A. V. Molochkov, and A. A. Nikolaev. *Study of the phase diagram of dense two-color QCD within lattice simulation.* arXiv:1605.04090v3, 2016.

[37] Lukas Holicki. private communication.

[38] Philipp Scior and Lorenz von Smekal. *Effective Polyakov loop models for QCD-like theories at finite chemical potential.* Proceedings, 33rd International Symposium on Lattice Field Theory (Lattice 2015), arXiv:1602.04614, 2016.

[39] Michael A. Clark. *The Rational Hybrid Monte Carlo Algorithm.* PhD thesis, The University of Edingburgh, 2005.

[40] Peter Young. *The leapfrog method and other "sympletic" algorithms for integrating Newton's laws of motion.* Physics 155/242, 2014.